

國立臺灣大學理學院物理學研究所



碩士論文

Department of Physics

College of Science

National Taiwan University

Master Thesis

毫秒等級三維影像顯微鏡於果蠅腦之研究

Millisecond-scale Volumetric Imaging Microscopy for
Drosophila Brain Study

蔡宇軒

Yu-Hsuan Tsai

指導教授：朱士維 博士

Advisor: Shi-Wei Chu, Ph.D.

中華民國 109 年 7 月

July, 2020

口試委員會審定書

國立臺灣大學碩士學位論文

口試委員會審定書

毫秒等級三維影像顯微鏡於果蠅腦之研究

Millisecond-scale Volumetric Imaging Microscopy
for *Drosophila* Brain Study

本論文係 蔡宇軒君 (r06222013) 在國立臺灣大學物理學系、所完成之碩士學位論文，於民國 109 年 07 月 06 日承下列考試委員審查通過及口試及格，特此證明

口試委員：

朱士維

(簽名)

(指導教授)

江子世

陳柏文

朱若舟

謝辭

不知不覺在實驗室就待了三年多的時間，從一開始的實驗室新手懵懵懂懂的學習，一路慢慢累積經驗到現在已經快要是實驗室年資最久的人了，回顧這段時光真的受到不少人的幫忙。

首先，要感謝我的指導教授朱士維教授，不但在教學方面很有耐心的回答我們對於光學以及架設系統的各種問題，在研究這條路上也幫忙建立了相當嚴謹的態度，對我來說受益最多的是除了學會如何有邏輯的思考問題、找到關鍵原因並提出合理的解決方法之外，還有口頭報告的重要性，畢竟未來我們不一定會有機會碰到光學這塊領域，但能不能夠有邏輯的處理問題以及讓別人清楚了解我們的想法卻是我們帶得走的能力，這些都是我在遇見朱士維教授之前不曾重視的能力。

另外我也要特別感謝清大的江安世教授以及朱麗安教授提供生物樣本進行測試，特別是朱麗安教授，還特地抽空跑來和我們一起測試系統，也幫忙解答了不少果蠅腦的知識。

再來要感謝的是學長姊們的幫忙。國仁學長你一直都是我們實驗室的支柱，儘管看起來相當嚴肅，但每次有問題向你詢問的時候都會非常細心的解釋。致維學長，雖然跟你共事的時間不多，但還是相當感謝你在我對系統有問題的時候都會仔細的跟我講解。涵源學長，你應該是我覺得相處起來最沒有架子的學長，感謝你對於口頭報告上的指引與修正。厚獻學長，感謝你在我一開始踏進實驗室不知道該找誰幫忙的時候願意帶我做量光斑實驗。黃喬學姊，感謝你帶我學會切果蠅腦還有常常跟我一起討論問題，不管是多小的問題都會認真看待。裕峰學長，雖然有時候覺得你對人很嚴厲，但很感謝你在我進實驗室的第一年一起把光路上的像差問題解決。

接下來是一起奮鬥的夥伴們。冠傑，你大概是我覺得實驗室裡最可靠的人了吧，接到手的事幾乎都會做到最好，不管是實驗上或是器材上的事，還有畫圖的標準，感謝你特地抽時間幫忙畫精美光路圖，每天都相當期待跟你和建昇一起邊騎腳踏車回家邊抒發今天遇到的事，相信你在往博士這條路上邁進的過程能夠順利。邦漢，實驗室最老的學生，可是卻像個小孩一樣反而相處起來沒有距離感，感謝你在苦悶的研究生涯中陪我一起奮鬥，互相傾吐苦水，讓碩士這條路上不再

這麼煩悶。伯超，雖然你中途就去當醫生了，但很感謝當初一起和你辦實驗室出遊的過程，還有時不時舉辦的各種宴會活動。

學弟妹的部分，建昇，真的很感謝你跑來和我一起接手同一個題目，雖然你各種忘東忘西，商用顯微鏡也遇到各種麻煩，但和你一起做實驗時的拌嘴都讓做實驗的過程變得不那麼乏味，甚至有時候會期待能夠一起做實驗。俊誼，感謝你陪我一起參加了各個研討會，還有一起討論如何跟廠商有效溝通，記得要多喝水啊。鴻羽，雖然你很怪，可是就是因為你很怪所以常常發生一些無厘頭的事，增添實驗室歡樂的氣氛，很感謝每次請你幫忙的時候都很樂意放下手邊的工作跑來幫我，不管最後有沒有成功，希望你的題目也能夠順利。伯元，很感謝你在我和建昇說明我們題目的困境後卻仍然願意接下這個題目，雖然你常常做實驗做到一半就跟我說肚子餓和想睡覺，但相信你凡事都要找到原因的態度能夠幫助你達成你的目標。

接下來要感謝的是我的父母親，感謝你們支持我的任何決定，不管是選擇大學科系或是選擇念研究所的時候，都不給予過多干涉，在我念碩班做實驗不順利時也不過於苛責，每次回家都使我能夠重新補充能量，讓我可以順利完成學業。我也要感謝怡瑄這幾年的陪伴，謝謝你在我低潮的時候陪我度過，在我實驗順利時一起慶祝分享喜悅，體會成長的點點滴滴。

最後要感謝的是臺灣大學提供這麼好的環境可以讓我們無憂無慮的學習，在這七年的時光裡，說長不長說短卻也不短，一路上經歷不少事，也成長了不少，尤其是碩班階段，算是立下了一個人生的里程碑，期許自己未來能夠更加精進。

摘要

大腦是生物最重要的器官之一，因為不管是情感、思考、記憶和甚至是生命徵象等大多數行為主要都是由大腦所控制。近百年來，儘管科學家已經對單顆神經元進行了詳盡的研究，我們對腦功能的理解仍然有限。主要原因之一在於大腦的功能並不是由單顆神經元所主導的，而是由全腦神經元之間交錯連接而成且結構複雜的神經網路所控制的。在這個研究裡我們以果蠅作為研究對象，因為果蠅不但具有相當完整的神經結構性圖譜，果蠅腦的大小也足夠小來達成全腦觀察，那為了瞭解功能性神經網路是如何在果蠅的大腦中運作，所需的工具應具有亞細胞的空間解析度以區分單顆神經元、毫秒等級的成像速度以捕捉神經元之間高速的訊號傳遞（像是動作電位）以及接近毫米立方體積的成像尺寸以用於全腦研究。

近年來，雙光子顯微鏡逐漸成為研究活體大腦功能性神經網路的重要工具，因為它不僅能夠提供非侵入性的觀察還能夠達到微米尺度的空間解析度以及深組織穿透深度的光學切片能力來涵蓋三維結構的大腦。為了捕獲神經元之間的快速動態行為，現有的雙光子顯微鏡已經能夠達到毫秒尺度的二維成像速度。然而，神經網路結構本質上是三維分佈的，由於雙光子顯微鏡需要透過掃描來完成三維成像的特性使得目前雙光子顯微鏡的三維成像速度遠低於毫秒尺度。

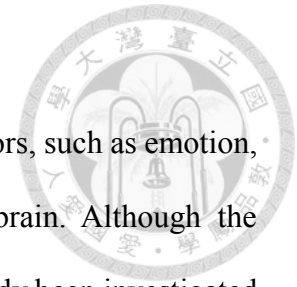
因此近十年來許多技術致力於提高三維成像速度，例如壓電致動器、液體透鏡、聲光偏轉器、全像術、空間時域聚焦和層光顯微鏡等等。然而前三種方法是基於單點掃描成像式的技術，由於橫向或軸向掃描速度的限制使得三維成像速度無法達到毫秒尺度。此外，這些技術大多使用單通道偵測器來收光，取樣速度會被螢光衰減週期所限制，導致取樣率不會超過 500 MHz，限制了影像速度。後三項技術則是基於廣域照明以及收光來提高成像速度，然而該方式很容易受到散射的影響導致穿透深度不深，因此比較適合用在透明樣本上而不適用於密集的神經網路結構(果蠅大腦)。

為了解決上述的問題，在這項研究中我們開發了一套多焦點多光子體積成像顯微技術，利用將單道光分成 32 道光，搭配上可調式聲波梯度折射率透鏡以及 32 通道的光電倍增管，我們達成了每秒 500 個體積以上的三維成像速度，體積大小約略是邊長為 200 微米的立方體。透過繞射分光元件產生的 32 道光做平行掃

描，相比於單道光來說可大幅度提高橫向掃描速度，而可調式聲波梯度折射率透鏡可提供約 100 kHz 的超快軸向掃描速度，從而達到毫秒等級的三維成像。為了能夠補捉可調式聲波梯度折射率透鏡的掃描速度，我們採用了 32 通道光電倍增管，不但有足夠快的資料取樣速度，整體的資料取樣率更可以提高到 10 GHz 以上（在這個研究中使用了 2.56 GHz），比起單通道偵測器來說整整多了一個數量級。為了證明系統的可行性，我們利用流動的螢光球來測試高速成像，的確能夠捕捉螢光球在流動時的動態行為。希望我們所發展的這套高速多焦點多光子體積成像技術能夠對果蠅全腦功能性神經網路研究有所幫助。

關鍵字：多焦點顯微鏡、多光子顯微鏡，可調式聲波梯度折射率透鏡、體積成像、毫秒等級時間解析度

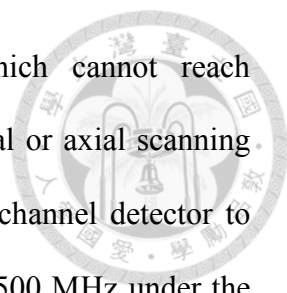
Abstract



Brain is one of the most important organs because most behaviors, such as emotion, thinking, memory and vital sign, are mainly governed by our brain. Although the behaviors of basic component of brain, so-called neurons, have already been investigated thoroughly for more than one century, our understanding toward brain function is still limited. One of the main reasons is that brain function is not performed by a single neuron, but dominated by sophisticated connections among neurons inside a whole brain, i.e. connectome. In this study, *Drosophila* was selected as our target not only due to its nearly-complete structural neural connectome but also small enough brain size, which is available for whole brain observation. In order to study how functional connectome works in living brain of *Drosophila*, the required tool should exhibit (i) sub-cellular spatial resolution to distinguish individual neurons, (ii) temporal imaging speed as high as kHz to capture rapid dynamics among neurons, such as action potential, and (iii) imaging size approaching hundreds of micrometers cubic in volume for whole brain study.

Recently, two-photon microscopy has emerged as a powerful tool for *in vivo* functional connectome study in living brains not only because of its noninvasive property but also due to its $\sim\mu\text{m}$ spatial resolution and optical sectioning capability to monitor 3D brain functions with remarkable penetration depth. In order to capture rapid dynamics among neurons, imaging speed of two-photon microscopy in lateral dimension can already reach up to kHz frame rate. Nevertheless, neural network is intrinsically three-dimensionally distributed, and current volumetric two-photon imaging speed is far below kHz due to the requirement of time-consuming sequential axial-scanning.

In the past decade, several schemes have been demonstrated to boost volumetric imaging speed, such as piezoelectric actuator, liquid lens, acousto-optic deflector, holography, spatial temporal focusing and light-sheet microscopy. However, the first



three methods are single-beam scanning-based techniques, which cannot reach millisecond-scale volumetric imaging due to the limitation of lateral or axial scanning speed. Besides, abovementioned techniques typically use a single-channel detector to collect signal, so that the data acquisition rate is restricted below ~500 MHz under the limitation of fluorescence lifetime. The latter three are based on wide-field illumination and wide-field detection to increase the imaging speed; however, they easily suffer image blurred due to scattering and are limited to transparent samples. Therefore, they are not suitable for dense neuron structures, such as *Drosophila* brains.

In this study, we developed a multi-focal multi-photon volumetric imaging microscopy, based on the combination of 32-channel multi-focal excitation, a tunable acoustic gradient-index (TAG) lens, and a 32-channel PMT, thus reaching unprecedented volumetric imaging rate above 500 volumes per second, in a cubic volume of ~200 μm on each side. The 32-focus parallel scanning is provided by a diffractive optical element (DOE) to considerably enhance lateral scanning speed. The TAG lens offers ~100 kHz ultrafast axial scanning speed, leading to millisecond-scale volumetric imaging. To catch up with the speed of the TAG lens, the 32-channel PMT was adopted which can further boost up data acquisition rate to more than 10 GHz (2.56 GHz is used in this work), one order larger than that of a single-channel detector system. As a proof of concept, we have demonstrated high speed imaging with flowing fluorescence beads, capturing volumetric dynamics of flow motion. Our high-speed multi-focal multi-photon volumetric imaging technique paves the way toward functional connectome study in *Drosophila* brain.

Keywords: Multi-focal microscopy, Multi-photon microscopy, Tunable acoustic gradient-index lens, Volumetric imaging, Millisecond-scale temporal resolution

Contents



口試委員會審定書	I
謝辭	II
摘要	IV
Abstract.....	VI
Contents.....	VIII
Figure list.....	X
Table list	XII
Chapter 1. Introduction of brain study: Technical problems and possible solutions .	1
1.1 Brain study: Features and challenges	1
1.1.1 Brain characteristics	1
1.1.2 Animal models: From human to <i>Drosophila</i>	4
1.1.3 Challenges for <i>Drosophila</i> brain study.....	5
1.2 Techniques comparison for brain study challenges.....	6
1.2.1 Common techniques for brain study: Why optical microscopy?	6
1.2.2 Optical microscopy for brain study: Why two-photon?	10
1.2.3 Current limitation of two-photon microscopy: Speed	10
1.2.4 How to improve lateral scanning speed: Multifocal.....	11
1.2.5 How to improve axial scanning speed: TAG lens	12
1.3 Aim: Millisecond-scale volumetric imaging microscopy for <i>Drosophila</i> brain study	13
Chapter 2. Principle of techniques for millisecond-scale volumetric microscopy...	15
2.1 Two-photon laser scanning microscopy	15
2.2 Multifocal multiphoton microscopy	18
2.2.1 Common multifocal techniques.....	18
2.2.2 Diffractive optical element (DOE)	20
2.3 TAG lens.....	22
2.4 Two-photon volumetric imaging microscopy.....	25
Chapter 3. System design of millisecond-scale volumetric imaging microscopy....	27
3.1 Optical setup	27
3.2 Contrast agent and excitation wavelength.....	30
3.3 Selection of each component.....	32

3.3.1	DOE	32
3.3.2	TAG lens	33
3.3.3	Photomultiplier tube (PMT)	35
3.3.4	Amplifier (AMP)	40
3.3.5	Data acquisition system (DAQ).....	41
3.4	Expected performance	47
3.4.1	Spatial resolution	47
3.4.2	Volumetric imaging: Size	48
3.4.3	Volumetric imaging: Speed	52
Chapter 4.	Experimental protocols and sample preparations	54
4.1	Experimental protocols.....	54
4.2	Sample preparations	61
4.2.1	Test sample: Fluorescent microspheres	61
4.2.2	In vitro fixed <i>Drosophila</i> brain slide	62
Chapter 5.	Results	63
5.1	System performance	63
5.1.1	Spatial resolution	63
5.1.2	Volumetric imaging: Size	65
5.1.3	Volumetric imaging: Speed	73
5.2	<i>Drosophila</i> brain imaging.....	75
Chapter 6.	Discussion.....	76
6.1	Strong absorption of TAG lens	76
6.2	Emitted photon number	78
6.3	Equal-interval sampling against stochastic fluorescent pulses.....	79
6.4	Cross-talk.....	80
6.5	Shot noise	81
Chapter 7.	Conclusion and future work	83
7.1	Conclusion	83
7.2	Future work	84
References	86

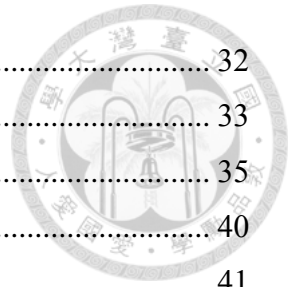


Figure list



Fig. 1.1.1 Neural structure and network	2
Fig. 1.1.2 Spike of action potential.....	3
Fig. 1.1.3 Comparison of brain size among human, mouse and fruit fly	4
Fig. 1.2.1 Functional magnetic resonance imaging	7
Fig. 1.2.2 Schematic of electrophysiology	8
Fig. 1.2.3 Schematic of optical microscopy	9
Fig. 2.1.1 Schematic of two-photon effect	15
Fig. 2.1.2 Schematic of raster scanning to acquire a volumetric image	17
Fig. 2.2.1 Schematic of function of DOE	21
Fig. 2.2.2 Schematic of raster scanning combining with the multi-focal method.....	21
Fig. 2.3.1 Schematic showing the operation of the TAG lens and how the combination of the TAG lens and the objective lens achieves axial scanning	23
Fig. 2.3.2 Axial extension of the TAG lens with different incident beam sizes	25
Fig. 2.4.1 Schematic of raster scanning combining with a multi-focal method and the TAG lens to achieve volumetric imaging	26
Fig. 3.1.1 Schematic of our system	27
Fig. 3.2.1 Two-photon absorption cross-section (σ_2) of eGFP versus laser wavelength	31
Fig. 3.2.2 Transmission rate of the TAG lens with different incident wavelengths	32
Fig. 3.3.1 TAG lens family	35
Fig. 3.3.2 Quantum efficiency of different types of material for multi-anode PMT	40
Fig. 3.3.3 Overall setup and data process procedure of our DAQ system.....	43
Fig. 3.3.4 Laser synchronization signal (CH1) and fluorescent pulse signal (CH2) captured by the oscilloscope.....	44
Fig. 3.3.5 Image reconstruction procedure	46

Fig. 3.4.1 Schematic of a volume with given dimensions for each scanning tool	49
Fig. 3.4.2 Specification of TAG lens 2.5β , including operation frequency, effective aperture, optical power and corresponding driving amplitude	50
Fig. 4.1.1 Control panel of 2D imaging software	55
Fig. 4.1.2 Appearance of laser delay board	56
Fig. 4.1.3 Control panel of the TAG lens and operation steps.....	57
Fig. 4.1.4 Control panel of data acquisition software and operation steps.....	59
Fig. 4.1.5 Control panel of image reconstruction software and operation steps	60
Fig. 5.1.1 Spatial and axial resolution verification.....	64
Fig. 5.1.2 3D reconstruction imaging of scanning pattern in sequence using a thin green-fluorescent film.....	65
Fig. 5.1.3 Image of 32 foci	66
Fig. 5.1.4 Experimental axial extension of the TAG lens.....	67
Fig. 5.1.5 Lateral scanning range of the galvanometric mirror	69
Fig. 5.1.6 Comparison of 2D fluorescent microspheres images.....	70
Fig. 5.1.7 Comparison of 3D observation	72
Fig. 5.1.8 Time-lapse volumetric imaging.....	74
Fig. 5.2.1 <i>Drosophila</i> brain imaging labeled with GCaMP7f on mushroom body	75
Fig. 6.1.1 Image of 32 foci captured by the sCMOS camera using FITC solution.....	77
Fig. 6.1.2 Image of partial 32 foci with and without aberration.....	78
Fig. 6.3.1 Comparison of ADRF6520 amplifier with different frequency responses using single-channel PMT detection	80
Fig. 6.5.1 Shot noise analysis	82

Table list

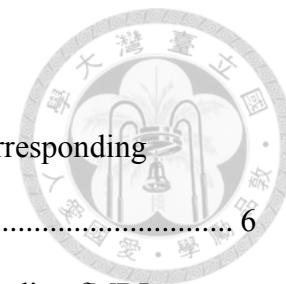


Table. 1.1.1 Organization of <i>Drosophila</i> brain characteristics and corresponding requirements.	6
Table. 1.2.1 Comparison of common techniques for brain study, including fMRI, electrophysiology and optical microscopy.	9
Table. 1.2.2 Organization of various axial scanning tools in terms of their scanning speed and characteristics.	13
Table. 2.2.1 Organization of possible choices for multi-focal method.....	20
Table. 3.1.1 List of each instrument with the information of company and model number.	30
Table. 3.3.1 Transmission rate of each optical component.....	39
Table. 3.3.2 Several parameters related to the data acquisition and throughput.	45
Table. 3.3.3 List of every instrument used in DAQ system with the information of company and model number.....	47
Table. 3.4.1 Several parameters related to the calculation of pixel number in axial direction.	51
Table. 3.4.2 Organization of maximal scanning range and total pixel number.	52
Table. 3.4.3 Estimation of volume rate with different number of pixels in y direction.	53
Table. 5.1.1 Comparison of lateral and axial resolution between theoretical and experimental results.....	65
Table. 5.1.2 Comparison between theoretical and experimental scanning range.....	71
Table. 5.1.3 Comparison between theoretical and experimental volume rate.....	73
Table. 7.1.1 Comparison between the requirements of our aim mentioned in section 1.3 and the experimental achievements.	84

Chapter 1. Introduction of brain study: Technical problems and possible solutions



Brain is one of the most important organs inside human body because several behaviors, such as emotion, thinking, vital sign and memory, are mainly controlled by our brain. However, even massive amount of effort is devoted, and longstanding studies for brain research has been proceeded for more than one century, our understanding toward brain function is still limited. The main obstacle is the lack of suitable tools to decipher the brain function for further investigation. Thus, in this chapter, we will describe the characteristics and fundamental properties of brain first and the primary challenge hindering the study of brain function. Next, in section 1.2, through comprehensive techniques review, appropriate techniques will be determined and the reasons of the selections will be clearly explained as well. In section 1.3, with the aid of the properly selected techniques, an innovative design is proposed, providing the opportunity to reveal the mystery of brain mechanism.

1.1 Brain study: Features and challenges

1.1.1 Brain characteristics

Since the day of Golgi and Cajal in 19th century, we gradually get deeper knowledge about our brains not only from the perspective of brain anatomical structure but also from the viewpoint of dynamic behaviors. To understand how brain truly works, it is important to know the basic component of brain structure is important. Brains are actually composed of neurons which are the fundamental units of brain [1]. Through longstanding research and investigation by neurologists and biologists for more than a century, the

characteristics of single neuron were well-understanding. As shown in Fig. 1.1.1(a), a single neuron is constructed by a cell body, an axon and plenty of dendrites. In general, a cell body ranges from $\sim 1 \mu\text{m}$ to $\sim 20 \mu\text{m}$ [2] depending on different species. A cell body is so-called soma which mainly dominates behavioral activities of a neuron, including signal transmission and collection. The function of dendrites is to collect signals from surrounding neurons. On the contrary, an axon is to transmit signals with a relatively longer route to synaptic or axon terminals. Then, signals will be delivered to the dendrites of adjacent neurons. These signals are known as action potential which cause by rapidly rising and falling of membrane potential spontaneously or passively being excited by adjacent neurons. Since the duration of action potential typically happens within few milliseconds [2], the response of the action potential looks like a spike, as shown in Fig. 1.1.2.

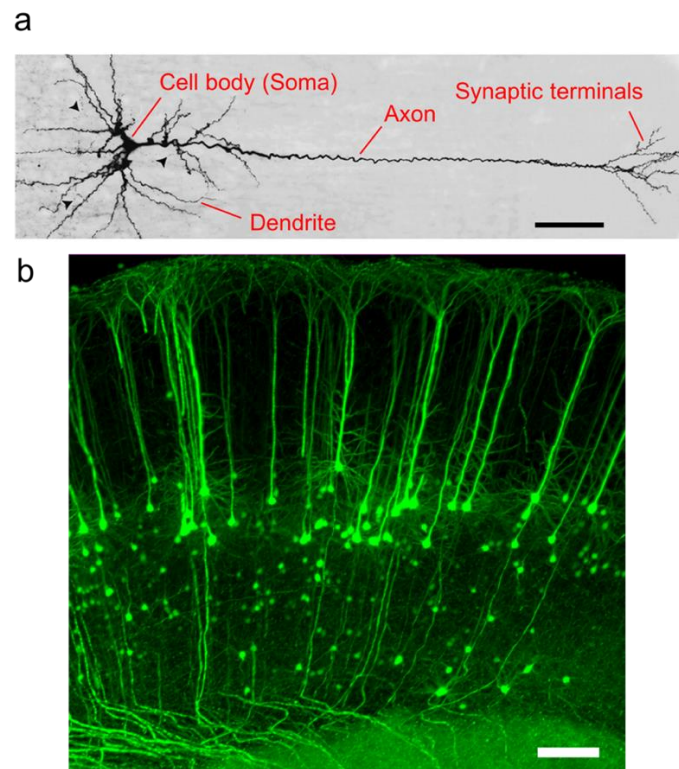


Fig. 1.1.1 Neural structure and network

(a) Extended-focus views rat pyramidal cells stained for biocytin [3]. The scale bar is 50

μm . (b) Neuronal network imaging of a Thy1-YFP transgenic mouse [4]. The scale bar is $200 \mu\text{m}$.



In the past century, although the behaviors of single neuron have already been investigated completely, our understanding toward brain function is still limited. One of the main reasons is that brain function is not performed by a single neuron, but dominated by sophisticated connections among neurons, also known as “connectome”, as shown in Fig. 1.1.1(b). From the above information, we know that neurons are based on the propagation of the millisecond-scale action potential to somehow “communicate” with each other within the neural network. In order to reveal the secret behind the mechanism of brain function, it is necessary to capture the path or propagation of action potential of each single neuron within a whole brain to recognize the pattern of these dynamic activities for in-depth investigation. The pattern of the neural network is known as “functional connectome” [5].

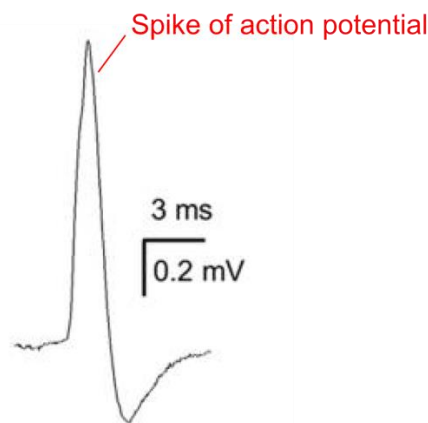


Fig. 1.1.2 Spike of action potential

Spontaneous intracellular firing activity recordings of rat hippocampal neurons [6].

1.1.2 Animal models: From human to *Drosophila*

Although capturing the functional connectome to understand human brain function is our final purpose, there are almost one 100 billion neurons inside the human brain with $\sim 1600 \text{ cm}^3$ cubic size [7] which is not trivial for whole brain study. Even the mouse brain has about 100 million neurons with centimeter cubic brain size [8]. It certainly takes plenty of time to recognize every single neuron, not to say that capturing the millisecond-scale dynamics among these neurons. It seems that an animal model with small brain size but functionally complicated is required. So, in this study, we choose *Drosophila Melanogaster*, so-called fruit fly, to be our target. There are about 130 thousand neurons [9] and $\sim 200 \times 700 \times 400 \text{ }\mu\text{m}^3$ cubic brain size. It not only possesses nearly-complete structural neural mapping, done by Brain Research Center in NTHU [10], but also is small enough for whole brain study. Besides, it shares 75% of human disease-causing genes [11], such as Parkinson's disease and epilepsy which is a suitable animal model for preliminary study.

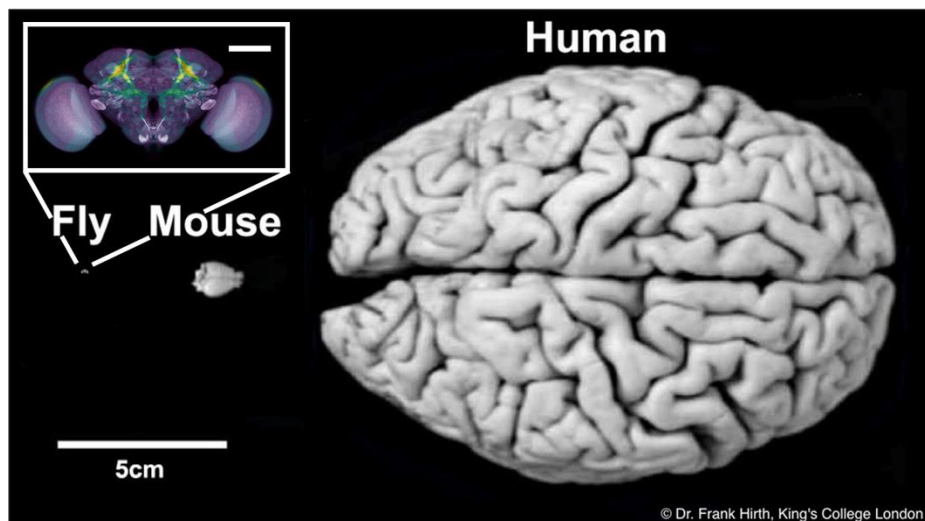


Fig. 1.1.3 Comparison of brain size among human, mouse and fruit fly

The scale bar of inset image is $100 \text{ }\mu\text{m}$. Image courtesy:

<https://theconversation.com/ode-to-the-fruit-fly-tiny-lab-subject-crucial-to-basic-research-38465>

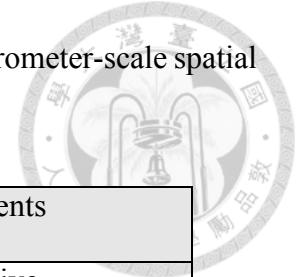


1.1.3 Challenges for *Drosophila* brain study

To achieve whole brain functional study of *Drosophila*, we need to understand some characteristics of *Drosophila* brain to select what kind of techniques are required in advance. First, since we aim at observing the functional connectome, it should be a living brain. Therefore, noninvasive method is essential for *in vivo* study. Second, the neuron size of *Drosophila* brain is around 5-6 μm [12], so we need a micrometer-scale spatial resolution to distinguish a single neuron. Third, in order to achieve deep tissue down to $\sim 200 \mu\text{m}$, hundreds of micrometers penetration depth is required. Fourth, a *Drosophila* brain is a 3D structure, so we need volumetric imaging modality for whole brain observation. Final, response time of a neuron or the action potential occurs within $\sim 2 \text{ ms}$ [13], so a ms-scale temporal resolution is highly demanded to capture rapidly transient neural dynamics. The characteristics and corresponding requirements are organized in Table. 1.1.1.

Although it seems that each requirement can be fulfilled individually, the challenge is that to achieve those requirements simultaneously, it becomes a tough issue. The bottleneck is mainly related to volumetric imaging and $\sim\text{ms}$ -scale temporal resolution. There are two primary limitations. First, in order to acquire a volumetric image, we certainly need imaging tools to somehow scan the sample. However, most techniques are restricted by the speed of imaging tools which cannot reach $\sim\text{ms}$ -scale temporal resolution. Second, a volumetric image can be considered as constructing by plenty of voxels. If the throughput of data which means voxel or pixel per second is not high enough, for example, maximum readout rate of commercial sCMOS cameras is about 500 MHz [14], the imaging speed will be ultimately restricted by this upper limit. Thus, no recent techniques

can cover all requirements for ms-scale volumetric imaging with micrometer-scale spatial resolution and deep tissue yet.



Characteristics	Requirements
In vivo/living brain	Noninvasive
Neuron size (~5-6 μm)	$\sim\mu\text{m}$ spatial resolution
Deep tissue	Hundreds of micrometers depth
3D brain structure	Volumetric imaging
Fast response (~2 ms action potential)	$\sim\text{ms}$ temporal resolution

Table. 1.1.1 Organization of *Drosophila* brain characteristics and corresponding requirements.

1.2 Techniques comparison for brain study challenges

In the following section, various techniques for brain study will be brought forward for discussion in detail, and suitable tools are specifically selected to fit our requirements for whole-brain high-speed observation in *Drosophila*.

1.2.1 Common techniques for brain study: Why optical microscopy?

During the past few decades, brain study and neuroscience have gradually become one of the popular research fields. More and more techniques are developed to reveal the mechanism of brain function. Hence, in order to select appropriate techniques, we briefly compare some most-commonly-used techniques for brain study, such as functional magnetic resonance imaging (fMRI), electrophysiology and optical microscopy, and choose a suitable one among them.

Functional magnetic resonance imaging (fMRI):

Functional MRI is based on measuring the magnetic resonance signal of blood. For example, while neurons inside the brain become active, massive amount of glucose and oxygen are consumed, causing the concentration of oxygenated-hemoglobin within the blood to increase in active brain region. Since the magnetic response of oxygenated-hemoglobin and deoxygenated-hemoglobin is different, as we guide external magnetic field through the brain, we can distinguish the active and inactive region of brain simply by the magnetic response, and the response is known as blood-oxygen-level dependent (BOLD) contrast. By observing the active region in human brain, as shown in orange area in Fig. 1.2.1, whole-brain activities can be monitored. However, although it is noninvasive and the region is large enough for whole brain observation, it cannot reach ~ms temporal resolution, at most ~20 ms [15]. Besides, the spatial resolution is quite poor, in general few millimeters, losing the capability to distinguish a single neuron [16, 17].

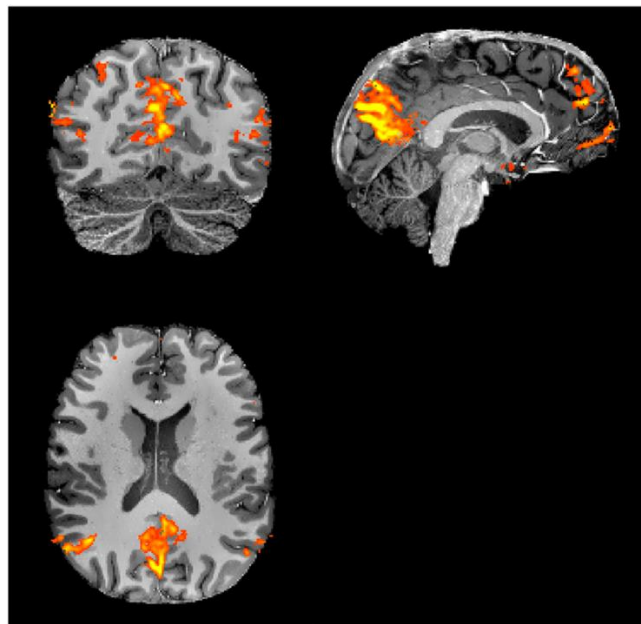


Fig. 1.2.1 Functional magnetic resonance imaging
The active region of human brain was shown with orange color [17].

Electrophysiology:

We already know that neurons transmit signal within the neural network via membrane potential variation. To capture the voltage variation, electrophysiology uses a thin probe to attach on the membrane of a neuron directly to record the response of action potential. Due to the direct measurement of electric signals, the temporal resolution can reach as high as the duration of action potential and the spatial resolution is determined by the dimension of the probe whose tip diameter can be manufactured below $\sim 1 \mu\text{m}$ [18]. Although such high spatial-temporal resolution can be provided by electrophysiology, it is relatively invasive for probe insertion, and the region of interest is restricted to a single neuron for each probe which means thousands of neurons require same number of probes for observation. Besides, it lacks the capability to repeat the experiment once the probe was detached from the neuron which is difficult to detect the same neuron again [19, 20].

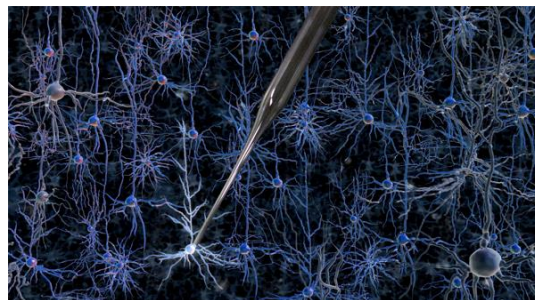


Fig. 1.2.2 Schematic of electrophysiology

A thin probe is used to attach on a single neuron for recording. Image courtesy: <https://www.medgadget.com/2012/05/robot-for-whole-cell-patch-clamp-electrophysiology-of-neurons-in-vivo.html>

Optical microscopy:

Optical microscopy manipulates light to illuminate or excite neurons of interest and captures the reflection or emitted signals by detectors for image formation. Due to inherent properties of optical microscopy, it is noninvasive, and the spatial resolution can reach \sim sub-micrometers [21]. The conventional way of optical microscopy uses wide-

field illumination which can observe multiple neurons simultaneously. With the aid of the development of fluorescent proteins, we possess the capability of labeling specific neurons of interest with genetically-encoded fluorescent proteins. With proper optical design, the 2D imaging speed can even reach beyond \sim ms temporal resolution [22], but the region of interest might not be as large as fMRI, \sim millimeter cubic size at large; nevertheless, it is sufficient to cover whole *Drosophila* brain.

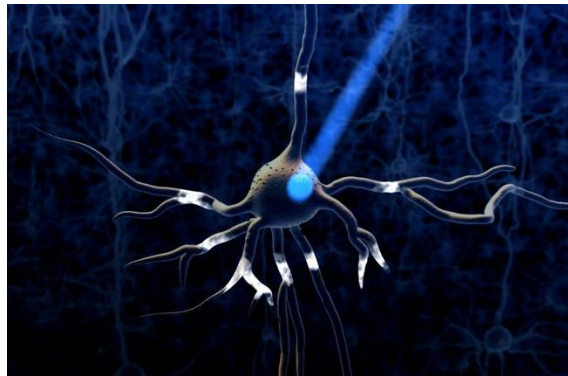


Fig. 1.2.3 Schematic of optical microscopy

By exciting the neuron with incident light, we can capture the image of a specific neuron. Image courtesy: <https://scientiportal.wordpress.com/2015/09/23/wireless-mice-batteries-not-included-optrodes-and-electrodes-in-one-wireless-contraption/>

In Table.1.2.1, these techniques are organized according to our requirements. It seems that optical microscopy well matches the requirements, so optical microscopy is chosen as the imaging tool in this study.

	fMRI	Electrophysiology	Optical microscopy
Temporal resolution (ms)	\sim 10	\sim 0.1	\sim 0.1
Spatial resolution (μ m)	\sim 1000	\sim 1	\sim 0.1
Noninvasive	O	X	O
Region of interest	Whole brain (\sim m ³)	Single neuron	Multiple neuron (\sim mm ³)

Table. 1.2.1 Comparison of common techniques for brain study, including fMRI, electrophysiology and optical microscopy.



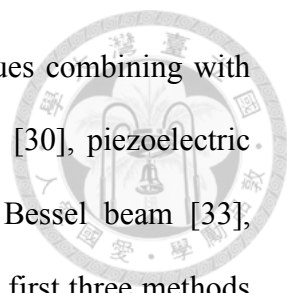
1.2.2 Optical microscopy for brain study: Why two-photon?

As mentioned above, conventional wide-field optical microscopy allows probing multiple neurons within the field of view simultaneously, but, due to the lack of optical section, it works well only for thin samples, and thus it is not applicable for 3D structures [22]. To tackle with this problem, light-sheet techniques integrate optical sectioning ability with high-speed wide-field detection for 3D observation [23, 24]. However, wide-field detection is easily affected by tissue scattering leading to blurred images, thus not feasible for deep-tissue imaging.

To reduce the detrimental scattering effects, confocal and two-photon laser scanning microscopy seems to be good solutions. By using single-beam raster scanning with a single-channel detector (plus a pinhole in confocal system), tissue scattering effect is avoided within the detection process, since signals are captured at different timepoints pixel by pixel. It not only provides the optical sectioning ability, but also the intrinsic sub-micrometer spatial resolution [25, 26]. Between them, two-photon microscopy confines the excitation of fluorescence within focal volume, reducing photobleaching and phototoxicity effects compared to confocal microscopy. Besides, based on long-wavelength excitation, two-photon microscopy further provides longer penetration depth to ~millimeters [27]. Thus, two-photon laser scanning microscopy is chosen in this study.

1.2.3 Current limitation of two-photon microscopy: Speed

In general design of two-photon laser scanning techniques, they often equipped with a polygonal mirror [28] or resonant mirrors [29] for lateral scanning which can reach ~100 frames/s, but they were limited to 2D observation. Since neural network is



intrinsically a 3D structure, several two-photon volumetric techniques combining with axial imaging capabilities have been exhibited, such as liquid lens [30], piezoelectric actuator, [31], tunable acoustic gradient-index (TAG) lens [32], Bessel beam [33], acousto-optical deflector (AOD) [34] and remote focusing [35]. The first three methods demonstrate imaging speeds with only 10 volumes/s because they require raster scanning frame by frame sequentially to achieve volumetric imaging. Bessel-beam-based technique extending the beam shape along the axial direction for simultaneously excitation can reach 50 Hz volume rate, but it is limited to sparse samples to avoid overlapping of signal in the axial direction. AOD-based and remote focusing random-access techniques achieve ms-scale sampling of multiple points in 3D structure, but they are susceptible to motion artifact due to the property of partial sampling. Besides, abovementioned techniques mostly adopt a single-channel detector, such as a photomultiplier tube (PMT), for detection. Thus, the data acquisition rate is limited below ~ 500 MHz due to restriction of fluorescence lifetime (2-3 ns). All of them are hampered by the speed of scanning tools and the data acquisition rate of detector to reach ms-scale temporal resolution.

1.2.4 How to improve lateral scanning speed: Multifocal

To further break the limitation to improve imaging speed, one strategy is to increase the number of focus or enlarge excitation region simultaneously. For example, multi-focal methods [36], such as diffractive optical element (DOE) [37], spinning-disk [38] or micro-lens array [39] adopt multiple beams for parallel scanning simultaneously, which proportionally reduces the scanning duration. Besides, multi-photon wide-field illumination methods are demonstrated recently, such as two-photon light-sheet [40], holography [41] and spatial temporal focusing [42]. They feature wide-field excitation

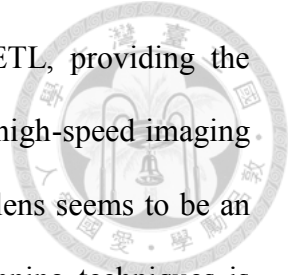
with a thin optical section or specific pattern, thus improving imaging speed by eliminating the need of lateral raster scanning. However, those methods are typically based on wide-field detection captured by a sCMOS camera or CCD, which again face the restriction of limited penetration depth caused by tissue scattering.

Therefore, from the above literature review, the viable choice is the combination of the multi-focal method and single-channel detection. The advanced multi-focal multi-photon microscopy using single-channel detector can reach thousands of frames per second [43], but it is limited to 2D lateral observation and the data acquisition rate is mainly restricted by lifetime of fluorescence (2-3 ns). To break through the limitation, the design may be further improved via adding multi-channel detectors [44]. Hence, we decide to use the multi-focal method collocating with a multi-channel detector to enhance the lateral scanning speed.

1.2.5 How to improve axial scanning speed: TAG lens

After determining the lateral scanning method, a suitable axial scanning tool is highly demanded for ms-scale volumetric imaging. From the above discussion, we mention various kinds of axial scanning components, such as piezoelectric actuator [31], liquid lens [30], electrically tunable lens (ETL) [45] and TAG lens [32]. From recent literature review, the application of a multi-focal method combining with a piezoelectric actuator attached on the objective lens for volumetric imaging was proposed [46]; however, the scanning speed of piezoelectric actuator is too slow with maximally ~100 Hz to achieve ms-scale temporal resolution. Although the scanning speed of liquid lens and ETL is one order higher than piezoelectric actuator which might be possible to reach our goal, considering the scanning time required for the lateral plane, there are only few planes within the volume instead of full sampling. In contrast, TAG lens offers ~100 kHz

scanning speed which is two-order faster than liquid lens and ETL, providing the capability of dense sampling. Since our goal is trying to develop a high-speed imaging technique without losing any information within the volume, TAG lens seems to be an appropriate choice for us. Detailed information of these axial scanning techniques is organized in Table. 1.2.2.



	Scanning speed	Characteristics
Piezoelectric actuator	~100 Hz	Few planes within the volume
Liquid lens	~1 kHz	Few planes within the volume
Electrically tunable lens	~1 kHz	Few planes within the volume
TAG lens	~100 kHz	Fully sampling for whole volume

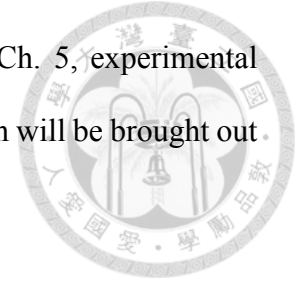
Table. 1.2.2 Organization of various axial scanning tools in terms of their scanning speed and characteristics.

1.3 Aim: Millisecond-scale volumetric imaging microscopy for *Drosophila* brain study

In this study, in order to capture the propagation of action potential inside whole *Drosophila* brain for *in vivo* functional study, we aim at developing a multi-focal two-photon volumetric imaging microscope, based on the combination of multi-focal method for lateral scanning speed enhancement and a TAG lens for ultrafast axial scanning, to achieve ms-scale volumetric imaging together with a sub-micrometer resolution. Collocating with a multi-channel detector, deeper penetration depth and larger data throughput can be further provided. This innovative design is expected to meet the requirements to fulfill our goal.

In the following chapter, principle of each techniques will be fully described in Ch.

2, and the setup of our system is shown in Ch. 3. In Ch. 4 and Ch. 5, experimental protocols and results are exhibited. Finally, discussion and conclusion will be brought out in Ch. 6 and Ch. 7 respectively for a brief summary.



Chapter 2. Principle of techniques for millisecond-scale volumetric microscopy



In this chapter, principle of each technique we chose will be explained thoroughly, including the mechanism of two-photon laser scanning microscopy, multi-focal method, TAG lens and how the combination of these techniques provide volumetric imaging modality.

2.1 Two-photon laser scanning microscopy

We will first elucidate the principle of two-photon absorption and then explain how laser scanning microscopy operates with the two-photon effect.

The concept of two-photon absorption was proposed by Maria Goeppert-Mayer in 1931. As its name implies, an electron of molecules absorbs two photons with an identical frequency to being excited from the ground state to the excited state, as shown in Fig. 2.1.1(a) [27]. After that, it spontaneously emits one fluorescent photon to decay back into ground state.

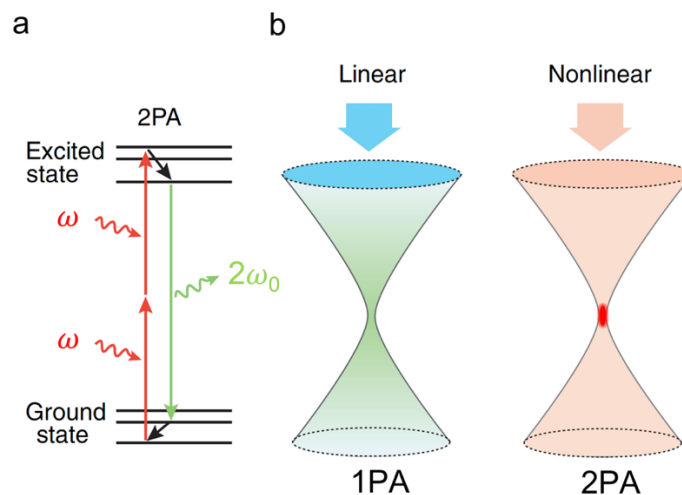
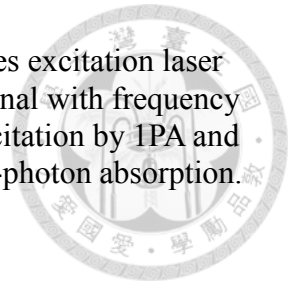
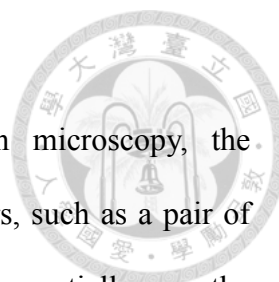


Fig. 2.1.1 Schematic of two-photon effect

(a) Two-photon absorption energy level diagram. Red light indicates excitation laser with a frequency ω and green line means the emitted fluorescent signal with frequency $2\omega_0$. ω is slightly larger than ω_0 . (b) Comparison between linear excitation by 1PA and nonlinear excitation by 2PA. 1PA, one-photon absorption; 2PA, two-photon absorption.



However, the probability of this phenomenon is extremely low because the electron needs to absorb two photons almost “simultaneously.” The probability can be defined by the absorption cross-section of the molecules which is named after Goepfert-Mayer, GM. One GM is 10^{-58} m⁴s/photon which means the probability to induce the two-photon effect is extremely low. To efficiently increase the probability of two-photon absorption, ultrahigh density photons are required with the means of confining photons both in a temporal and spatial region, such as a pulsed laser with a ~fs-scale pulse width. After converging the laser beam size into a $\sim\mu\text{m}^2$ size region by a convex lens, we possess the chance to induce two-photon absorption within this ultra-small focal region. Besides, two-photon absorption is a nonlinear process. The absorption probability is proportional to the square of the laser intensity ($S \propto I^2$; S, absorption probability; I, laser intensity), so that there is extremely small chance in the out-of-focus region to absorb two photons for excitation as a result of the lower laser intensity. As shown in Fig. 2.1.1(b), the single-photon absorption is a linear process which excites whole molecules within the cone volume, and in contrast, two-photon absorption only happens within the focal region, providing the capability of optical sectioning for volumetric imaging without the need to filter our out-of-focus signal. From the intrinsic property of optical microscopy, the focal size is in the order of laser wavelength [25], thus providing sub-micrometer resolution for biological applications. Moreover, owing to the fact that excitation wavelength of two-photon absorption, usually in the infrared region, is generally two-fold larger than that of single-photon absorption, the penetration length can be enhanced due to less scattering



effects.

In order to achieve volumetric imaging with two-photon microscopy, the conventional way is to use raster scanning. By steering the scanners, such as a pair of galvanometric mirrors, to control the position of the focus, it can sequentially scan the sample with “raster” shape to cover a whole layer of interest. As shown in Fig. 2.1.2, in general, the scanning sequence starts from x-y lateral plane and then to different layers by the movement of a sample stage or objective lens to achieve volumetric imaging. Since it is based on point-scanning for excitation, one common way of detection is to use a single-channel detector, such as a PMT, to collect the time-discernable signal pulse by pulse. Depending on how long the pixel dwell time is, the value of each pixel is assigned with the total accumulated signal by a detector. After combining with the information of total number of pixels, we can calculate the image speed accordingly. The two-photon laser scanning microscopy with the optical sectioning ability thereby provides the viability for volumetric imaging in deep tissue at cellular spatial resolution.

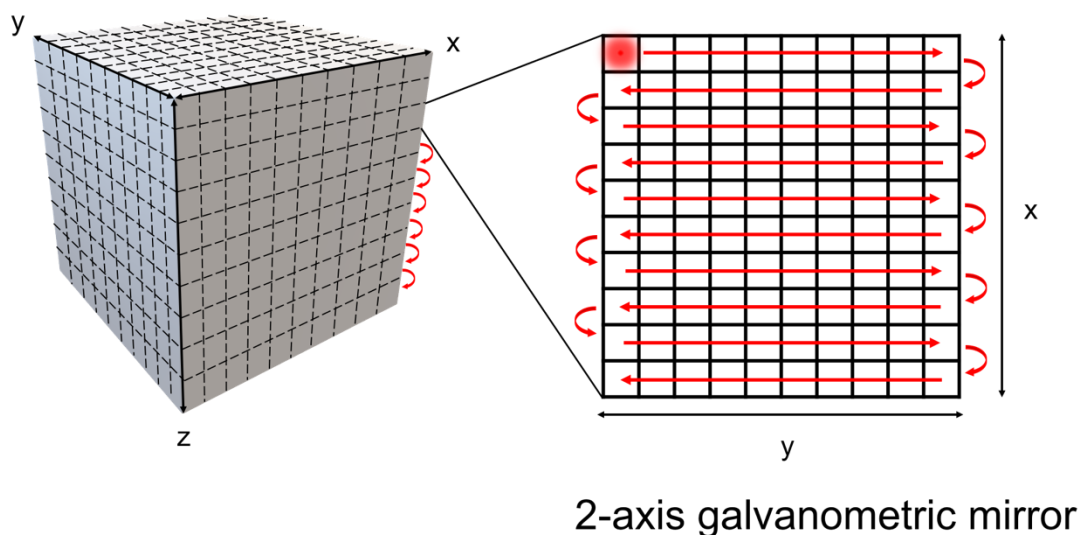


Fig. 2.1.2 Schematic of raster scanning to acquire a volumetric image

The raster scanning procedure generally starts from x-y lateral plane and then to different layers by moving the sample stage or objective lens sequentially.



2.2 Multifocal multiphoton microscopy

In subsection 1.2.4, we choose a multi-focal method to increase the number of beams for parallel scanning which proportionally reduces scanning time depending on how many beams were generated. There are several different kinds of splitting ways, including beam splitter, micro-lens array, spatial light modulator (SLM) and diffractive optical element (DOE). In this section, we will analyze the pros and cons of each method and explain why we chose DOE. Also, the mechanism of DOE will be described.

2.2.1 Common multifocal techniques

Beam splitter [47]:

By using several 50/50 beam splitters cascaded sequentially, even number of beams can be generated with high transmission rate approaching 90% and high splitting efficiency. However, the uniformity is relatively poor due to the discrepancy between transmission rate and reflection rate of beam splitter, resulting in nonuniform splitting and image brightness. Besides, strict alignment is required for this configuration, impeding the compatibility with other systems.

Micro-lens array [38, 39]:

This method employed a micro-lens array to split the incident laser with large beam-width into multiple small beam-width foci. Since the array is manufactured by placing several micro-lenses together, the spacing between each micro-lens causes additional power loss, resulting in relatively lower transmission rate and splitting efficiency. Moreover, the uniformity of each foci will be affected by the incident beam. For example, the most commonly used gaussian-shape incident laser leads to nonuniform power

distribution between the central part and the peripheral part.

Spatial light modulator (SLM) [48]:

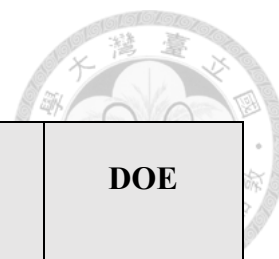
The SLM is constructed by plenty of liquid crystal elements aligning compactly as an array. By modulating the wavefront of the incident laser with phase-tuning, it can generate any specific pattern including multiple foci. Due to the delicate adjustment of SLM, high splitting efficiency and high uniformity of excitation beams can be achieved. However, SLM suffers from lower power damage threshold, especially for pulsed laser, which may restrict the application of two-photon microscopy.

Diffraction optical element (DOE) [37, 48]:

The DOE is based on diffraction to generate any required pattern. By imprinting specific microstructure on the base plate, the transmitted light can be reshaped into arbitrary distribution, such as a beam array. DOE can not only reach almost 99% transmission rate, ~1% nonuniformity and ~80% splitting efficiency, but also be easy to be integrated into the optical system. However, since the pattern is defined by the arrangement and shape of microstructure, the pattern is fixed once the DOE is manufactured, losing the freedom for pattern tuning.

Since high intensity laser power is required to induce two-photon effect for each splitting beam, transmission rate as high as possible is necessary. SLM may not be suitable to endure the laser power needed for splitting tens of beams. Beam splitter requires precise implementation and alignment. Micro-lens array causes too much power loss which will be a main concern. From the above criteria, it seems that although the splitting efficiency of the DOE is not optimal, high enough transmission rate and uniformity still meet our need, and the high compatibility serves as a suitable choice to integrate into our system. The organization of each method categorized by their pros and cons was provided in Table. 2.2.1.





	Beam splitter	Micro-lens array	SLM	DOE
Transmission rate	~90%	~50%	~95%	~99%
Splitting efficiency	~90%	~50%	~95%	~80%
Uniformity	Low	Low	High	High
Pros	High efficiency	Easy to fabricate	Tunable pattern	High compatibility
Cons	Require strict alignment	Large power loss	Low power damage threshold	Fixed pattern

Table. 2.2.1 Organization of possible choices for multi-focal method.

2.2.2 Diffractive optical element (DOE)

As we mentioned in previous section, DOE is based on diffraction for beam splitting, pattern generation or beam shaping. To give a clear demonstration, the DOE is made by mounting repetitive microstructure on the surface of base plate, as shown in Fig. 2.2.1 [49]. The shape of pattern is encoded within the microstructure, so that the transmitted light can be redistributed into a desired pattern and maintain subsequent propagation. For instance, the incident laser can be split into multiple collimated beams with a fixed divergent angle, as shown in the schematic. The number of beams and the divergent angle between each beam can be decided via simulation of the diffraction result in advance before manufacturing. One thing needs to be noticed is that once the DOE was made, it was not able to change the output pattern.

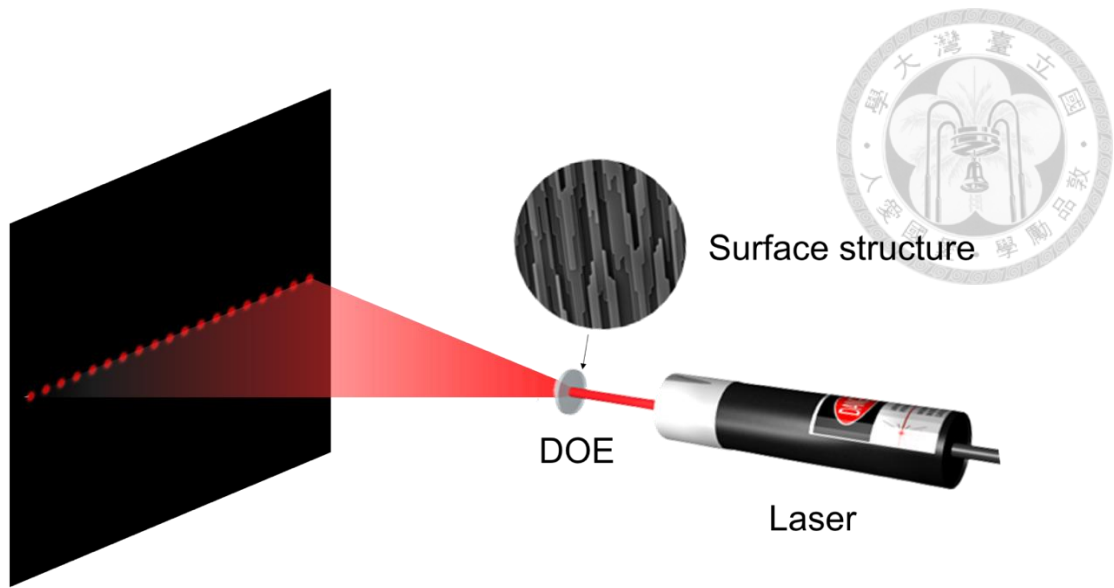


Fig. 2.2.1 Schematic of function of DOE

In this study, we customized a DOE to generate 32 beams lining up in one direction for parallel scanning. Compare to single beam raster scanning, the scanning time is reduced at least 32-fold. As shown in Fig. 2.2.2, by using multi-focal and a single axis galvanometric mirror for parallel scanning in lateral direction, the imaging speed of volumetric imaging can be significantly improved.

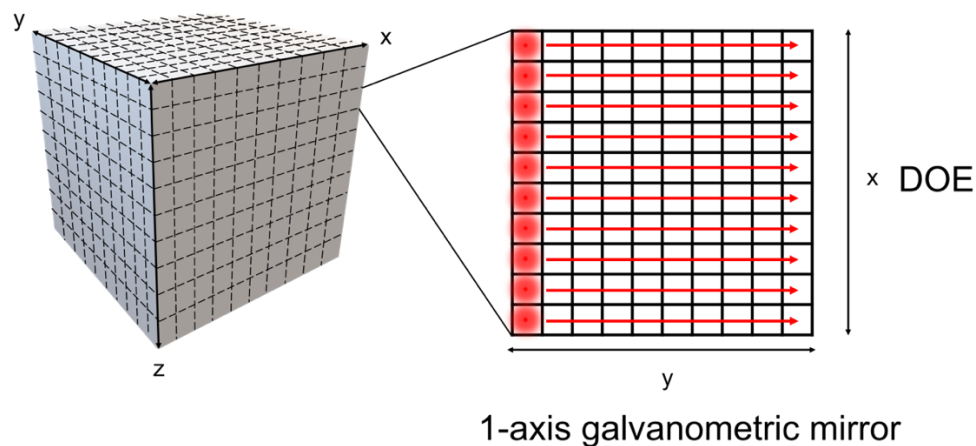


Fig. 2.2.2 Schematic of raster scanning combining with the multi-focal method
The scanning time can be reduced, and thus the imaging speed increases accordingly.

2.3 TAG lens

TAG lens is the abbreviation of tunable acoustic gradient-index lens. Using acoustic-optic effects, TAG lens provides the capability to manipulate the wavefront of incident light by tuning the acoustic wave inside the lens. The internal structure of the TAG lens is shown in Fig. 2.3.1 [50]. In the central part of the TAG lens, a container filled with specific medium (silicone oil in this TAG lens) is surrounded by a ring-shape transducer and metallic housing at the outer surface. When we import sinusoidal voltage signals into the TAG lens to driven the transducer, it will convert it into vibration motion to generate acoustic wave in the medium. The acoustic wave thus creates a periodic density and refractive index (RI) variation in both time and space domains inside the medium of the TAG. The RI variation is approximated and described by

$$n(r, t) = n_0 + n_\alpha J_0\left(\frac{\omega r}{v}\right) \sin(\omega t) \quad (2.1)$$

where r is the spatial coordinate along lens radius, t is the temporal coordinate, n_0 is the static RI, n_α is the maximum RI variation as the lens is operating, J_0 is a Bessel function of the first kind, ω is the driving frequency, and v is the sound speed in the lens media [51]. Due to the variation of RI inside the TAG lens, when an incident beam passes through the TAG lens, the wavefront of the beam changes according to different states of the TAG lens. At specific operation frequency of the input driven signal, the acoustic wave produces a standing wave inside the TAG lens and two representative operating states happened at the two endpoints of standing wave are shown in Fig. 2.3.1(b) and (c).

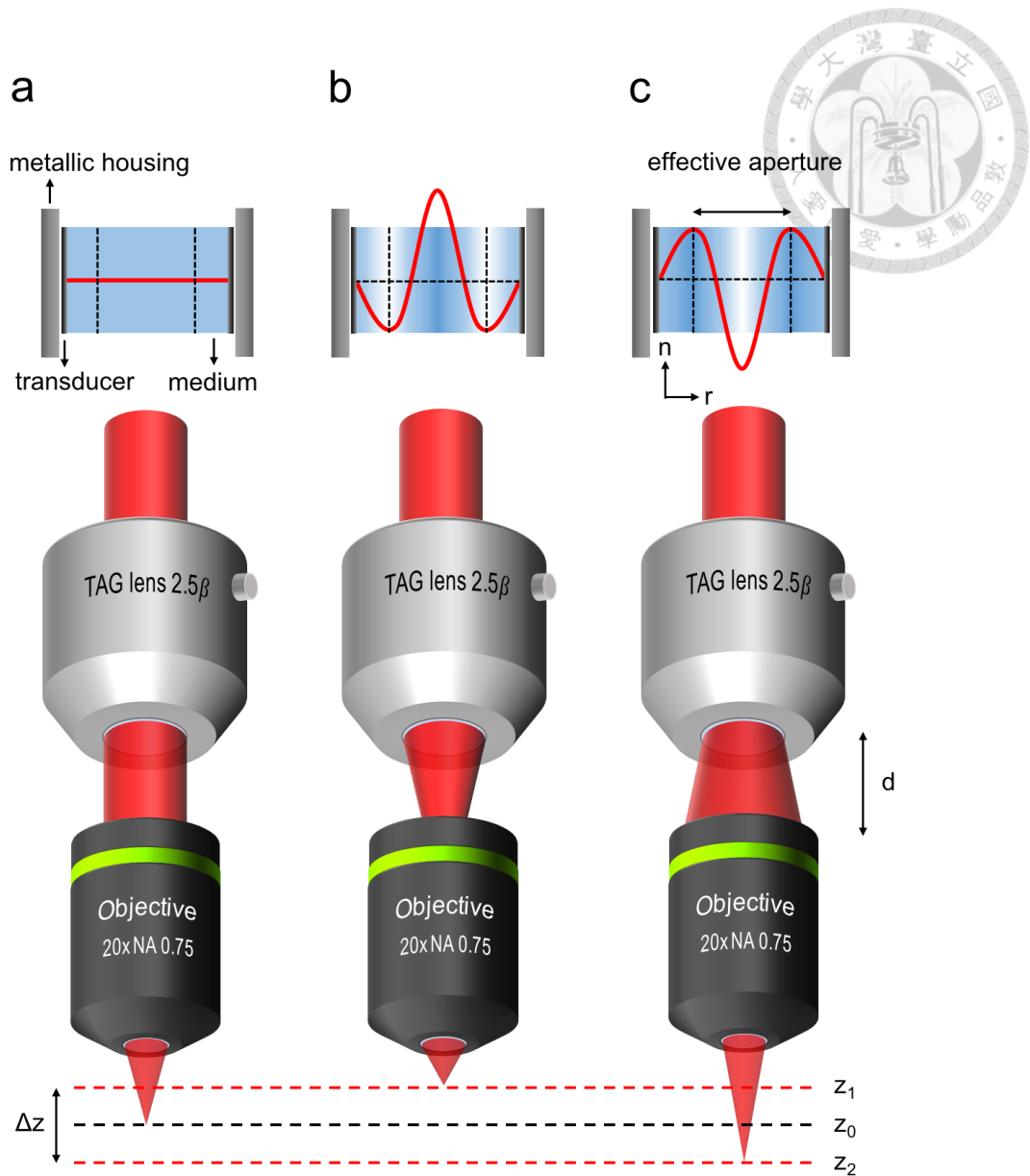


Fig. 2.3.1 Schematic showing the operation of the TAG lens and how the combination of the TAG lens and the objective lens achieves axial scanning

- (a) When the TAG lens is turned off, it just acts like a cylinder with a uniform medium. Therefore, the incident beam remains collimated and forms a focus at z_0 image plane after objective lens. (b) When the TAG lens is turned on, it acts like a convex lens, and the incident beam converges and forms a focus at z_1 image plane after objective lens. (c) When the TAG lens is operating at the other state, it acts like a concave lens, and the incident beam diverges and forms a focus at z_2 image plane after objective lens. The distance between z_1 and z_2 represents the axial scanning range of the TAG lens (Δz). n , refractive index; r , spatial coordinate along lens radius; d , distance between the TAG lens and objective lens.

When the TAG lens is turned off, as shown in Fig. 2.3.1(a), it just acts like a

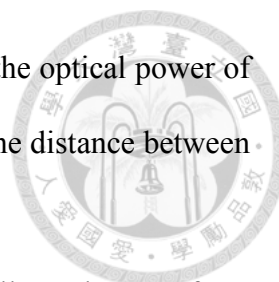
cylindrical container with a uniform RI medium. As the incident beam passes through the TAG lens, it remains collimated. When the TAG lens is turned on with the acoustic standing wave forming local maximal RI at the central point, as shown in Fig. 2.3.1(b), the TAG lens acts like a convex lens. Therefore, the incident beam converges after passing through the TAG lens. On the contrary, when the TAG lens is operating with the acoustic standing wave forming local minimal RI at the central point, as shown in Fig. 2.3.1(c), the TAG lens acts like a concave lens. Hence, the incident beam diverges after passing through the TAG lens.

After combining with an objective lens placing right after the TAG lens, the incident beam forms a focus at the imaging plane of objective lens. With different operating states of the TAG lens, the alteration of beam convergence leads to different focus depths. As shown in Fig. 2.3.1, the stationary state of the TAG lens forms a focus at z_0 image plane, and the operating states of the TAG lens at two endpoints case form the focus at z_1 and z_2 image plane respectively. The distance between z_1 and z_2 represents total axial scanning range (Δz). Since the driven frequency of the TAG lens operates at ~ 70 kHz, it looks like the focus scans at the axial direction with ~ 70 kHz scanning speed.

To know the theoretical axial scanning range (Δz) of this configuration, we can simply assume that the TAG lens is a lens with tunable focal length and optical power ranging from δ_{TAG} to $-\delta_{TAG}$ due to the symmetric property of sinusoidal wave. Via simple calculation of geometric optics using the parameters of the TAG lens and objective lens, the axial scanning range can be described as

$$\Delta z = |z_1 - z_2| = \frac{2f_{tube}^2\delta_{TAG}}{M^2 - \delta_{TAG}^2(Md - f_{tube})^2} = \frac{2\delta_{TAG}}{\delta_{obj.}^2 - \delta_{TAG}^2(\delta_{obj.}d - 1)^2} \quad (2.2)$$

where f_{tube} is the tube length used to collocated with objective lens, M is the



magnification factor between tube lens and objective lens, δ_{TAG} is the optical power of the TAG lens, δ_{obj} is the optical power of objective lens, and d is the distance between the TAG lens and the objective lens [52].

One thing needs to be noted is that the standing wave spatially follows the waveform of Bessel function, and thus only the region within the pair of locations with local minimal RI in Fig. 2.3.1(b) or within the pair of locations with local maximal RI in Fig. 2.3.1(c) can function properly, which is defined as the effective aperture (EA) of the TAG lens. If the incident beam passes through the TAG lens with different beam widths, the axial extension profile changes due to the different portion coverage of the TAG lens effective aperture, as shown in Fig. 2.3.2 [51].

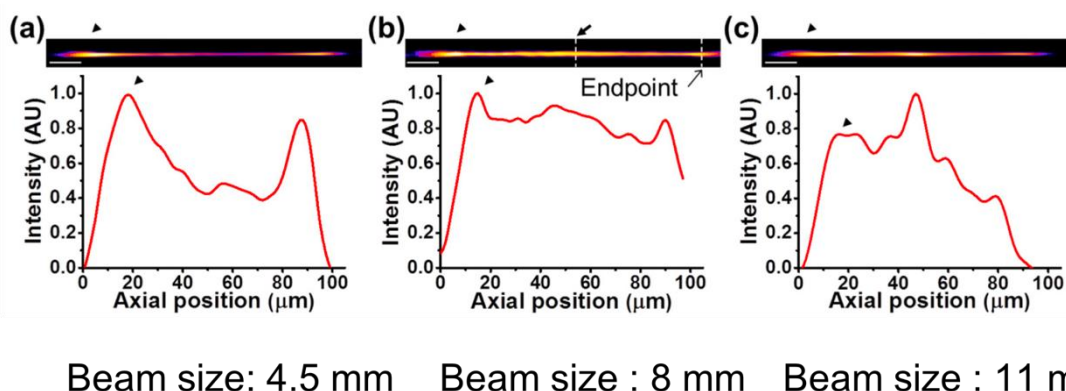


Fig. 2.3.2 Axial extension of the TAG lens with different incident beam sizes

(a)-(c) are axial intensity distributions with corresponding xz images characterized by 80-nm gold nanoparticles. The incident beam sizes in front of the TAG lens are (a)~4.5, (b)~8, and (c)~11 mm, respectively,

2.4 Two-photon volumetric imaging microscopy

In brief summary, we choose multi-focal method using a DOE for parallel scanning to enhance the lateral scanning speed and a TAG lens to achieve axial scanning. The lateral imaging plane (x-y plane) is achieved by a single-axis galvanometric mirror. To

give an overall demonstration of the volumetric imaging, the schematic is shown in Fig. 2.4.1 with x, y and z direction corresponding to a DOE, the galvanometric mirror and the TAG lens respectively. Because the scanning frequency of the TAG lens is much higher (~70 kHz) than galvanometric mirror (~1 kHz), instead of scanning from the lateral imaging plane first (x-y plane), such as Fig. 2.1.1, the scanning sequence starts from vertical imaging plane (x-z plane in this scheme) and then move to adjacent vertical plane by the galvanometric mirror subsequently to achieve volumetric imaging.

1-axis galvanometric mirror

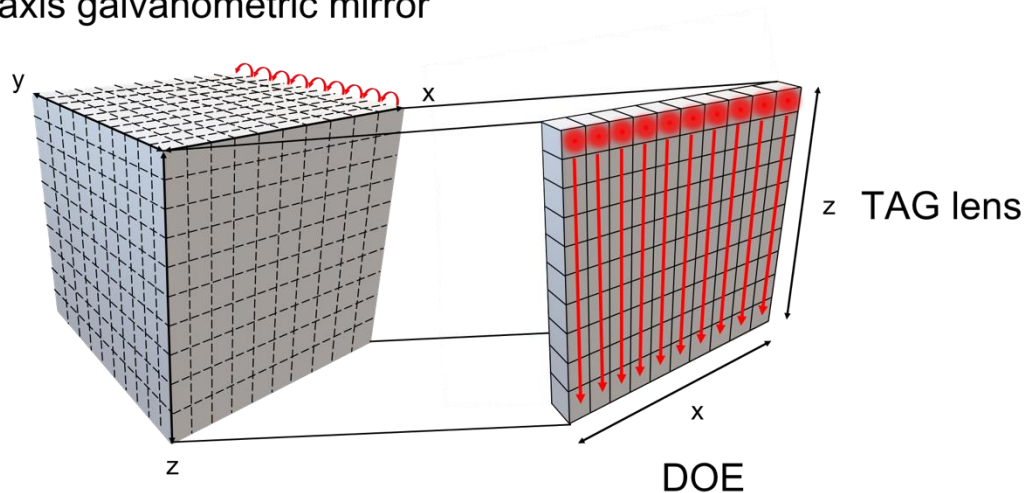


Fig. 2.4.1 Schematic of raster scanning combining with a multi-focal method and the TAG lens to achieve volumetric imaging

X direction is covered by a DOE, y direction is scanned by a galvanometric mirror and z direction is scanned by the TAG lens.

Chapter 3. System design of millisecond-scale volumetric imaging microscopy



In this chapter, detailed information about how we constructed our system will be clearly demonstrated, including the setup, contrast agent, the wavelength of laser and every optical component we used. In the end, some theoretical system performances will also be calculated, including the spatial resolution, the size of volume and the volumetric imaging speed.

3.1 Optical setup

In the beginning, we will start from our setup and then follow the sequence of light path to introduce every component, from excitation to emission. The overall schematic of our setup is shown in Fig. 3.1.1.

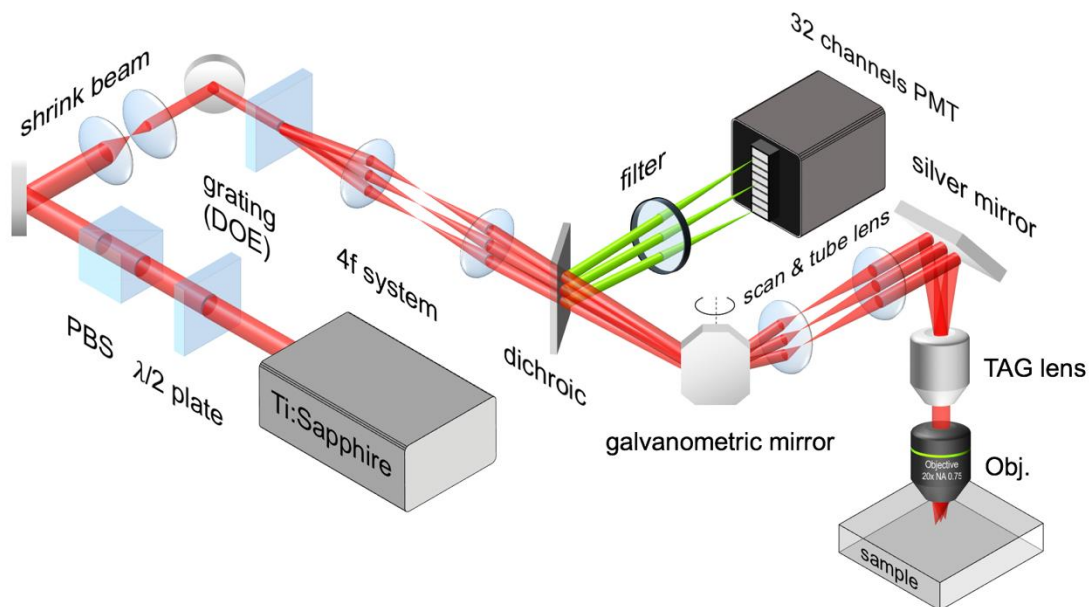
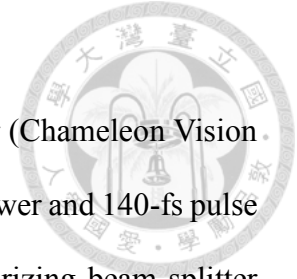


Fig. 3.1.1 Schematic of our system

See the main text for detailed information of each component and principle. PBS, polarizing beam splitter; DOE, diffractive optical element; TAG, tunable acoustic gradient-index; Obj., objective; PMT, photomultiplier tube. Please note that the image is not in real scale. Image courtesy: G.-J. Huang.

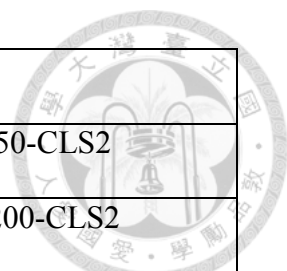


A 940 nm beam was generated from a Ti:Sapphire pulsed laser (Chameleon Vision II, Coherent) with an 80-MHz repetition rate, ~1.4-W laser output power and 140-fs pulse width. One pair of half wave plate (10RP52-4, Newport) and polarizing beam splitter (PBS253, Thorlabs) were used for tuning laser power. Followed by one pair of beam-shrinkers (AC254-150-B-ML, AC254-50-B-ML, Thorlabs), beam size could be adjusted to match the effective aperture of the TAG lens. The excitation laser was sent through a diffractive optical element (DOE, Holo/Or) to form 32 collimated beams, which were then relayed by a 4f system (AC254-100-B-ML, AC254-150-B-ML, Thorlabs) onto a pair of galvanometric mirrors (6215HM40B, Cambridge Technology) for lateral scanning. The scanning direction was orthogonal to the splitting direction of the DOE, forming a transverse 2D plane. After that, these scanning beams were projected by a telecentric scan and tube lens pair (SL50-CLS2, TL100-CLS2, Thorlabs) onto the back aperture of an objective lens (HC PL IRAPO 20x, NA=0.75, water immersion, Leica) to form a multi-lines image. Maximum laser power after the objective lens could reach 300 mW, while typically 120 mW was used in the experiment. For high-speed axial scanning, a TAG lens (TAG Lens 2.5β , TAG Optics Inc.) was placed right before the objective lens to alter the wavefront of 32 beams simultaneously. Thus, on the imaging plane of objective lens, 32 focal spots moved up and down at ~70 kHz for axial scanning according to different states of the TAG lens.

The emitted fluorescent signal was epi-detected by the same objective lens, de-scanned by the galvanometric mirror and separated by a dichroic mirror (DMLP650R, Thorlabs). Via a de-scanning method, we can make sure that the fluorescent signal remains stationary for detection. Two pieces of band-pass filters (FF01-520/15-25, Semrock & FBG39-2IN-SP, Thorlabs) are applied before the detector to filter out laser

and detrimental background signals. Because 32 spots of fluorescent signals emitted simultaneously, instead of employing the commonly used single-channel PMT detection, we adopted a 32-channel linear PMT (H12175-200, Hamamatsu) which is constructed by an array of single-channel PMTs. Each channel corresponds to each beam. In our system, chromatic aberration appears as an unignorable effect, since the wavelength of excitation signals (940 nm) and emission signals (520 nm) has a large discrepancy with regard to the objective lens. We found that after fluorescent signals were de-scanned for such a long distance, it gradually converged instead of remaining collimated. Therefore, with finely tuning of the distance between beam shrinkers, we can control the position of focal plane of 32 fluorescent spots to precisely match the spacing of 32-channel PMT. The beam size of each focal spot (438 μm at $1/e^2$ width) has been verified to be smaller than the geometric size of each channel (800 μm). The company and model number of each instrument are listed in Table. 3.1.1.

Instrument	Company	Model number
Laser	Coherent	Chameleon Vision II
Half wave plate	Newport	10RP52-4
Polarizing beam splitter	Thorlabs	PBS253
Beam shrinker(front)	Thorlabs	AC254-150-B-ML
Beam shrinker(back)	Thorlabs	AC254-50-B-ML
Diffractive optical element	Holo/Or	Customized 32-beam splitter
4f system(front)	Thorlabs	AC254-100-B-ML
4f system(back)	Thorlabs	AC254-150-B-ML
Dichroic	Thorlabs	DMLP650R
Galvanometric mirrors	Cambridge	6215HM40B



	Technology	
Scan lens	Thorlabs	SL50-CLS2
Tube lens	Thorlabs	TL200-CLS2
Silver mirrors	Newport	20D620ER.2
TAG lens	TAG Optics Inc.	TAG Lens 2.5 β
Objective lens	Leica	HC PL IRAPO 20x/0.75 W
3-axis stage (sample stage)	Thorlabs	MAX313D
Reflective mirrors	Thorlabs	BB1-E03
Band-pass filter	Semrock	FF01-520/15-25
Band-pass filter	Thorlabs	FBG39-2IN-SP
32-channel PMT	Hamamatsu	H12175-200
Single-channel PMT	Hamamatsu	H5782-20
sCMOS camera	ANDOR	Neo 5.5

Table. 3.1.1 List of each instrument with the information of company and model number.

3.2 Contrast agent and excitation wavelength

In this study, our purpose is trying to capture the propagation of action potential in neural network. Nowadays, voltage sensitive agents or indicators are developed [53]. Due to its fast response (~ 10 ms) to membrane voltage variation, we can monitor transient dynamics of neural networks immediately. However, before we proceed to that step, we need to test whether our system is applicable to observe the fluorescent signal of *Drosophila* brain. Thus, proper indicator as bright as possible is demanded, and the brightness is primarily determined by the two-photon cross-section of the fluorescence

indicator. Among several kinds of fluorescence proteins, enhanced green fluorescent proteins (eGFP) are one of the suitable and mature candidate which possesses large two-photon cross-section [54], and thus was used in the experiment. The two-photon cross-section of eGFP versus the laser wavelength was provided in Fig. 3.2.1 [54]. The peak appears at around 927 nm.

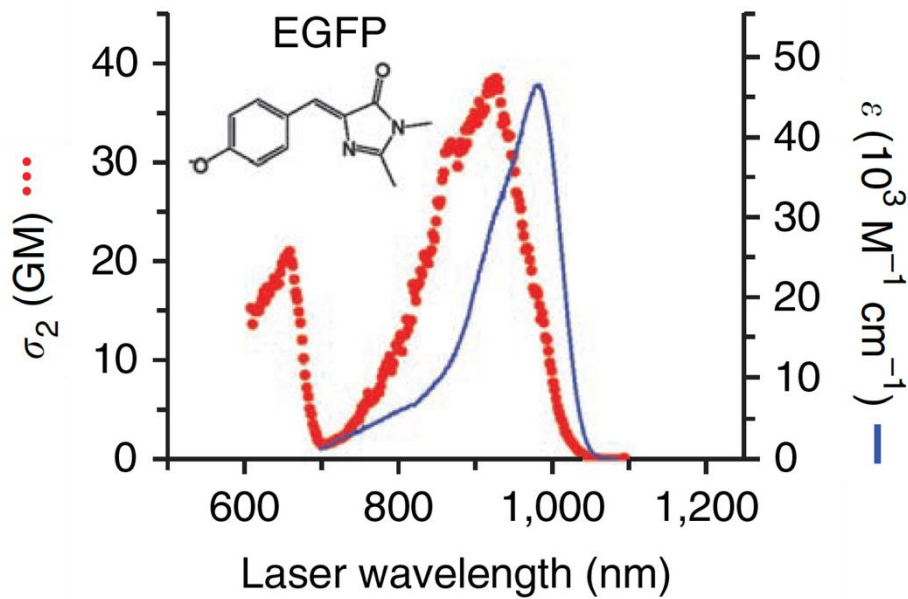


Fig. 3.2.1 Two-photon absorption cross-section (σ_2) of eGFP versus laser wavelength. For the purpose of comparison, the one-photon absorption cross-section spectrum (ϵ) shown in the figure is multiplied the original spectra with a factor of two [54].

However, instead of using 927 nm as the excitation wavelength, we found that there is a strong absorption peak of the TAG lens at around 910 nm [55]. The transmission spectrum of the TAG lens, as shown in Fig. 3.2.2, was measured by our previous lab member, Kuo-Jen Hsu [56]. This phenomenon induces not only unnecessary power consumption but also additional aberration due to nonuniform heating of the material (silicone oil) inside the TAG lens which might distort the wavefront of the transmission laser. Detailed discussion will be brought forward in section 6.1. Thus, in order to avoid absorption of the TAG lens and still maintain high enough absorption efficiency of eGFP

at the meantime, 940 nm was chosen as the excitation wavelength to strike a balance.

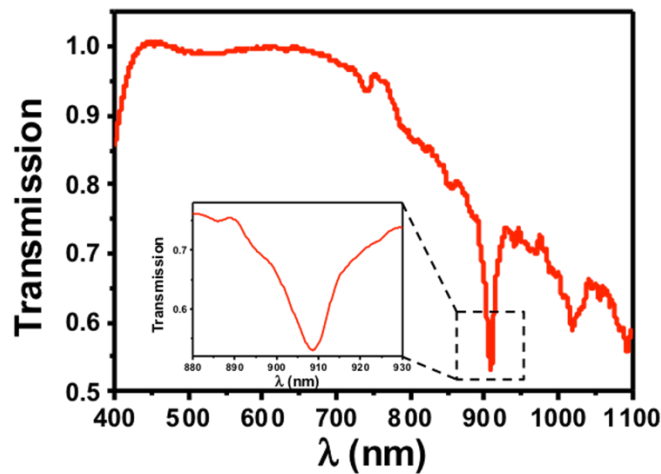


Fig. 3.2.2 Transmission rate of the TAG lens with different incident wavelengths

Image courtesy: Kuo-Jen's doctoral dissertation.

3.3 Selection of each component

In this section, the reason for the selection of important components will be comprehensively discussed and explained, including the DOE, the TAG lens, the PMT, the amplifier and the entire data acquisition (DAQ) system.

3.3.1 DOE

First, DOE plays an important role in this study because the concept of multi-focal is one of the key designs. From subsection 2.2.2, we already knew that once the DOE was fabricated, parameters, such as foci number and splitting angle, were fixed. Therefore, we need to determine those parameters in advance, which is highly related to the biological characteristics of our target, *Drosophila*. The general size of *Drosophila* brain is about $200 \times 700 \mu\text{m}^2$. To achieve whole brain imaging without missing any neurons, the shorter side of a *Drosophila* brain ($200 \mu\text{m}$) should be totally covered by multi-foci, and every

neuron should be at least scanned by one excitation beam. Given that the general size of *Drosophila* brain neuron is about 6 μm [12], we can deduce that there are about 32-33 neurons in the shorter side of a *Drosophila* brain which means the foci number should be at least 32 to fulfill the requirement.

From the discussion in subsection 1.2.4, a multi-channel PMT is necessary for detection to achieve deep tissue imaging. Thus, the number of foci should also collocate with the number of PMT channel among existing commercial products. After carefully searching for commercial PMT modules, multi-channel PMTs from Hamamatsu company have the potential to fit our purpose. They provide PMT modules with 8, 16, 32 and 64 channels, and from the above discussion, 32-channel PMT appears as a great choice. Therefore, the DOE was customized by Holo/Or company to generate 32 foci with 6.875 degree splitting angle. Combining with the 4f system, scan lens, tube lens and objective lens, it perfectly forms 32 foci with 200- μm full spacing on the imaging plane of objective lens. The calculation is shown as below.

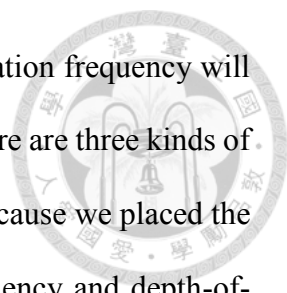
$$\begin{aligned} \text{Full spacing} &= f \times \theta_1 \times m_1 \times m_2 \\ &= 10 \text{ mm} \times 6.875 \times \frac{\pi}{180} \times \frac{100}{150} \times \frac{50}{200} = 200 \text{ } \mu\text{m} \end{aligned} \quad (3.1)$$

f , focal length of objective lens; θ_1 , radius of splitting angle; m_1 , magnification factor of 4f system; m_2 , magnification factor of scan lens and tube lens.

The transmission rate of the DOE approached 99% with about 80% splitting efficiency which should be high enough to generate 32 foci.

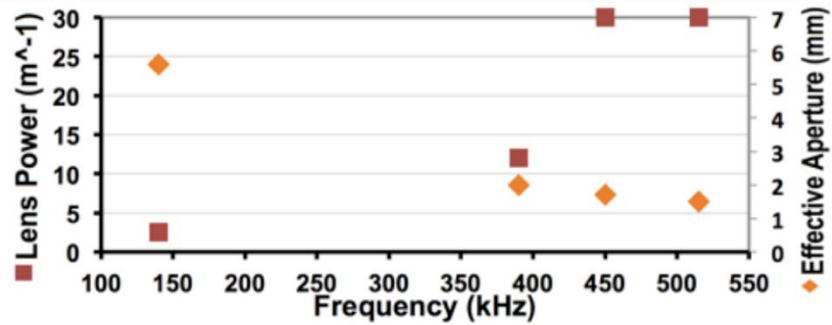
3.3.2 TAG lens

TAG lens acts as another important tool because it determines the extension of axial

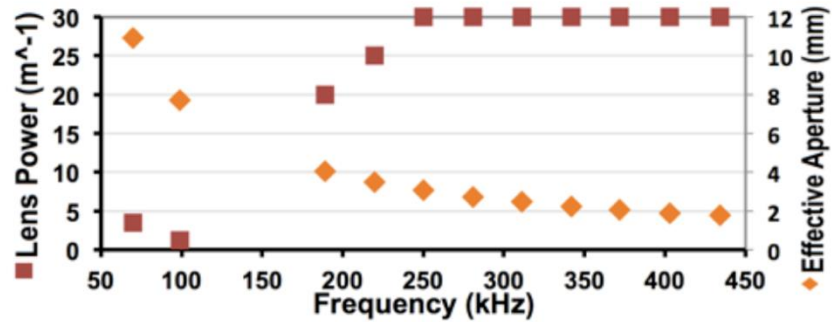


scanning. Besides, from the discussion in section 2.4, different operation frequency will affect the imaging speed. From the catalog of TAG lens company, there are three kinds of TAG lenses with different properties, as shown in Fig. 3.3.1 [57]. Because we placed the TAG lens in front of the objective lens to optimize collection efficiency and depth-of-field extension [51], from this viewpoint, the first thing we should take into consideration is the effective aperture of the TAG lens. If the aperture is smaller than objective lens, part of the incident beam will be blocked, resulting in lower NA and worse spatial resolution. The back aperture of the objective lens we are using now is about 16 mm. From Fig. 3.3.1, the closest option is TAG Lens 2.5β with maximal 11 mm which supposes to be the best choice, although the spatial resolution will be slightly sacrificed. Even though there is only one choice, we still need to verify whether the axial extension and operation frequency meet our requirement. The total optical lens power is 2 m^{-1} , and from the equation of axial extension calculation showed in section 2.3, combining with a $20\times$ objective lens with 10 mm focal length, the theoretical extension can reach $200 \mu\text{m}$ which should be deep enough to cover *Drosophila* brain. Detailed calculation will be mentioned in subsection 3.4.2. The other important parameter is operation frequency. In our design, the scanning period of the TAG lens is inversely proportional to imaging speed. In order to fulfill high speed imaging, the operation frequency should be as high as possible. However, the operation frequency is limited to 70 kHz. Although there is no more chance to further improve the imaging speed by changing operation frequency of the TAG lens, the current imaging speed can already reach ~ 500 volumes/s which will be discussed in subsection 3.4.3.

TAG Lens 2.0



TAG Lens 2.5β



TAG Lens HPβ

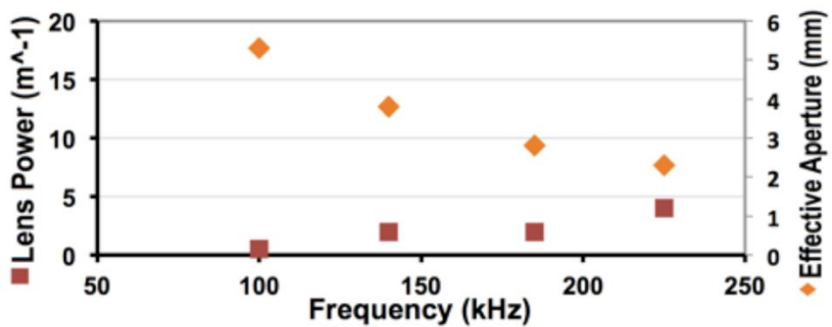


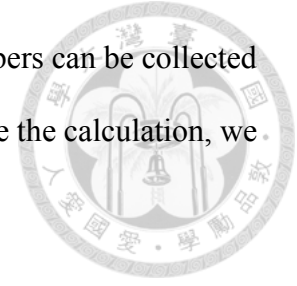
Fig. 3.3.1 TAG lens family

Right figure shows the lens power and effective aperture versus operation frequency of TAG Lens 2.0, TAG Lens 2.5β and TAG Lens HPβ from top to bottom.

3.3.3 Photomultiplier tube (PMT)

From the above discussion, we choose a multi-anode PMT as our detector. In order to select suitable one, the criterion is the quantum efficiency (QE), which means the conversion factor between the incident photon number and emitted electron number. PMT with QE as high as possible is preferable to detect weak signals. To know how large the QE of PMT we should choose, we need to strictly calculate two-photon excitation

efficiency of our system in advance to know how many photon numbers can be collected by our detector. The estimation method is provided from [58]. Before the calculation, we list definitions of several parameters below.



$n_{\text{pulse}}^{\text{incident}} \equiv$ Number of incident photons per laser pulse (photons/pulse)

$n_{\text{pulse}}^{\text{collect}} \equiv$ Number of photons collected by the objective lens per laser pulse

$P_{\text{average}}^{\text{incident}} \equiv$ Average power of incident laser (J/s)

$\Phi_{\text{pulse}}^{\text{incident}} \equiv$ Intensity of incident photons (photons/m²/s)

$\tau_{\text{pulse}} \equiv$ Width of laser pulse (140 fs)

$\sigma_{\text{dye}} \equiv$ Cross section of fluorescent indicator

$\xi_{\text{obj}} \equiv$ Collection efficiency of objective lens

$N_{\text{molecules}} \equiv$ Number of molecules within focal excitation volume

$\Gamma \equiv$ Repetition rate of laser pulses (80 MHz)

$h \equiv$ Planck's constant (6.6×10^{-34} J·s)

$\beta^2 \equiv$ Relative variance of laser intensity, $\langle \Phi_{\text{pulse}}^{\text{incident}^2} \rangle / \langle \Phi_{\text{pulse}}^{\text{incident}} \rangle^2$

$N_a \equiv$ Avogadro's number (6×10^{23} molecules/mole)

[dye] \equiv Molar concentration of the fluorescent indicator

$\omega \equiv$ Radius of beam at the focus ($1/e^2$)

$z \equiv$ Beam diameter in axial direction

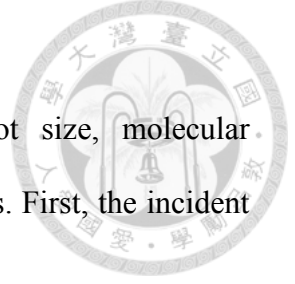
$V_{\text{excitation}} \equiv$ Optical excitation volume

$\lambda \equiv$ Center wavelength of laser (940 nm)

NA \equiv Numerical aperture of the objective lens (effective NA = 0.572)

$n \equiv$ Refractive index (1.33 for water)

$c \equiv$ Speed of light (3×10^8 m/s)



The calculation starts from excitation intensity, focal spot size, molecular concentration and then converging to the number of emitted photons. First, the incident photons per laser pulse is

$$n_{pulse}^{incident} = \frac{\lambda}{hc} \times \frac{P_{average}^{incident}}{\Gamma}. \quad (3.2)$$

In our system, maximum laser power after objective lens was about 300 mW. Therefore, each beam has about 10 mW average laser power ($P_{average}^{incident}$). Substitute related parameters into the equation, we can get

$$n_{pulse}^{incident} = 5.9 \times 10^8 \text{ photons/pulse}. \quad (3.3)$$

The radius of focal size can be defined as,

$$\omega = \frac{1}{\pi} \times \frac{\lambda}{NA} = 523 \text{ nm} \quad (3.4)$$

and beam diameter in axial direction can be defined as well [25],

$$z = \frac{2 \times 0.532\lambda}{n - \sqrt{n^2 - NA^2}} = \frac{2 \times 0.532 \times 940}{1.33 - \sqrt{1.33^2 - 0.572^2}} = 7.76 \text{ } \mu\text{m}. \quad (3.5)$$

From the combination of beam radius and beam diameter in axial direction, focal volume can be deduced as,

$$V_{excitation} = \frac{4}{3}\pi \times \omega^2 \times \frac{1}{2} \times z_{confocal} = 4.45 \times 10^{-15} \text{ L}. \quad (3.6)$$

Now, we are able to acquire incident photon intensity via dividing incident photons

by focal cross-section area and pulse width,

$$\Phi_{pulse}^{incident} = n_{pulse}^{incident} \times \frac{1}{\pi\omega^2\tau_{pulse}} = 4.9 \times 10^{33} \text{ photons/m}^2/\text{s}. \quad (3.7)$$



We also need the cross-section of the fluorescent probe. The cross-section of most widely used enhanced green fluorescent protein (eGFP) varies from 20 GM (10^{-58} m⁴s/photon) to 300 GM [59] which is tested under different excitation wavelengths. Without loss of generality, we choose 180 GM (average) at 960 nm which is close to the wavelength we used.

Number of molecules inside focal excitation volume is

$$N_{molecules} = [dye]N_aV_{excitation}. \quad (3.8)$$

The molar concentration of eGFP in *Drosophila* tissue was measured at about 1 μM [60]. Thus, we can get

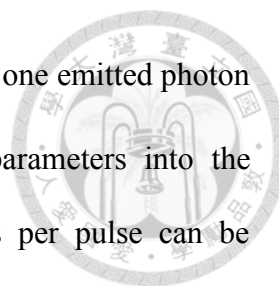
$$N_{molecules} = 2667. \quad (3.9)$$

We also need to calculate epi-fluorescent collection efficiency using the same objective lens,

$$\xi_{obj} = \frac{1}{4} \left(\frac{NA}{n} \right)^2 = 0.0866 = 8.66\% \quad (3.10)$$

Finally, the emitted photons collected by the objective lens can be deduced as,

$$n_{pulse}^{collect} = \xi_{obj} \times \frac{1}{2} \times \sigma_{dye} \times \beta \times \langle \Phi_{pulse}^{incident} \rangle^2 \times \tau_{pulse} \times N_{molecules}. \quad (3.11)$$



The $\frac{1}{2}$ comes from the conversion of two incident photons into one emitted photon and the normalized variance $\beta = 0.664$ [61]. Substituting all parameters into the equation, the emitted photon number collected by objective lens per pulse can be estimated as,

$$n_{pulse}^{collect} = 4.6 \text{ photons/pulse.} \quad (3.12)$$

However, that is total emitted photons collected by objective lens. In order to estimate number of incident photons on the detector, transmission rate for lenses and reflection rate for mirrors of 520 nm fluorescent signal of each component within the de-scanned light path should be taken into consideration. The transmission rate of each component is showed in Table. 3.3.1 in sequence.

Component	Transmission/Reflection
Objective lens	92%
TAG lens	92%
A pair of silver mirrors	92%
Tube lens	95%
Scan lens	93%
A pair of galvanometric mirrors	92%
Dichroic	99.5%
E02 mirror	99.5%
Filter	99.9%
Total	63%

Table. 3.3.1 Transmission rate of each optical component.

Thus, number of incident photons on the detector should be modified as $4.6 \times 0.63 = 2.9$ photons/pulse. In order to guarantee that we could acquire signals from each laser pulse, the emitted electron per pulse should be at least larger than one. From the inverse of the incident photon per pulse, minimum quantum efficiency of PMT should exceed $1/2.9 = 0.345 = 34.5\%$. However, from the spectral response of different material type for multi-anode PMT showed in Fig. 3.3.2 [62], the maximal QE at 520 nm is -200 type with about 20% QE. Although it doesn't meet our requirement, the QE is still close to it. Therefore, in this study, we choose Hamamatsu H12175-200, which is a 32-channel PMT, as our detector. To deal with the situation of insufficient emitted photons, several aspects regarding how to improve emitted photon number will be discussed in section 6.2.

Figure 1: Typical Spectral Response

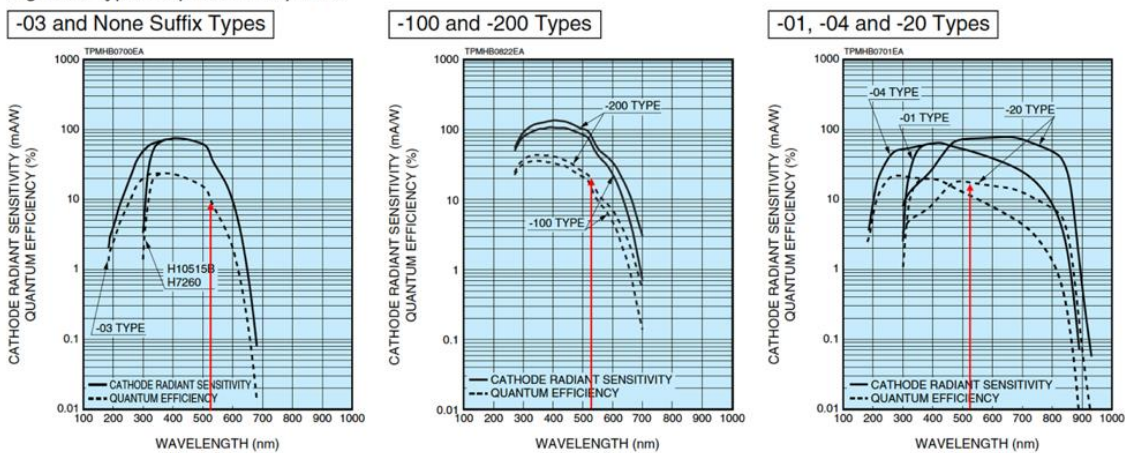
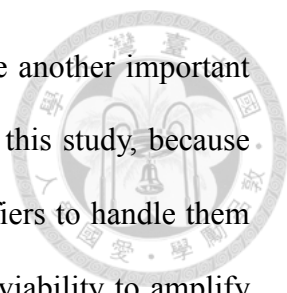


Fig. 3.3.2 Quantum efficiency of different types of material for multi-anode PMT

3.3.4 Amplifier (AMP)

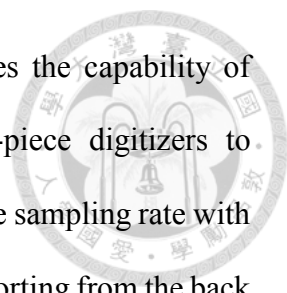
Although PMT can already transform detected fluorescence photons into usable current signals, in general, the magnitude of current output is in the order of $\sim \mu\text{A}$ which is too weak for data acquisition. In order to gather strong enough signal, an amplifier is necessary within the process of data acquisition to magnify the output signals of PMT.



Besides, appropriate magnification factor of amplifier appears to be another important issue to collocate with following instrument, such as a digitizer. In this study, because there are 32 streams of output signal from PMT, we need 32 amplifiers to handle them separately. However, most commercial amplifiers only provide the viability to amplify single-channel signals. If we use 32 single-channel amplifiers at the same time, the design would be quite bulky and definitely cost a lot. To handle this problem, we adopt the choice of surface mount amplifier which is small and cost efficient. We choose ERA-3SM+ as our amplifier which has about 23.5 dB gain (~15 folds) and 3 GHz operation bandwidth, capable of amplifying the ~ns-scale output current signals of PMT without enlarging the temporal response of signals. With the assistant of SouthPort Co., Ltd, we customized an amplifier board with 32 amplifiers mounted on it to convert the current input into voltage signals with 100 Ω resistance and then amplify each channel individually.

3.3.5 Data acquisition system (DAQ)

After the fluorescent signal was captured by the PMT, converted into current signals and then magnified with an amplifier, we certainly need to record the value by a digitizer and store it into hard-disk for image reconstruction. The overall schematic data acquisition procedures were shown in Fig. 3.3.3. We'll follow the sequence of data flow to explain the function of each instrument and the reason why we choose them. Since the repetition of pulsed laser is 80 MHz, it equivalently generates 80 MHz fluorescent pulses. In order to utilize the enormous amount of signal maximally, we plan to capture all of the pulses which means the recording rate should at least higher than the repetition rate of laser pulses to prevent from missing any fluorescent pulses. Through complete searching of commercial digitizers, we chose a four-channel digitizer (NI-5734, National Instrument) due to its 120-MS/s (sampling per second) bandwidth with 16-bit digital



resolution, which is high enough for sampling. Besides, it provides the capability of sampling for four channels simultaneously, so we only need 8-piece digitizers to accommodate 32 parallel signals, reducing the total cost. To match the sampling rate with 80-MHz signal pulses, we utilize 80-MHz synchronization signal exporting from the back panel of the laser as a clock signal and import it into the digitizer as a trigger. The shape of the synchronization signal is similar to sinusoidal wave. By setting the digitizer with the condition of sampling each point while the synchronization wave passing through zero from negative to positive, we are able to sample the fluorescent signal synchronized with laser pulses. However, here comes a problem that which timepoint is the best to sample the signal? The sampling timepoint might not match the peak of the fluorescent signal. To address the problem, we customized a laser delay board to arbitrarily tune the delay of the laser synchronization signal to match the peak of the fluorescent signal. As shown in Fig. 3.3.4, CH1 signal is the synchronization wave captured by an oscilloscope and CH2 signal is the fluorescent signal. Due to the intrinsic property of fluorescence, the occurrence of fluorescent pulse appears randomly within the duration of fluorescent lifetime (2-3 ns); therefore, the overlapping of multiple fluorescent pulses looks like a “wave packet” with 80-MHz repetition rate. We could thereby tune the delay of laser synchronization signal to match the peak of the wave packet to ensure that we acquire the maximal signal, as shown with red dot line in Fig. 3.3.4.

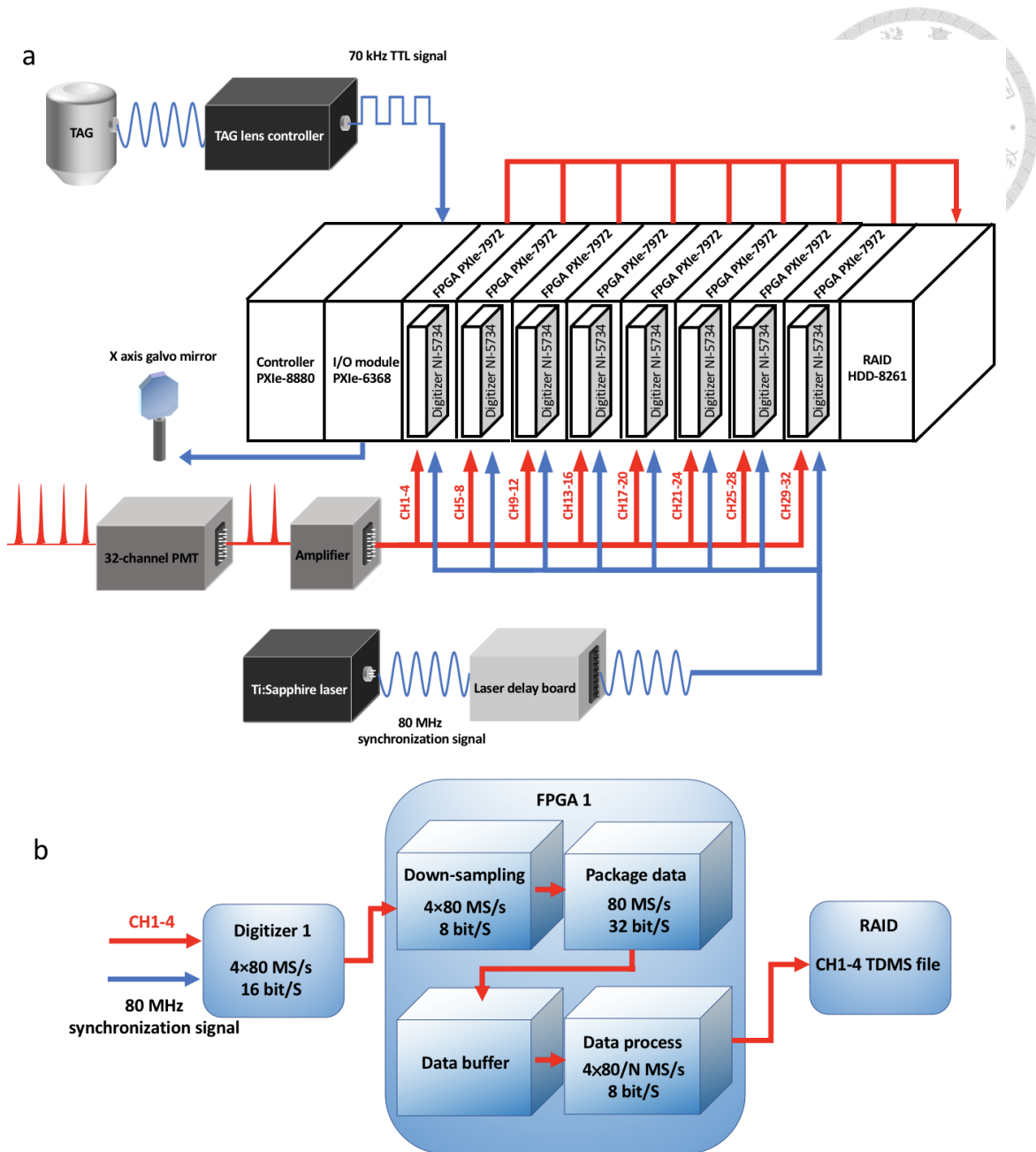


Fig. 3.3.3 Overall setup and data process procedure of our DAQ system

(a) The schematic of the data flow and each instrument. (b) The data flow showing how signal processes within digitizer and FPGA.

After 32 fluorescent signals were sampled by digitizers, the data were sent to the field-programmable gate array (FPGA, PXIe-7972, National Instrument) for data pre-processing. As shown in Fig. 3.3.3(b), signals undergo four different processes. First, each data was down-sampling from 16-bit to 8-bit to reduce the throughput of data

transmission to prevent from overload. Next, the data gathered from four different channels was cascaded to form a 32-bit dataset to reduce the amount of data transfer and then sent to the data buffer. After that, FPGAs provided the capability to pre-process the data, such as decimation, average and accumulation. For example, the data can be averaged per N points to generate a processed data. With those pre-process functions, we can manipulate the data before those datasets were sent to the hard-disk for storage. Finally, the packaged data was transformed into TDMS file and stored in the solid-state disk (SSD, HDD-8261, National Instrument). Owing to the fact that we sample each channel with 80-MHz sampling rate, totally it will generate $32 \times 80/N$ MHz = 2.56/N GHz data throughput which is quite enormous. To handle such large amount of data, we constructed an array of solid-state drives into a redundant array of independent disks (RAID) which provide not only 2.9 TB capacity for storage but also 2 GB/s data transmission rate. Several important parameters during data acquisition are listed in Table.

3.3.2.

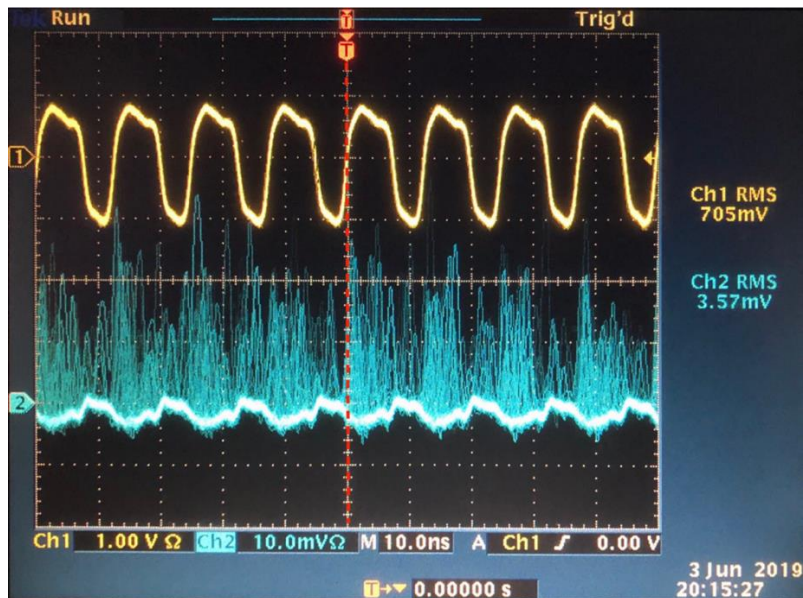


Fig. 3.3.4 Laser synchronization signal (CH1) and fluorescent pulse signal (CH2) captured by the oscilloscope

Red dot line indicates that the sampling timepoint matches the peak of fluorescent wave

packet.



After finishing data acquisition, another important issue is image reconstruction. In order to assign each signal to the correct position in the three-dimension coordinate, it is necessary to record the scanning position of imaging tools during data acquisition, such as the rotating angle of galvanometric mirror and TAG lens. Therefore, we use a multi-function I/O module (PXIe-6368, National Instrument) to receive the transistor-transistor logic (TTL) signal emitted from the TAG lens controller. The TTL signal synchronized with the operation frequency of the TAG lens driven by sinusoidal waves. By recognizing the rising edge of the TTL signal, we are able to know how many fluorescent pulses are included within each cycle of axial scanning. As shown in Fig. 3.3.5, the green line shows the TTL signal of the TAG lens and the blue dots indicate each sampling of data. During each cycle of TTL signal, the data within the cycle was packaged and then assigned to correct position while doing imaging reconstruction.

Parameters	Value
Laser repetition rate	80 MHz
Sampling rate of each digitizer	80 MS/s
Total Sampling rate of digitizers	2.56 GS/s
Digital resolution	8 bits
Total data throughput	2.56/N GB/s

Table. 3.3.2 Several parameters related to the data acquisition and throughput.

One thing needs to be noticed is that although TTL signals synchronized with sinusoidal driven waves, we actually don't know the phase shift between them. It will lead to the image shift if we arbitrarily assign data into the wrong position. Either

measuring the phase shift between two signals or using post-image reconstruction can solve this problem.

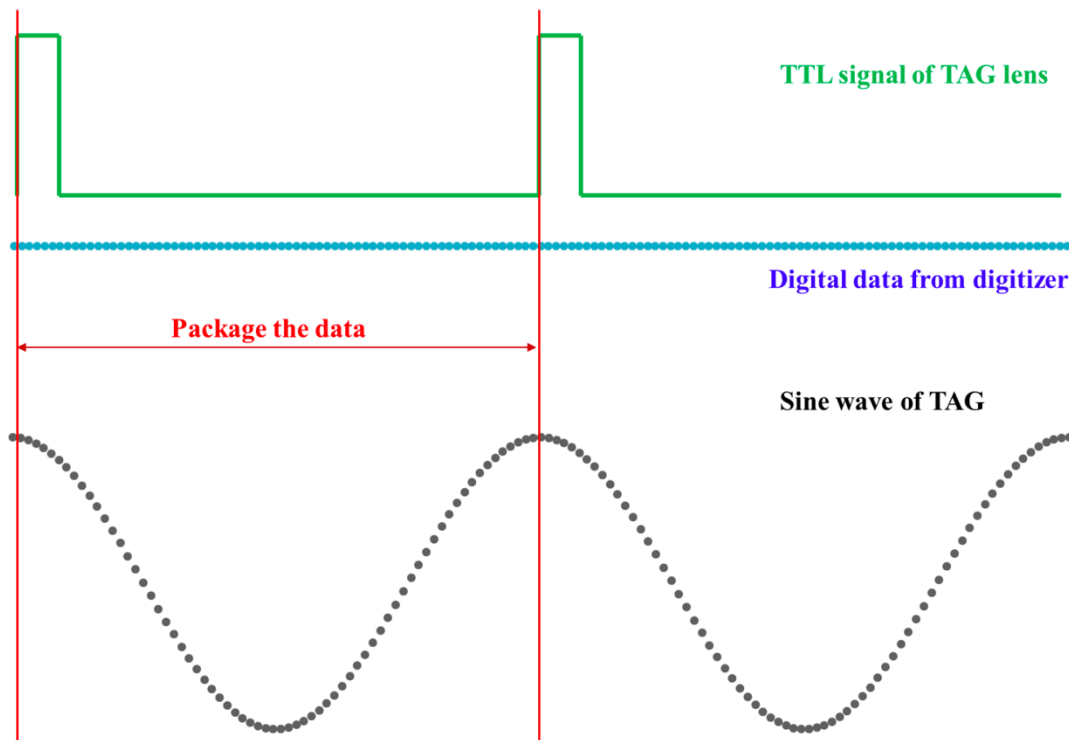



Fig. 3.3.5 Image reconstruction procedure

Finally, those abovementioned instruments were integrated into a chassis (PXIe-1075, National Instrument) and manipulated by a main controller (PXIe-8880, National Instrument). Main control software was written by SouthPort Co., Ltd. All instruments were listed in Table. 3.3.3.

Instrument		Company	Model number
Amplifier board		SouthPort Co., Ltd	Customized, ERA- 3SM+
DAQ system	Chassis	National Instrument	PXIe-1075
	Controller	National	PXIe-8880



		Instrument	
	Digitizer adapter module	National Instrument	NI-5734
	FPGA module	National Instrument	PXIe-7972
	Multifunction I/O module	National Instrument	PXIe-6368
	Data storage module	National Instrument	HDD-8261
	Laser trigger delay board	SouthPort Co., Ltd	Customized

Table. 3.3.3 List of every instrument used in DAQ system with the information of company and model number.

3.4 Expected performance

In order to confirm that our system can satisfy the requirements and be feasible to apply on functional studies of *Drosophila* brain. Several aspects and expected system performances, such as the spatial resolution, the size of volume and the volumetric imaging speed, are necessary to be clarified in advance to assure the viability before conducting the experiments.

3.4.1 Spatial resolution

First of all, in order to verify the intrinsic subcellular resolution provided by two-photon microscopy, the theoretical lateral full width at half maximum (FWHM) can be formulated as [25],

$$FWHM_{xy} = \begin{cases} \sqrt{2\ln 2} \times \frac{0.32\lambda}{NA} & NA \leq 0.7. \\ \sqrt{2\ln 2} \times \frac{0.325\lambda}{NA^{0.91}} & NA > 0.7. \end{cases} \quad (3.13)$$



Although the numerical aperture of the objective lens we used is 0.75, we actually didn't utilize full aperture of the objective lens, since the aperture of the TAG lens needed to be taken into consideration. The beam size of incident beam should not exceed the effective aperture of the TAG lens which was supposed to be 11 mm; otherwise, it might not operate as what it was expected to be. Thus, in our system, the beam size had been adjusted to 10 mm. Although it is not optimal, it is still close to the optimal value. Thus, the effective numerical aperture of objective lens needed to be modified to 0.572. After inserting all parameters into the equation, we could get

$$FWHM_{xy} = \sqrt{2\ln 2} \times \frac{0.32\lambda}{NA} = \sqrt{2\ln 2} \times \frac{0.32 \times 940}{0.572} = 619 \text{ nm}. \quad (3.14)$$

And the axial FWHM could also be provided as follows,

$$FWHM_z = \frac{\sqrt{2\ln 2} \times 0.532\lambda}{n - \sqrt{n^2 - NA^2}} = \frac{\sqrt{2\ln 2} \times 0.532 \times 940}{1.33 - \sqrt{1.33^2 - 0.572^2}} = 4.57 \text{ } \mu\text{m}. \quad (3.15)$$

Those results showed that both FWHM in lateral and axial direction were adequate to resolve *Drosophila* brain neurons.

3.4.2 Volumetric imaging: Size

In order to know how large the volume can be achieved, we decomposed the volume

into three orthogonal dimensions which are scanned by three different tools, a DOE, a TAG lens and a single-axis galvanometric mirror respectively. Since these tools are individually controlled, we can estimate the theoretical extension or scanning range separately. Besides, to form a digital image, number of pixels is also one important factor to be considered. We'll follow the sequence of scanning order to calculate each parameter, starting from a DOE, a TAG lens and then to a galvanometric mirror. The schematic of the volume with corresponding scanning tools for three different dimensions was showed in Fig. 3.4.1.

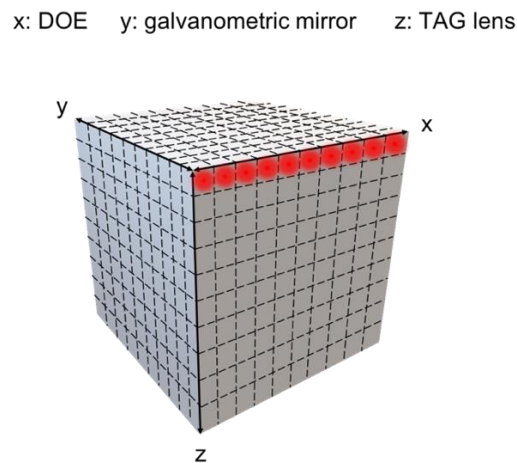


Fig. 3.4.1 Schematic of a volume with given dimensions for each scanning tool

DOE (x direction):

From the discussion in subsection 3.3.1, we already know that with 6.875-degree splitting angle of the DOE and other relayed lenses, the 32 foci forms on the imaging plane of objective lens with 200 μm length. Without scanning in x direction, there are 32 pixels in x direction corresponding to each beam.

TAG lens (z direction):

The axial extension range of the TAG lens depends on how large is the optical focusing power. The maximal optical focusing power of the TAG lens is ± 1 diopter (1/m),

as shown in Fig. 3.4.2 [63]. From the equation of axial extension calculation showed in section 2.3, the maximum extension range is roughly inversely proportional to the square of objective magnification. Here we used a 20x objective lens, leading to ~200 μm depth coverage.

$$\Delta z = \frac{2f_{tube}^2 \delta_{TAG}}{M^2 - \delta_{TAG}^2 (Md - f_{tube})^2} = \frac{2\delta_{TAG}}{\delta_{obj.}^2 - \delta_{TAG}^2 (\delta_{obj.} d - 1)^2} \quad (3.16)$$

$$= \frac{2}{100^2 - (100 \times 0.005 - 1)^2} = 0.0002 \text{ m} = 200 \text{ } \mu\text{m}.$$

Frequency (kHz)	Calc. Eff. Aperture (mm)	Total Optical Power (diopters)	% of Max Driving Amplitude
68.5	11.0	0.5	20%
68.5	11.0	1.0	39%
68.5	11.0	1.5	58%
68.5	11.0	2.0	75%
188.0	4.0	10.0	43%
188.0	4.0	20.0	80%
308.0	2.5	10.0	5%
308.0	2.5	20.0	10%

Fig. 3.4.2 Specification of TAG lens 2.5β , including operation frequency, effective aperture, optical power and corresponding driving amplitude

The calculation of the pixel number in the z direction needs to combine with the repetition rate of the pulsed laser. Since we collect one signal for each pulse by a digitizer, with 80-MHz laser repetition rate, we can acquire 8×10^7 sampling point accordingly. The operation frequency of the TAG lens is 70 kHz which means, dividing 80 MHz by 70 kHz, there are about 1143 layers in the z direction. Because the TAG lens scans back and forth during each round, there are actually 571 different layers due to the duplication of each layer. Although there are plenty of layers generated, the lack of high enough axial resolution impedes the applicability of these layers. The digital axial resolution can reach 0.35 μm per pixel, but the optical axial resolution is only 4.57 μm . Thus, in order to

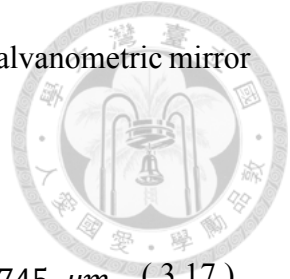
exploit redundant layers, we accumulate every 8 signals into one signal in the FPGA to enhance the SNR, reducing the digital axial resolution to 2.8 μm per pixel. The digital axial resolution was roughly half of the optical axial resolution which nicely matched the Nyquist-Shannon sampling theorem. The number of layers after averaging by FPGA becomes 71 which means there are 71 pixels in z direction. Those related parameters were listed in Table. 3.4.1.

Parameters	Values
Repetition rate of pulsed laser	80 MHz
Operation frequency of the TAG lens	70 kHz
Number of layers generated	$\frac{80 \text{ MHz}}{70 \text{ kHz}} = 1143 \text{ layers}$
Number of effective layers	$\frac{1143 \text{ layers}}{2} = 571 \text{ layers}$
Axial extension range	200 μm
Digital axial resolution	$\frac{200 \mu\text{m}}{571 \text{ layers}} = 0.35 \mu\text{m}$
Optical axial resolution	4.57 μm
Number of effective layers after averaging by FPGA	$\frac{571 \text{ layers}}{8} = 71 \text{ layers}$
Updated digital axial resolution	$\frac{200 \mu\text{m}}{71 \text{ layers}} = 2.8 \mu\text{m}$

Table. 3.4.1 Several parameters related to the calculation of pixel number in axial direction.

Galvanometric mirror (y direction):

The galvanometric mirror is driven by electrical input signals and the maximal input voltage is $\pm 10 \text{ V}$. From the manual of galvanometric mirrors, 10 V input signal indicates



to 20-degree angle of rotation. Thus, the maximal scanning range by galvanometric mirror on the imaging plane of objective lens can be deduced as well.

$$\text{Scanning range} = f \times \theta_1 \times m_2 = 10 \text{ mm} \times 40 \times \frac{\pi}{180} \times \frac{50}{200} = 1745 \text{ } \mu\text{m} \quad (3.17)$$

f , focal length of objective lens; θ_1 , maximal radius of rotation angle by galvanometric mirror; m_2 , magnification factor of scan lens and tube lens.

Since the galvanometric mirror needs to wait the TAG lens to finish one cycle of the z scanning and then rotates to the adjacent pixel, the total number of pixels in y direction depends on how many cycles the TAG lens undergoes. There is no specific upper limit, but in our system, 1024 pixels is the maximal number of pixels in y direction. The organization of maximal scanning range and total number of pixels in three dimensions are shown in Table. 3.4.2.

	Theoretical scanning range	Pixel number
x (DOE)	200 μm	32 pixels
y (galvanometric mirror)	1745 μm	1024 pixels
z (TAG lens)	200 μm	71 pixels

Table. 3.4.2 Organization of maximal scanning range and total pixel number.

3.4.3 Volumetric imaging: Speed

After evaluating the imaging size, another important issue in this study is volume rate. To calculate the imaging speed, we know that the DOE already forms 32 foci in the x direction for “simultaneously” scanning, so we only need to consider the scanning period of the TAG lens and a galvanometric mirror. The TAG lens operates at ~ 70 kHz

which represents that $\sim 14 \mu\text{s}$ is taken to complete each cycle of axial scanning. By steering the galvanometric mirror for raster scanning, volumetric imaging can be achieved and the time duration depends on how many rounds does the TAG lens operate. In our control software, viable choices are 128, 256, 512, 1024 pixels. Please note that these values can be arbitrarily adjusted to fit our need as long as the rotation frequency of galvanometric mirror is below the limitation of inertia. With the information of the pixel number, the volume rate can be thereby calculated and showed in Table. 3.4.3. The theoretical maximal volume rate can reach 558 Hz.

	Number of pixels scanned by galvanometric mirror (y direction)			
	128	256	512	1024
Total pixel	$32 \times 128 \times 71$	$32 \times 256 \times 71$	$32 \times 512 \times 71$	$32 \times 1024 \times 71$
Total period (μs)	$14 \times 128 = 1790$	$14 \times 256 = 3580$	$14 \times 512 = 7170$	$14 \times 1024 = 14340$
Volume rate	558 Hz	279 Hz	140 Hz	70 Hz

Table. 3.4.3 Estimation of volume rate with different number of pixels in y direction.

Chapter 4. Experimental protocols and sample preparations



In this chapter, we demonstrate experimental protocols and sample preparations details.

4.1 Experimental protocols

1. System alignment: Excitation light path

- i. Turn on the Ti:Sapphire laser and tune the wavelength to 940 nm.
- ii. Put on the removable mirror with specific angle to guide the laser beam into our home-built system.
- iii. Turn on the laser shutter and use the IR card to check the direction of the laser beam to make sure the laser beam enters our system.
- iv. At the beginning of our system, we place one half-wave plate and PBS crystal to adjust the power, and a mirror pair and irises are used to adjust the direction of the laser beam to normally pass through the center of two optical elements. Adjust the degree of the half-wave plate into 79 degree which provides the least transmission power.
- v. Turn on the power supply of galvanometric mirrors and open “JadeMAT0.1” software on the computer, as shown in Fig 4.1.1. The software is used for 2D image scanning. Click the concentric pattern at the lower left corner of the control panel to calibrate the voltage of galvanometric mirrors controller into zero.
- vi. Another set of mirror pair and irises after the half-wave plate and PBS crystal are used for the same purpose to align the light path of remaining optical

elements, including the beam shrinker, the 4f system, galvanometric mirrors, the scan lens and the tube lens.

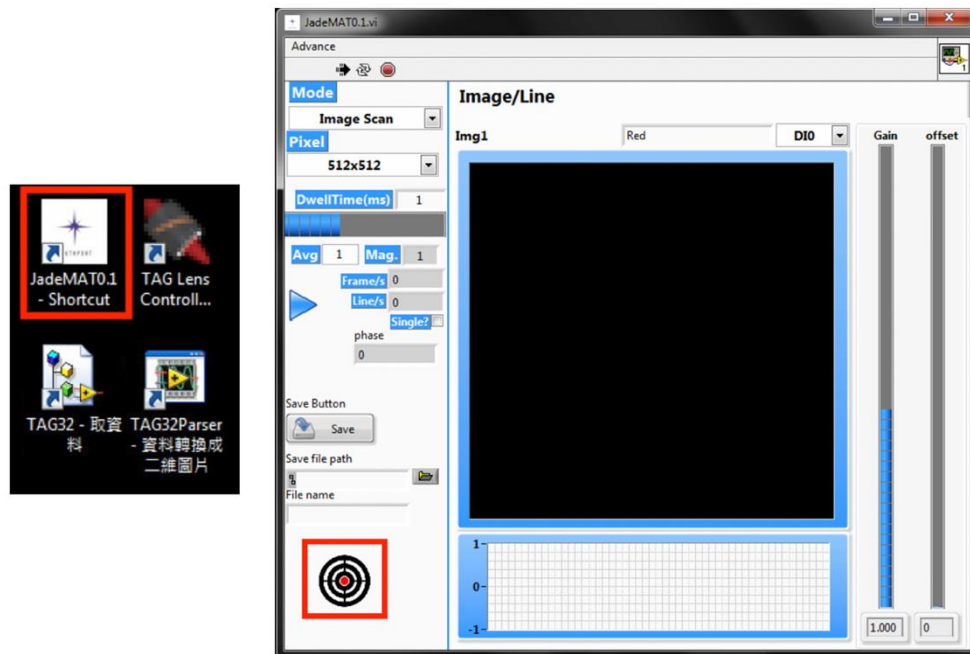


Fig. 4.1.1 Control panel of 2D imaging software

- vii. After aligning all of the aforementioned elements, put on the silver mirrors and screw the hollow tube into the objective lens mount. There are two irises mounted inside the tube, and then the silver mirror pair and irises can be used to align the light path of objective lens.
 - viii. Remove the hollow tube and screw objective lens into the lens mount.
 - ix. Now, we finish aligning excitation light path.
2. System alignment: Emission/detection light path
- i. Fill a glass container with 1 mM FITC fluorescent solution and put it onto the 3-axis specimen stage beneath the objective lens.
 - ii. Adjust the half-wave plate into 70 degree which provides 40 mW transmission



laser power after the objective lens to excite the fluorescent solution.

- iii. Turn off the fluorescent tubes and insert the dichroic mirror (DMLP650R) between galvanometric mirrors and 4f system to separate the excitation laser and emission fluorescent signals.
- iv. Two mirrors and irises after the dichroic mirror are used to align the detection light path. Check the second iris in front of the 32-channel PMT to make sure fluorescent signals locates at the center of detector.
- v. Turn on the 32-channel PMT. Connect output cable of CH16 and CH17 from the PMT to oscilloscope. Check the average amplitude of signals from both channels. If it is different, adjust the mirror before the detector to make it balance.
- vi. Insert the grating which is mounted on a flipper.
- vii. Now, we finish aligning emission/detection light path.

3. Data acquisition

- i. Check the laser delay board, as shown in Fig 4.1.2, which is used for laser signal synchronization. Fine phase tuner should be (0, 1, 0, 1). Coarse phase tuner should be (0, 0, 1, 0) in the left-hand side and (0, 0, 0, 0) in the right-hand side.

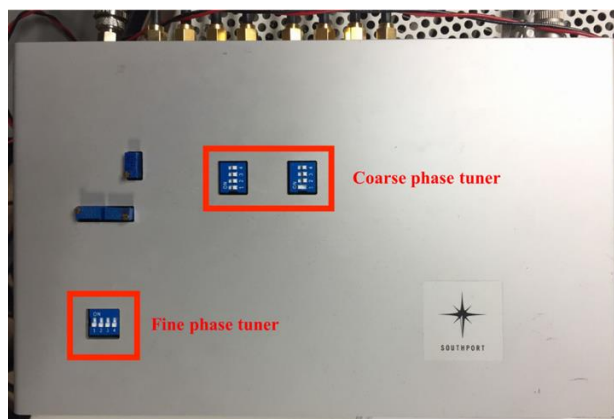


Fig. 4.1.2 Appearance of laser delay board



- ii. Turn on the power supply of the TAG lens controller (Drvkit3) and connect the controller with the computer via the USB cable. Also, connect the controller with the TAG lens via a SMA connector.
- iii. Open “TAG Lens Controller 3.3.8” software on the computer, as shown in Fig 4.1.3. Follow below steps in the figure to activate the TAG lens.

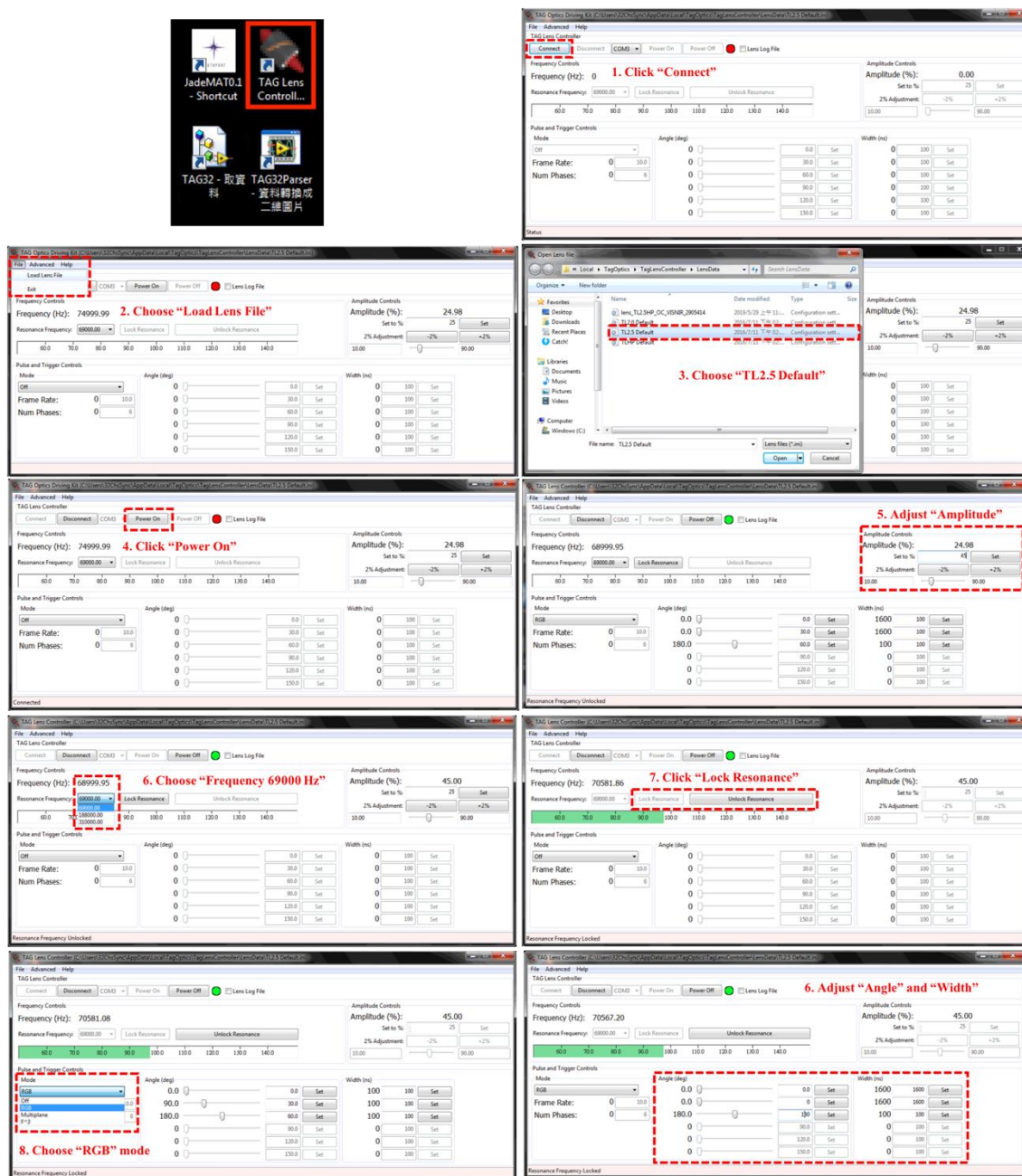
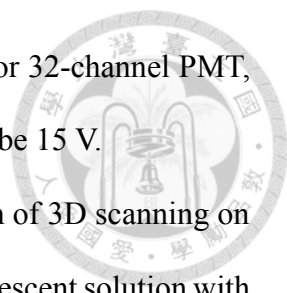


Fig. 4.1.3 Control panel of the TAG lens and operation steps

- 
- iv. Turn on the power supply. Check that the voltage supply for 32-channel PMT, the delay board, the TAG board and the wire board should be 15 V.
 - v. Open “TAG32” software which is used for data acquisition of 3D scanning on the computer, as shown in Fig 4.1.4. Replace the FITC fluorescent solution with fluorescent microspheres slide or *Drosophila* brain slide. Follow the steps listed in Fig 4.1.4 to accomplish data acquisition of the experiment.
 - vi. Now, we finish data acquisition.

4. Image reconstruction

- i. After data acquisition, it will generate several TDMS files.
- ii. Open “TAG32Parser” software which is used for image reconstruction, as shown in Fig 4.1.5. It will help us reconstruct 2D images from different layers. Follow the steps in Fig 4.1.5 and choose the TDMS files generated in the previous step to complete the image reconstruction.
- iii. Those files could be further exported out for imaging analysis.
- iv. Now, we finish image reconstruction.

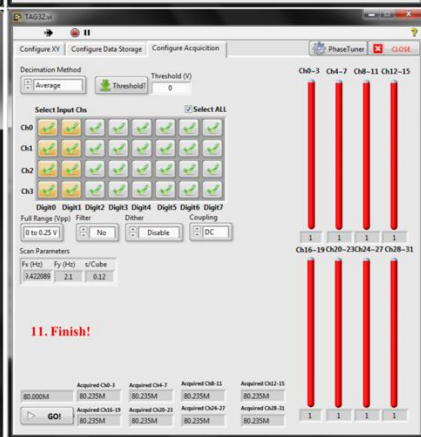
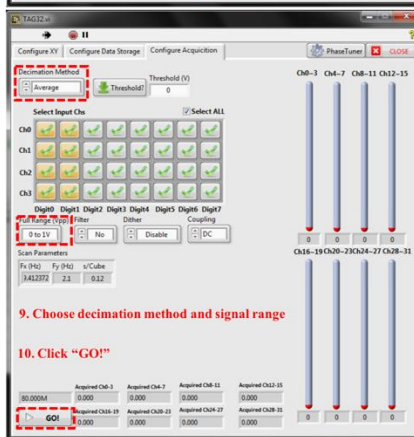
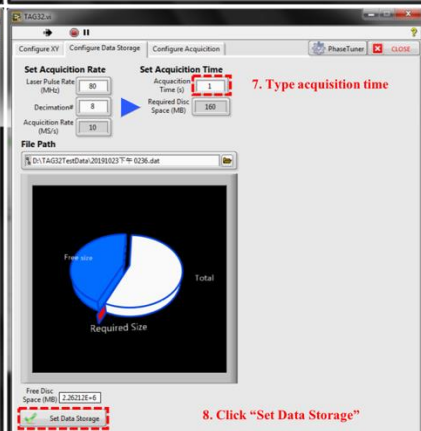
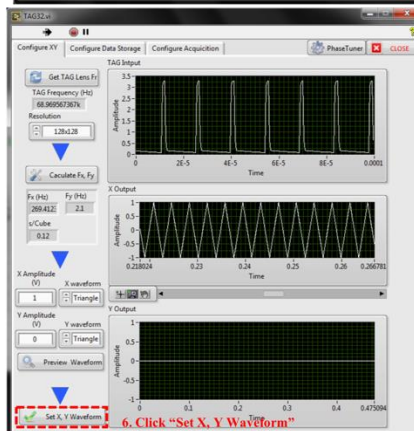
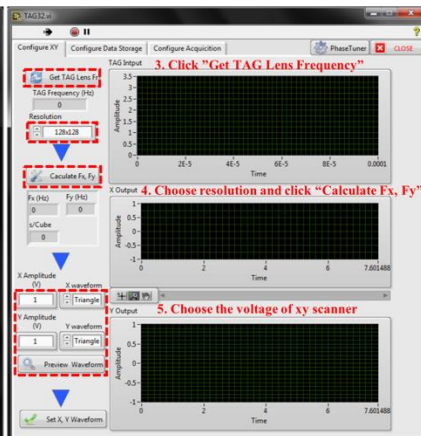
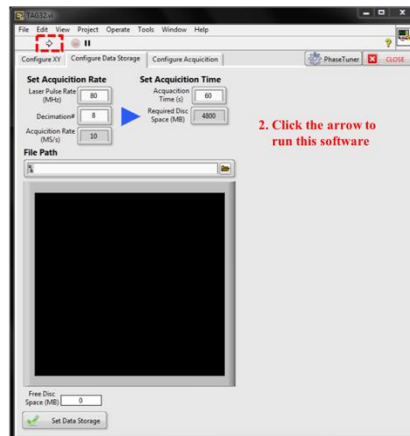
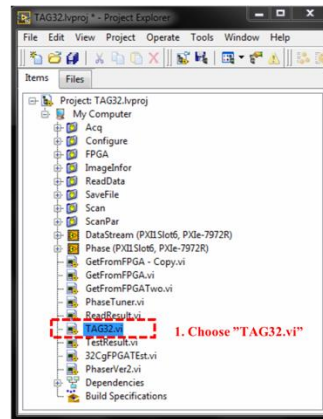


Fig. 4.1.4 Control panel of data acquisition software and operation steps

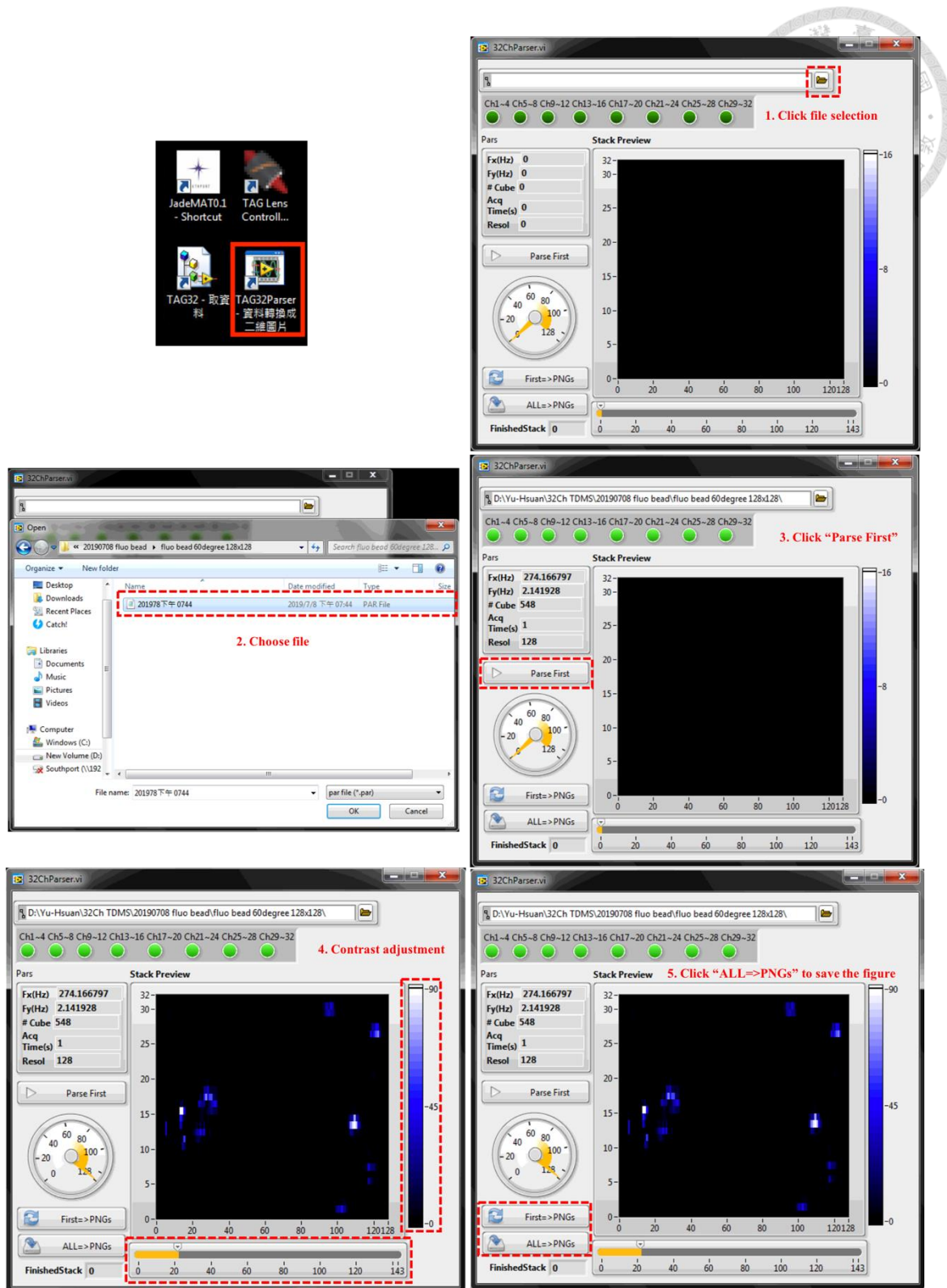
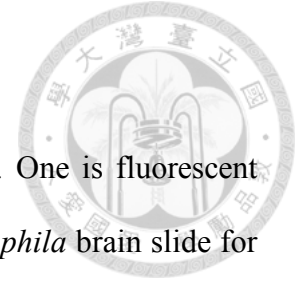


Fig. 4.1.5 Control panel of image reconstruction software and operation steps

4.2 Sample preparations

In this study, we use two kinds of sample for demonstration. One is fluorescent microspheres for system performance testing and the other is *Drosophila* brain slide for preliminarily biological testing.



4.2.1 Test sample: Fluorescent microspheres

1. 2D fluorescent microspheres slide
 - i. Take a slide and use de-ionized water (DI water) to wash dust away.
 - ii. Use 10 μL pipette to draw 3-5 μL fluorescent microspheres on the upper surface of the slide. In this study, we use three types of fluorescent microspheres as the test sample. The first two are 200 nm and 500 nm diameter yellow-green (excitation/emission, 505/515) fluorescent microspheres (F8774 and F8813, Thermo Fisher Scientific Inc.) for spatial resolution verification. The concentration of 200 nm and 500 nm fluorescent microspheres needs to be diluted with DI water into 10^5 and 10^4 times, respectively, to avoid the aggregation of microspheres. The other one is 10 μm diameter yellow-green (excitation/emission, 505/515) fluorescent microspheres (F8836, Thermo Fisher Scientific Inc.) which is used for simulating *Drosophila* brain neurons. Since the concentration of 10 μm fluorescent microspheres is low enough, it thereby doesn't need to be diluted.
 - iii. Use a cover glass to lay over fluorescent microspheres, and seal the edges of cover glass with nail polish.
2. 3D fluorescent microspheres embedded in agarose gel
 - i. Take a petri dish and use DI water to wash dust away.
 - ii. Use 1000 μL pipette to draw 22000 μL DI water into beaker. Add 0.08 g

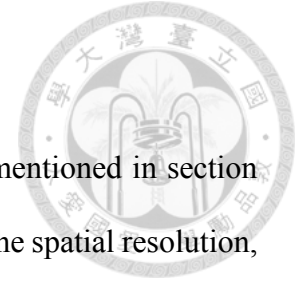
agarose into the beaker to make a 0.4% agarose gel.

- iii. Use microwave oven to heat it up for 1 min to dissolve agarose into water.
- iv. Wait for it to cool down. Before the temperature is below 40 degrees Celsius, use a 1000 μL pipette to draw 3000 μL agarose gel solution into the petri dish and mix with 300 μL 10 μm fluorescent microspheres to make a 9% agarose gel with fluorescent microspheres embedded in.

4.2.2 In vitro fixed *Drosophila* brain slide

- i. Put the tube with *Drosophila* inside into iced water to anesthetize them.
- ii. Fix *Drosophila* onto an iron platform with AB glue.
- iii. Use tweezers to remove the cuticle above *Drosophila*.
- iv. Take a slide and put on two donut-shape stickers overlapping with each other.
- v. Drop *FocusClear* solution in the middle of stickers.
- vi. Take out the *Drosophila* brain by the tweezer and put it into the cavity which locates in the middle of stickers.
- vii. Use a cover glass to lay over the *Drosophila* brain and seal the edges of the cover glass with nail polish.

Chapter 5. Results



In this chapter, several expected performances of our system mentioned in section 3.4 will be tested and clearly demonstrated in section 5.1, including the spatial resolution, the size of volumetric imaging and the volume rate. Detailed comparison between the expected performances and experimental results will be described, as well as the reasons of discrepancy. Besides, we also test the *Drosophila* brain slide labeled with GCaMP7f on mushroom body which will be shown in section 5.2.

5.1 System performance

5.1.1 Spatial resolution

From the mathematical calculation shown in subsection 3.4.1, the theoretical FWHM in lateral and axial direction are 619 nm and 4.57 μm , respectively. In order to examine the spatial resolution, we used 200 nm and 500 nm fluorescent microspheres which are much smaller than theoretical resolution for the lateral and axial testing, respectively. Since the sample will undergo raster scanning which gathers information pixel by pixel, the excitation PSF of the microsphere image is actually constructed by the convolution of the laser focal spot with the microsphere. Therefore, by convolving the theoretical FWHM with the size of microsphere using MATLAB, the convolution results of the lateral and axial direction are modified to be 629 nm and 4.573 μm . For experimental simplicity, instead of using the 32-channel PMT as the detector, the image is formed by scanning the fluorescent microspheres with original single-beam two-photon microscopy (without inserting the DOE) and captured by a single-channel PMT (H5782-20, Hamamatsu).

The experimental results are shown in Fig. 5.1.1. In Fig. 5.1.1(a), the scanning image of 200 nm fluorescent microsphere and the intensity profile along the center were provided which could deduce the experimental FWHM in the lateral direction. The axial FWHM could also be measured, as shown in Fig. 5.1.1(b).

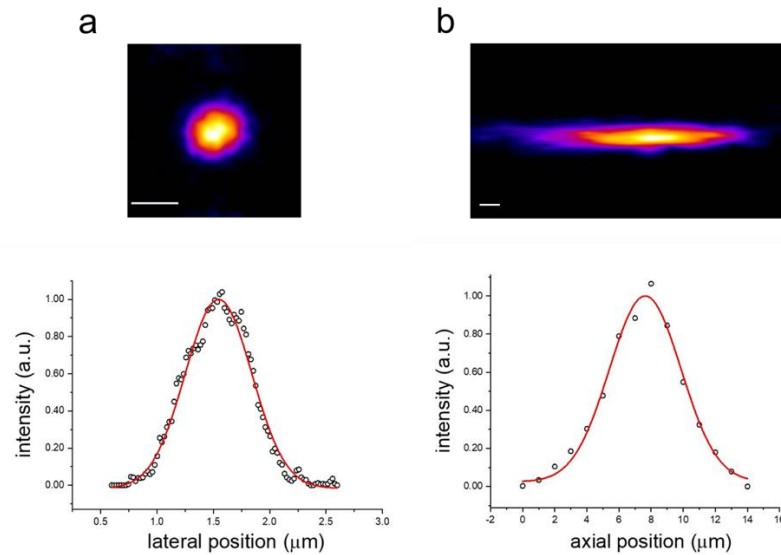


Fig. 5.1.1 Spatial and axial resolution verification

(a) (Top) Scanning imaging of 200 nm fluorescent microsphere in x-y plane. (Bottom) Intensity profile and fitting result. (b) (Top) Scanning imaging of 500 nm fluorescent microsphere in the x-z plane. (Bottom) Intensity profile and fitting result. The scale bar is 1 μm .

By taking several results of different microspheres for average, we could acquire the average value and standard deviation of FWHM in the lateral and axial direction, as shown in Table. 5.1.1. The theoretical values and deviation between them are also provided.

	Lateral resolution	Axial resolution
Theoretical results	629 nm	4.573 μm
Experimental results	693 \pm 6 nm	5.46 \pm 0.18 μm
deviation	10.2%	19.6%

Table. 5.1.1 Comparison of lateral and axial resolution between theoretical and experimental results.

There is about 10.2 % deviation in lateral resolution and 19.6 % in axial resolution which might be due to the intrinsic system aberration. Despite the deviation from the theoretical resolution, the spatial resolution had been proved to be adequate for distinguishing soma of neuron ($6\ \mu\text{m}$) in a living brain of *Drosophila*.

5.1.2 Volumetric imaging: Size

To visualize the scanning pattern, from fast to slow axes, we moved a homemade thin green-fluorescent film (thickness $\sim 4\ \mu\text{m}$) axially across the scanning volume and used a sCMOS camera (Neo 5.5, ANDOR) for detection, as shown in Fig. 5.1.2.

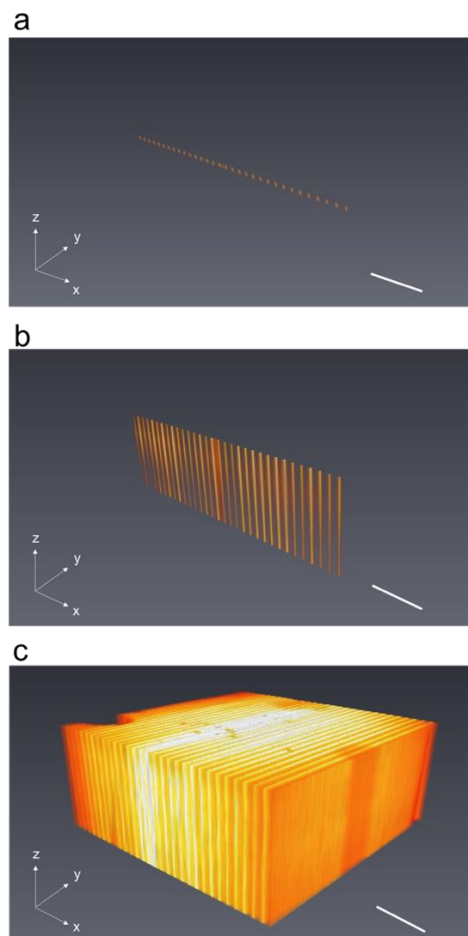


Fig. 5.1.2 3D reconstruction imaging of scanning pattern in sequence using a thin green-

fluorescent film

(a) Image of 32 foci. (b) Image of 32 scanning lines with the TAG lens turned on. (c) Volumetric image which is constructed by 32 planes, scanning with both the TAG lens and the galvanometric mirror turned on. The scale bar is 50 μm .

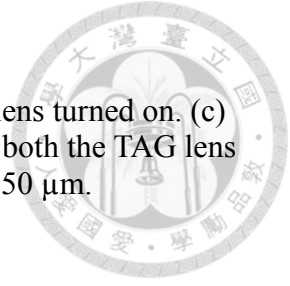


Fig. 5.1.2(a) shows the image of 32 foci formed by the DOE, without turning on the TAG lens and the galvanometric mirror. This can be regarded as scanning “simultaneously” with 32 foci in x direction. The performance of 32 foci and intensity profile along 32 foci are provided in Fig. 5.1.3. Total spacing of 32 foci is $\sim 207 \mu\text{m}$, close to the theoretical value which is $200 \mu\text{m}$. The nonuniformity of the 32 foci was probably caused by the spherical aberration for those beams far from the optical axis. There is one small peak located at the middle of 32 foci which might be due to zero-order splitting of the incident beam.

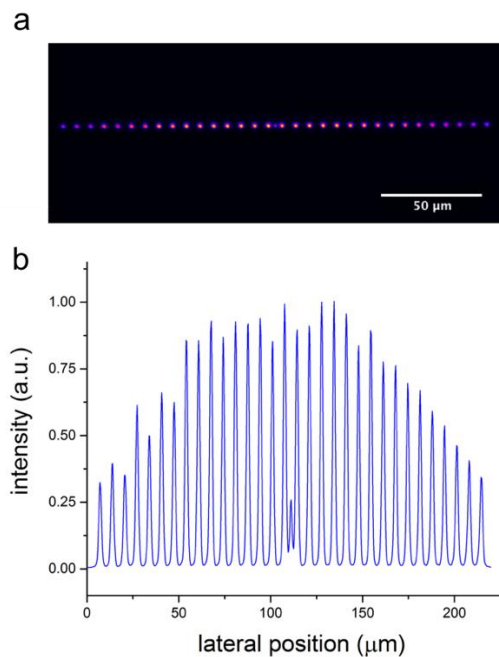


Fig. 5.1.3 Image of 32 foci

(a) Wide-field image of 32 foci captured by the sCMOS camera. (b) Intensity profile along 32 foci. The scale bar is 50 μm .

After turning on the TAG lens, Fig. 5.1.2(b) presents the second fast scan along the z axis, where foci scan up and down at ~ 70 kHz, resonant frequency of the TAG lens, resulting in a thin layer of 32 axially scanning lines. By plotting the intensity profile across the axial direction, as shown in Fig. 5.1.4, we can measure the extension of TAG lens. In this case, we use 1 μm green fluorescent beads to verify the extension. The experimental extension of the TAG lens, defined by the distance between two peaks, is about 320 μm with optical power of the TAG lens ranges between $\pm 1 \text{ m}^{-1}$. However, the theoretical extension with $\pm 1 \text{ m}^{-1}$ optical power is 200 μm . It seems that the experimental result is larger than theoretical result with 60% discrepancy. Possible reasons might be nonuniform coverage of the TAG lens aperture by incident beam mentioned in section 2.3, mismatch of the axis between the incident beam and the TAG lens or the optical power of TAG lens shifts as time goes by. Since the TAG lens was driven with sinusoidal signals which caused nonuniform sampling along the z axis, interpolation was required to register each plane into correct axial position.

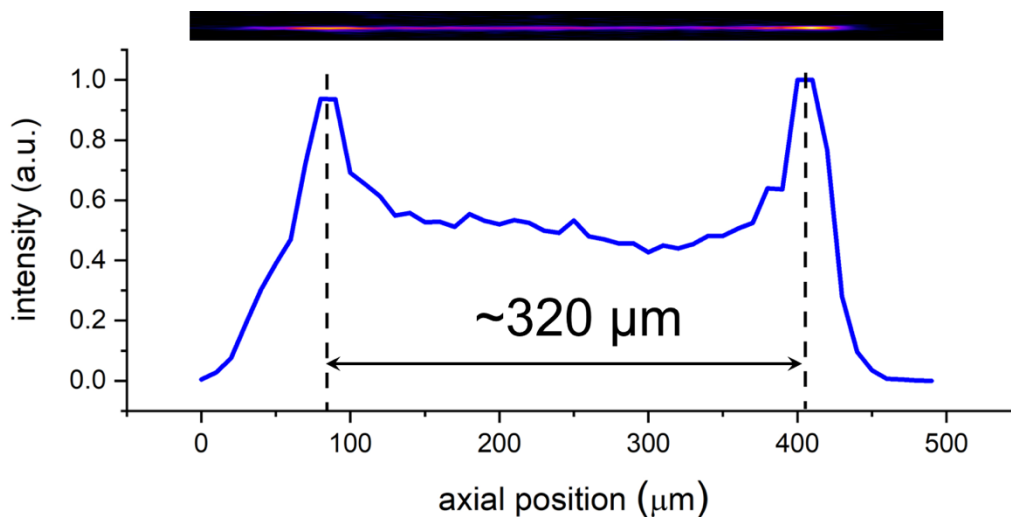


Fig. 5.1.4 Experimental axial extension of the TAG lens
The experimental axial extension of TAG lens is 320 μm .

After turning on both the TAG lens and the galvanometric mirror, Fig. 5.1.2(c) shows that the volume is filled with 32 vertical light ribbons, i.e. an image frame in the y-z plane. Based on the speed of galvanometric mirrors, a ribbon scan takes only a few millisecond [64]. After arranging 32-ribbon images in order (x direction), a 3D volumetric image could be acquired. Few nonuniform regions may be caused by manufacture defects of the fluorescent film. It is noteworthy that, with the aid of a pair of galvanometric mirrors, each ribbon shape of 32 beams can be arbitrarily located in the x-y plane, thus the parallelized scanning configuration allows observation on a volume with a curved shape which provides the versatility for the irregular structure. To verify the lateral scanning range of the galvanometric mirror, we measure the distance of scanning beam with a galvanometric mirror operating at 1 V, 3 V and 5 V, as shown in Fig. 5.1.5. The experimental extensions are 88.7 μm , 267.4 μm and 444.6 μm , respectively, which are close to theoretical estimations (87.2 μm , 261.9 μm and 436.6 μm). By adjusting the control voltage of the galvanometric mirror and the input amplitude of the TAG lens, scanning range can be arbitrarily changed to fit the sample.

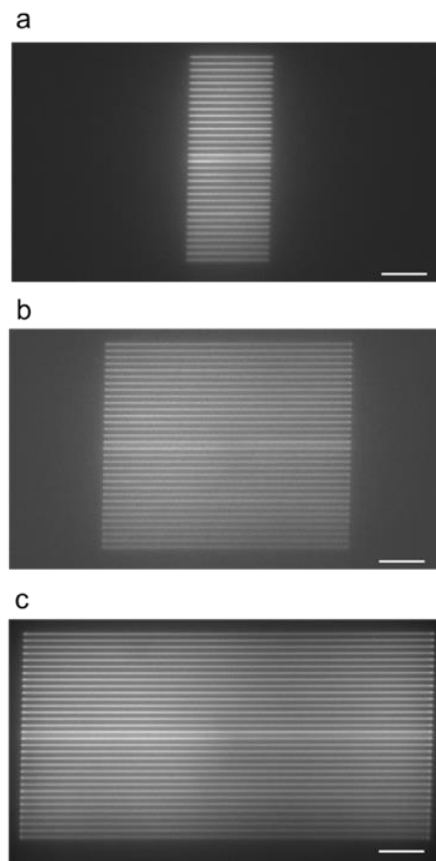


Fig. 5.1.5 Lateral scanning range of the galvanometric mirror
The galvanometric mirror is operating at (a) 1 V, (b) 3 V and (c) 5 V. The scale bar is 50 μm .

To prove the viability of our system, we constructed two homemade samples. One is 2D thin slide with 10 μm fluorescent microspheres. The other is 3D structure made by 10 μm fluorescent microspheres embedded in 0.4% agarose gel to simulate the soma of neurons distributed three-dimensionally in *Drosophila* brain.

2D slide of fluorescent microspheres:

In this demonstration, we scanned the sample with our 32-channel system, as shown in Fig. 5.1.6(a) with 32×128 pixels corresponding to $207 \times 262 \mu\text{m}^2$ imaging range. We also used single beam to scan the sample slowly and captured by a sCMOS camera, as

shown in Fig. 5.1.6(b) with 720×830 pixels corresponding to $234 \times 270 \mu\text{m}^2$. Although the number of pixels, so called digital resolution, of 32-channel system is not as high as camera, we still prove that all microspheres are captured without missing.

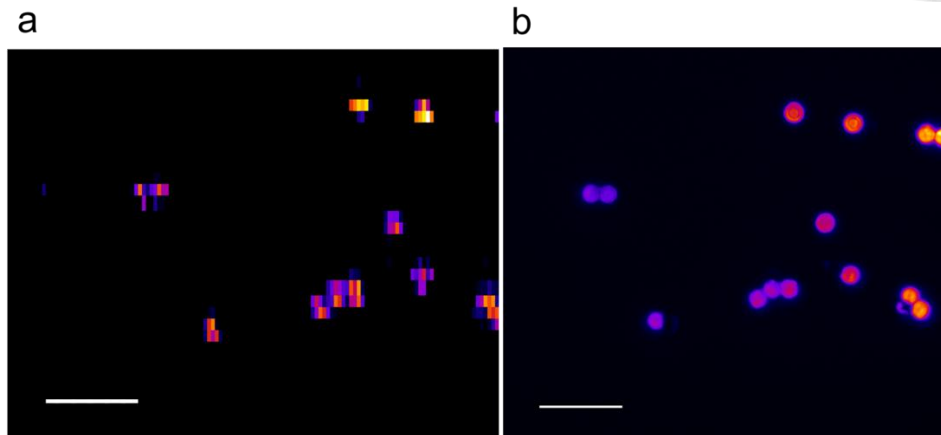
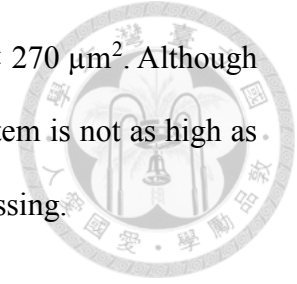


Fig. 5.1.6 Comparison of 2D fluorescent microspheres images

(a) Fast 32-beam scanning image captured by the 32-channel PMT (b) Single beam scanning image captured by the sCMOS camera. Horizontal axis is galvanometric mirror (y) and the vertical axis is DOE (x). The scale bar is $50 \mu\text{m}$.

3D structure of fluorescent microspheres:

The other representative result of ultrahigh speed volumetric imaging of $10 \mu\text{m}$ fluorescent microspheres embedded in 3D structure is given in Fig. 5.1.7(a), whose volume size is $207 \times 217 \times 185 \mu\text{m}^3$ corresponding to $32 \times 128 \times 70$ voxels and was acquired within 1.84 ms. The location of each microsphere was also verified through a slow-scanning version in Fig. 5.1.7(b), whose volume size is $262 \times 217 \times 170 \mu\text{m}^3$ corresponding to $512 \times 512 \times 17$ voxels which was based on single beam raster scanning in 3D (no DOE and the TAG lens turned off). Since we didn't equip with the automatic axial scanning tool, it took a few minutes to manually adjust z-stage to obtain one volume. The much faster imaging acquisition in Fig. 5.1.7(a) is based on trade-off of lower lateral sampling density (32×128 in Fig. 5.1.7(a) versus 512×512 in Fig. 5.1.7(b)) and reduced

signal-to-noise ratio. Nevertheless, the location of each microsphere was again precisely mapped, manifesting the potential of this high-speed imaging system toward studying dynamics in somas of a neuronal system. Different viewpoints of volumetric imaging by fast scanning and slow scanning were also showed in Fig. 5.1.7(c)(d) from the x-z plane and (e)(f) from the x-y plane.

The brief comparison between the theoretical imaging size and the experimental imaging size was provided in Table. 5.1.2. The extension range of the DOE was almost the same. Due to the fact that this is just the preliminary examination, the galvanometric mirror and the TAG lens were not operated with maximal amplitude. However, the demonstration indeed showed the capability of volumetric imaging for three-dimensional structure.

	Theoretical maximal range	Experimental range
x (DOE)	200 μm	207 μm
y (galvanometric mirror)	1745 μm	217 μm
z (TAG lens)	200 μm	185 μm

Table. 5.1.2 Comparison between theoretical and experimental scanning range.

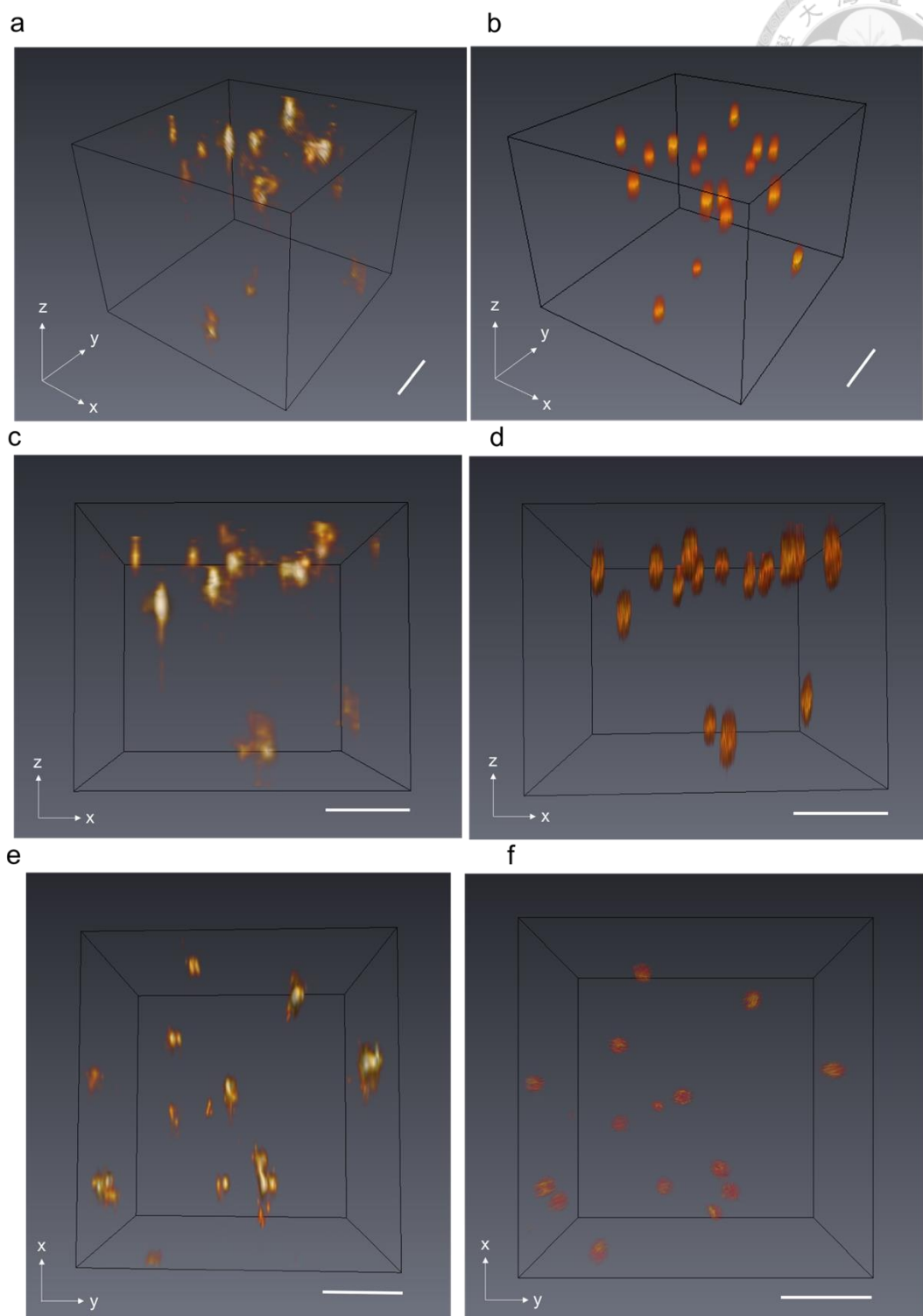
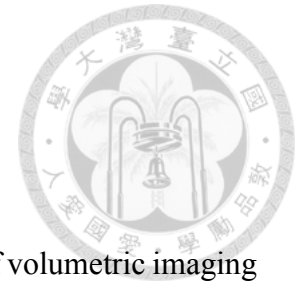


Fig. 5.1.7 Comparison of 3D observation

Via (a) high-speed 32-beam scanning + TAG lens (1.84 ms) and (b) slow single beam scanning + sample translation (> 1 minute). (c) Fast scanning from the x-z plane viewpoint. (d) Slow scanning from the x-z plane viewpoint. (e) Fast scanning from the x-y plane viewpoint. (f) Slow scanning from the x-y plane viewpoint. The high-speed version does not lose information of 10- μm fluorescent microspheres that mimic neuronal soma distribution. The scale bar is 50 μm .



5.1.3 Volumetric imaging: Speed

Although we already mentioned that the above demonstration of volumetric imaging only took 1.84 ms to achieve, which means 543-Hz volume rate. The sample of the demonstration was indeed stationary. To further exhibit imaging high-speed dynamics with our system, we presented time-lapse volumetric images with 1.84 ms/volume imaging speed, i.e. more than 500 volumes per second, showing the flow motion of 10 μm fluorescent microspheres in liquid. Moreover, it also offers the capability of speed measurement. To our knowledge, this is the highest two-photon volumetric imaging rate to date. The complete video of the flowing microspheres was provided in the below link.

<https://drive.google.com/file/d/11Mmhcv7kELSSdYwdG30cPJbKHV9r-3Y1/view?usp=sharing>

Briefly comparing the theoretical volume rate and experimental volume rate as shown in Table. 5.1.3, the experimental value is slightly smaller than theoretical value. The discrepancy might come from unfixed operation frequency of the TAG lens which varied between 69-71 kHz, thus resulting in the slight variation of the imaging speed.

	Theoretical volume rate	Experimental volume rate
Voxel number: 32×128×71	558 Hz	543 Hz

Table. 5.1.3 Comparison between theoretical and experimental volume rate.

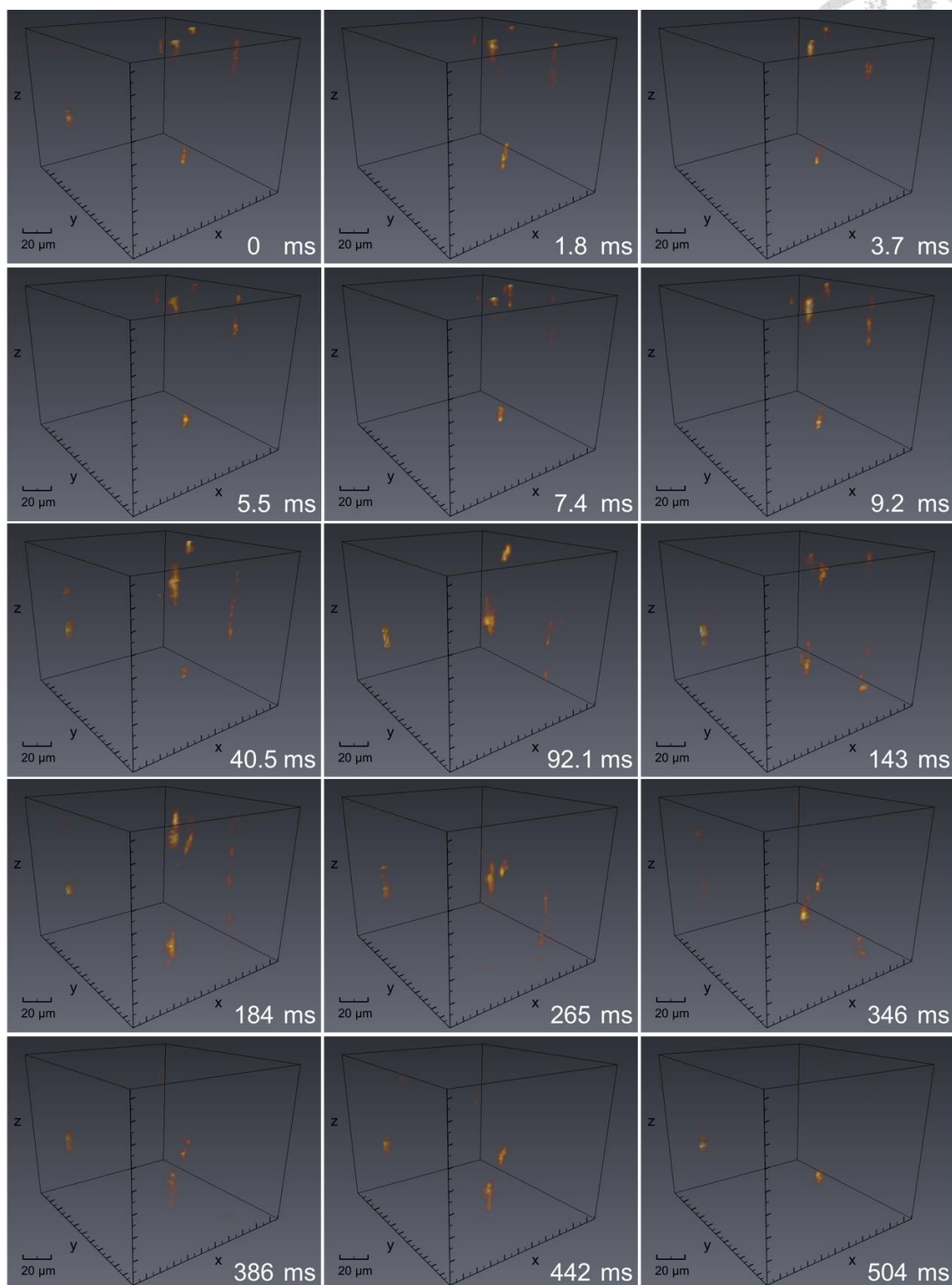


Fig. 5.1.8 Time-lapse volumetric imaging

The video showed the flowing motion of 10 μm fluorescent microspheres, over a volume of $\sim 200 \times 220 \times 185 \mu\text{m}$. Specific timepoints from 0 ms to 9.2 ms were chosen to confirm ms-scale volumetric imaging with 1.84 ms recording duration. Remaining timepoints were then chosen to display the dynamic activity.

5.2 *Drosophila* brain imaging

In our preliminary test, we also apply our system on *Drosophila* brain slide labeled with GCaMP7f on mushroom body. However, the brightness of *Drosophila* brain is too dark to observe. In order to increase the brightness, we use accumulation to enhance the fluorescent signal. By accumulating 20-set volumetric images of *Drosophila* brain, we indeed observe the structure of mushroom body within *Drosophila* brain, as shown in Fig. 5.2.1.

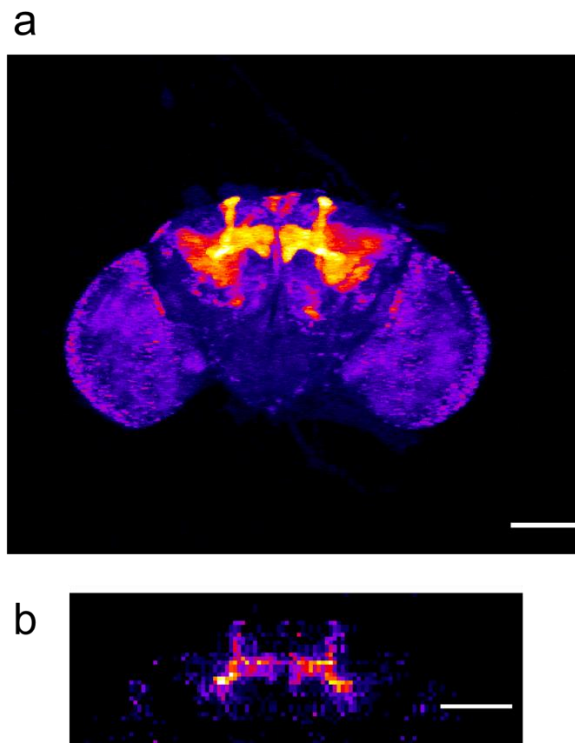


Fig. 5.2.1 *Drosophila* brain imaging labeled with GCaMP7f on mushroom body
(a) *Drosophila* brain image captured by single-beam scanning system. Image size is $874.9 \mu\text{m} \times 874.9 \mu\text{m}$ corresponding to 512×512 pixels. (b) *Drosophila* brain image captured by 32-beam high-speed scanning system. Image size is $217 \mu\text{m} \times 700 \mu\text{m}$ corresponding to 32×128 pixels. The scale bar is $100 \mu\text{m}$.

Fig. 5.2.1(a) is captured by single-beam scanning system, and Fig. 5.2.1(b) is captured by 32-beam high-speed scanning system which accumulated 20 sets of images.

Chapter 6. Discussion



Although we can achieve ms-scale volumetric imaging on fluorescent microspheres, a step to the *Drosophila* brain sample is still far to reach. When we applied our technique on *Drosophila* brain labeled with GCaMP7f on mushroom body (MB) region for testing, somehow the image we got was too dark to distinguish a single neuron. Thus, accumulation is required to enhance the fluorescent signal, however, coming with the disadvantage of decreasing imaging speed. In order to seek the reasons behind this problem, several aspects related to this issue and some drawbacks of our system will be discussed in this section, including absorption of TAG lens, limited photon number, sampling issue, cross-talk problem and shot noise analysis.

6.1 Strong absorption of TAG lens

In section 3.2, we mentioned that there is a strong absorption peak of the TAG lens at around 910 nm which causes large power absorption and thus severe aberration occurs due to nonuniform heating of the material inside the TAG lens. Therefore, we shift the excitation wavelength of the incident laser to 940 nm to avoid the absorption. To demonstrate this phenomenon, we used 920 nm and 940 nm laser to excite FITC solution with about 80 mW input power of the TAG lens and captured the image of 32 foci by the sCMOS camera at the intermediate plane between scan lens and tube lens, as shown in Fig. 6.1.1(a) and (b) respectively. In the case of 920 nm, due to the aberration of the TAG lens, the image becomes quite blurred that we can barely distinguish 32 foci clearly.

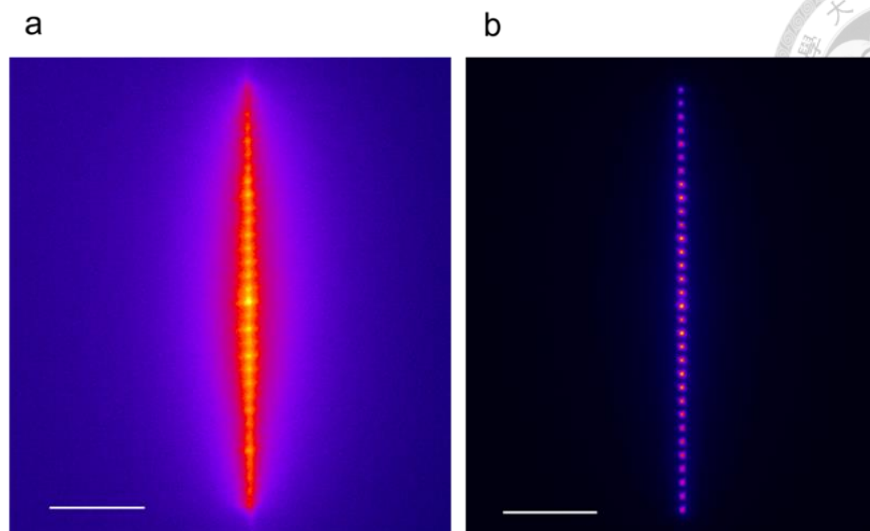


Fig. 6.1.1 Image of 32 foci captured by the sCMOS camera using FITC solution with (a) 920 nm excitation laser and (b) 940 nm excitation laser. The scale bar is 50 μm .

Although by shifting the wavelength of excitation laser to 940 nm to avoid the absorption peak can alleviate the thermal-induced aberration, as we keep increasing incident power of the TAG lens to about 500 mW, the aberration gradually appears. As shown in Fig. 6.1.2, by placing a sCMOS camera at the detection plane of 32-channel PMT, we compare portion of 32 foci before (0 sec) and after (240 sec) the TAG lens induces severe thermal effect in Fig. 6.1.2(a) and Fig. 6.1.2(b) respectively. This indicates that by changing the excitation wavelength from 920 nm to 940 nm can only “treat the symptoms, not the disease.” In order to solve the problem, one way is to use the wavelength whose transmission rate of the TAG lens is high enough to avoid the thermal-induced aberration; however, changing the wavelength also means that fluorescence indicator needs to be changed to collocate with the excitation peak and probably several optical elements need to be modified to meet maximal transmission rate, which might not be a trivial issue. Another possible choice is to change a TAG lens with low-power-absorption material to avoid the thermal effect. Nevertheless, it depends on whether TAG

company provides such kind of commercial TAG lens.

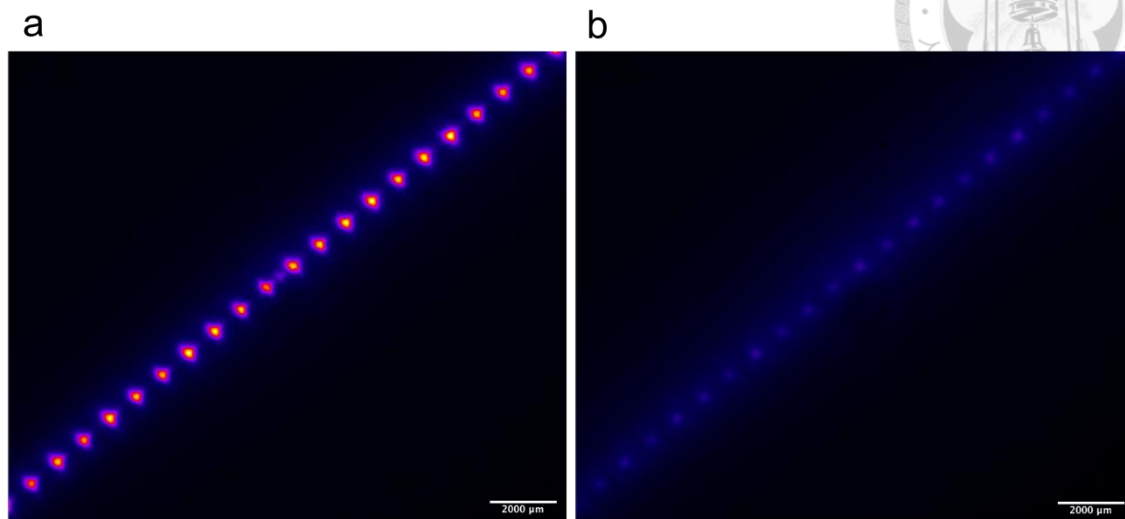


Fig. 6.1.2 Image of partial 32 foci with and without aberration

(a) Before (0 sec) and (b) after (240 sec) the TAG lens induces severe thermal effect, captured by a sCMOS camera using FITC solution and 940 nm excitation laser. The scale bar is 3 mm.

6.2 Emitted photon number

One of the main factors that determines the capability of observing *Drosophila* brain is the number of photons captured by our detector. From the discussion in subsection 3.3.3, the estimated emitted photons collected by our PMT is ~ 2.9 photons per laser pulse which is scarce, not to say that the estimation is based on the assumption of using maximal laser power for excitation. In fact, to avoid the thermal-induced aberration from the TAG lens, only 120 mW laser power after objective lens was used during the experiment (maximal laser power after the objective lens is ~ 300 mW). To achieve high-speed imaging in a living brain, high concentration of fluorescent proteins may be necessary. Instead of using fluorescent proteins, staining neurons with fluorescent dye is one of possible choices since the concentration of dye can be prepared as high as possible,

however, coming with the compromises of nonuniform staining and difficulty for staining in deep tissue. Other strategies to improve the photon yield include reducing the pulse width or decreasing the number of multi-foci, such as changing the number of beams from 32 to 16, under the same laser power condition which may increase the possibility to generate more emitted fluorescent photons for each beam. These will be our future research direction.

6.3 Equal-interval sampling against stochastic fluorescent pulses

Another reason why we cannot observe image of *Drosophila* brain might be that we didn't sample the right peak of each fluorescent pulse signal. As mentioned in subsection 3.3.5, we try to align the sampling point to the peak of fluorescent "wave packet" to acquire maximal amplitude of signals. However, the "wave packet" is actually constructed by the overlapping of several fluorescent pulses appearing randomly within the lifetime of fluorescence, ~2-3 ns in general, and visualized by an oscilloscope. It is highly possible that we didn't sample right at the peak of each pulse. Sometimes, we even miss the pulse, and the main reason is because of the short pulse response of the PMT and amplifier. To address this problem, we can replace the amplifier with a short frequency bandwidth amplifier or cascade with an RLC circuit to intentionally extend the pulse width, so that we won't encounter the situation of sampling nothing. Nevertheless, extending the pulse width comes with another trade-off that the amplitude of pulse response decreases at the same time. It seems that if we choose a higher-gain amplifier with short frequency bandwidth can offset the detrimental side effect. Through carefully searching of commercial surface mount amplifier, ADRF6520 (Analog Devices) with

gain as high as 53 dB (30 dB higher than recent amplifier) and the tunable frequency bandwidth down to 36 MHz might fit our need. To prove that it can really extend the pulse width, we purchased an ADRF6520 test board connected with single-channel PMT (H7422-40, Hamamatsu) for testing. As shown in Fig. 6.3.1, the amplifier operated at by-pass mode in Fig. 6.3.1 (a) and 36 MHz frequency bandwidth mode in Fig. 6.3.1 (b) respectively. We can see that, before changing frequency bandwidth, the pulse width is ~ 4 ns, and after adjusting the frequency bandwidth to 36 MHz, the pulse width obviously extends to ~ 10 ns, approaching duration of adjacent pulse (12.5 ns). By further increasing the gain, the peak response can rise to 1 V which works quite well and nicely fits our purpose. Thus, in the next step, we are going to customized an amplifier mounted with 32-channel ADRF6520 to enhance our system.

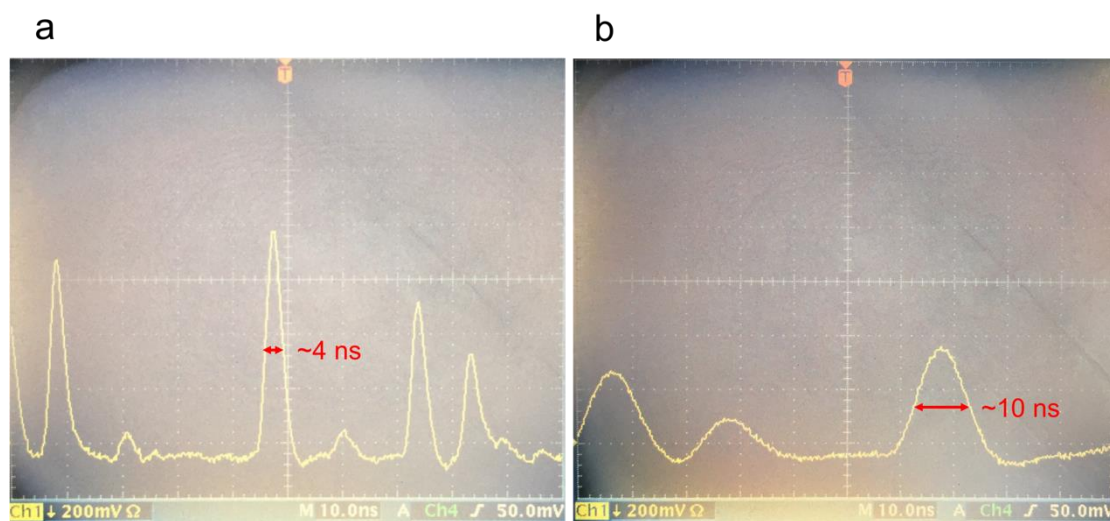
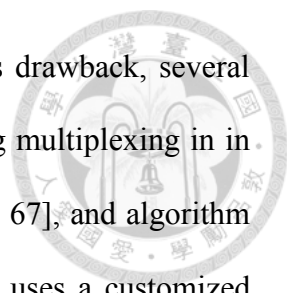


Fig. 6.3.1 Comparison of ADRF6520 amplifier with different frequency responses using single-channel PMT detection

(a) By-pass mode (b) 36 MHz frequency bandwidth mode

6.4 Cross-talk

A well-known major challenge of multi-focal multi-photon system is cross-talk,



especially for the turbid neural structure. In order to deal with this drawback, several methods have been proposed to solve the cross-talk issue, including multiplexing in in time-domain [43], frequency-domain [65, 66], in space-domain [38, 67], and algorithm for spatial pixel reassignment [68]. Temporal-domain multiplexing uses a customized mirror pair to generate multiple beams with different time delays and collects the signal of each beam by a single channel PMT; however, the data acquisition rate will be restricted by lifetime of fluorophores, 2-3 ns in general. In reference [43], the maximum data throughput is less than 300 MHz, one order lower than our system (~10 GHz maximum, now 2.56 GHz). Frequency-domain multiplexing requires encoding each beam with different frequency components, which need to be significantly smaller than laser repetition rate, thus resulting in long voxel dwell time and low imaging speed (0.4 frame/s in reference). Space-domain multiplexing, such as spinning-disk microscopy, which adopts pinhole to eliminate scattering signal to mitigate cross-talk effect; however, it will reject portion of interested signal at the same time. Therefore, in order not to sacrifice data throughput nor the fluorescent signal, we plan to apply post-calibration algorithm to re-assign cross-talk signal back to correct channel.

6.5 Shot noise

One of the limitations of high-speed imaging is that the fluorescent signal might be dominated by noise, since the photon number is not high enough, leading to the difficulty of distinguish interested signal from noise. In order to quantify noise level, including shot noise, in our system, I use single beam to scan the *Drosophila* brain slide which is captured by one channel of 32-channel PMT. By adjusting the input power, we can plot the curve of fluorescent signal versus input power both in linear and log scale, as shown in Fig. 6.5.1. The shot noise is determined by standard deviation which is marked by the

error bar within the curve. After measuring the signal-to-noise ratio (SNR) of each power, the SNR with input laser power larger than 40 mW can reach higher than 3.4. The slope of the curve in log scale from 40 mW to 100 mW is 1.84 which fits quite well with two-photon excitation (theoretical slope is 2). However, below 20 mW, the shot noise dominates the fluorescent signal which is hard to differentiate usable signal. The slope of the curve in log scale from 5 mW to 20 mW is 0.44 which also fits the distribution of shot noise. Nevertheless, in our system, the maximum input power is similar to the case of 40 mW which is capable of distinguishing *Drosophila* brain structure.

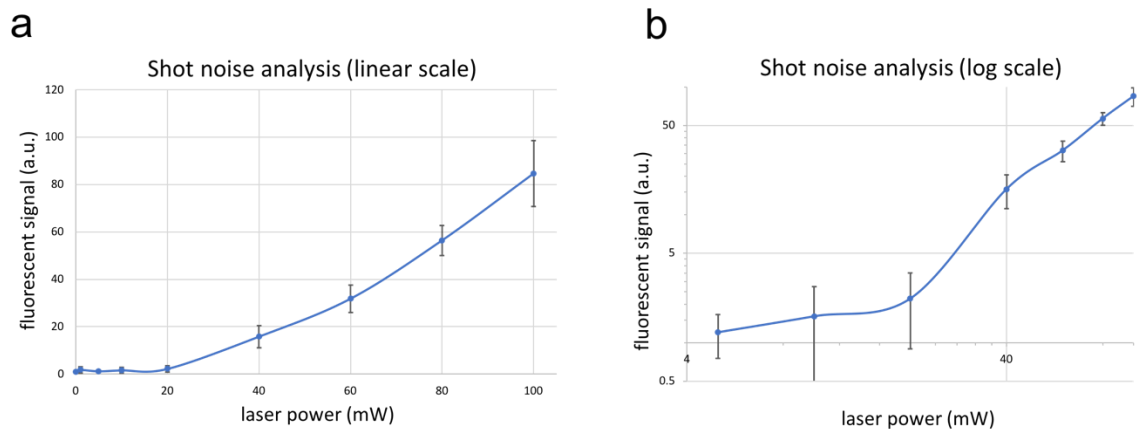
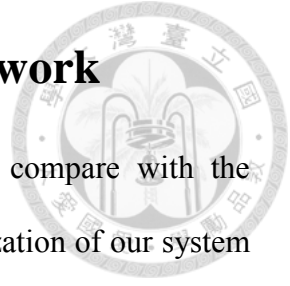


Fig. 6.5.1 Shot noise analysis

Fluorescent signal of *Drosophila* brain image versus input power in (a) linear scale and (b) log scale.

Chapter 7. Conclusion and future work



In conclusion, we briefly summarize the achievements and compare with the requirements of our aim. Finally, few outlooks related to the optimization of our system toward the functional study in *Drosophila* brain are proposed, and some possible applications are brought forward for future prospect.

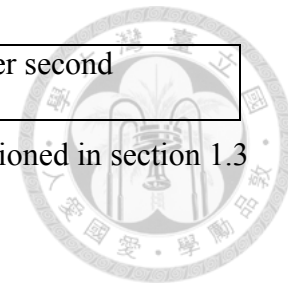
7.1 Conclusion

Our multi-focal two-photon volumetric imaging system indeed achieves record-high ~ 500 volumes per second with \sim micrometer spatial resolution in a $\sim 200 \mu\text{m}$ cubic volume, based on the combination of not only the high-speed multi-focal laser scanning and the TAG lens, but also the deep imaging capability of two-photon excitation plus multiple point detectors. The comparison between requirements of our aim and experimental achievements is showed in Table. 7.1.1. Total data throughput is 2.56 GHz, which can be further enhanced to more than 10 GHz, much higher than single-channel detector system and comparable to commercial camera-based techniques. As a proof of concept, we have demonstrated high speed imaging with flowing fluorescence beads, capturing volumetric dynamics of flow motion. To our knowledge, this is the fastest multi-photon volumetric imaging speed to date.

Requirements	Achievements
Noninvasive	Inherent property of optical microscopy
$\sim \mu\text{m}$ spatial resolution	Lateral resolution: $693 \pm 6 \text{ nm}$ Axial resolution: $5.46 \pm 0.18 \mu\text{m}$
Hundreds of micrometers	Inherent property of optical microscopy
Volumetric imaging	$207 \times 217 \times 185 \mu\text{m}^3$

~ms temporal resolution	543 volumes per second
-------------------------	------------------------

Table. 7.1.1 Comparison between the requirements of our aim mentioned in section 1.3 and the experimental achievements.



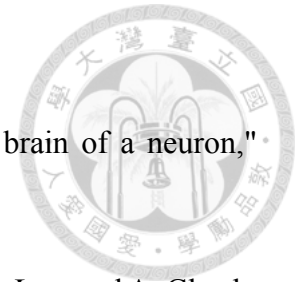
7.2 Future work

Although we have demonstrated the volumetric imaging with ~500 Hz imaging speed, possessing the opportunity to capture propagation of action potential, we now still face some difficulties toward the observation of the *Drosophila* brain. The main challenge is that the fluorescence signal of *Drosophila* brain is too weak for detection. Although, by using accumulation, we can enhance the fluorescent signal, it will ultimately decrease the imaging speed. To tackle with this situation, as we mention in section 6.2, a fluorescent indicator with higher concentration is critical. Decreasing the number of beams, such as from 32 to 16, is another possibility to enhance the intensity of each beam, however, with the compromise of smaller ROI. On the other hand, due to the fact that the occurrence of fluorescence pulse appears randomly, if we can ensure to at least sample each fluorescence pulse, we have more confidence to observe the *Drosophila* brain, as we mentioned in section 6.3. Once those problems are successfully solved, this innovative high-speed volumetric imaging system may open the avenue for the study of ms-scale neural dynamics within whole brains.

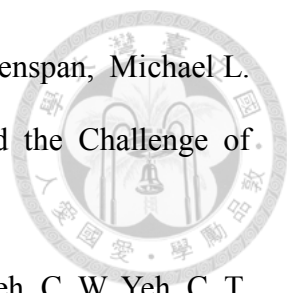
During the optimization of the abovementioned aspects, there are still some possible applications that worth a try, such as acceleration of structural imaging. For example, the advantage of our system is that we can increase the scanning speed up to 32-fold compared to single-beam scanning system, since we use 32 beams for scanning simultaneously. The combination of TAG lens makes our system resemble parallel

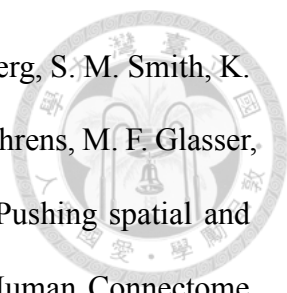
“vertical” light sheets. If a sample requires one month to reconstruct a high-digital resolution image by single-beam scanning system, the required time can be further reduced within one day by using our 32-beam system. Other applications, such as flow cytometry, drug flowing analysis and organoid screening, might also be possible ways for us to push forward in the future.

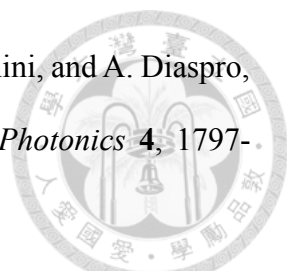
References



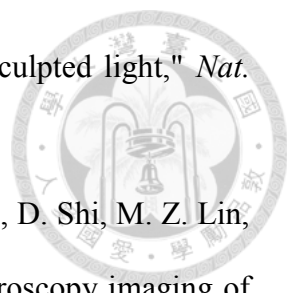
1. K. Sidiropoulou, E. K. Pissadaki, and P. Poirazi, "Inside the brain of a neuron," *EMBO Rep.* **7**, 886-892 (2006).
2. L. Squire, F. E. Bloom, N. C. Spitzer, L. R. Squire, D. Berg, S. du Lac, and A. Ghosh, *Fundamental Neuroscience* (Elsevier Science, 2008).
3. D. Schubert, R. Kötter, H. J. Luhmann, and J. F. Staiger, "Morphology, Electrophysiology and Functional Input Connectivity of Pyramidal Neurons Characterizes a Genuine Layer Va in the Primary Somatosensory Cortex," *Cereb. Cortex* **16**, 223-236 (2005).
4. H. Wang, Q. Zhu, L. Ding, Y. Shen, C.-Y. Yang, F. Xu, C. Shu, Y. Guo, Z. Xiong, Q. Shan, F. Jia, P. Su, Q.-R. Yang, B. Li, Y. Cheng, X. He, X. Chen, F. Wu, J.-N. Zhou, F. Xu, H. Han, P.-M. Lau, and G.-Q. Bi, "Scalable volumetric imaging for ultrahigh-speed brain mapping at synaptic resolution," *Natl. Sci. Rev.* **6**, 982-992 (2019).
5. M. G. Preti, T. A. W. Bolton, and D. Van De Ville, "The dynamic functional connectome: State-of-the-art and perspectives," *NeuroImage* **160**, 41-54 (2017).
6. M. Dipalo, H. Amin, L. Lovato, F. Moia, V. Caprettini, G. C. Messina, F. Tantussi, L. Berdondini, and F. De Angelis, "Intracellular and Extracellular Recording of Spontaneous Action Potentials in Mammalian Neurons and Cardiac Cells with 3D Plasmonic Nanoelectrodes," *Nano Lett.* **17**, 3932-3939 (2017).
7. F. A. Azevedo, L. R. Carvalho, L. T. Grinberg, J. M. Farfel, R. E. Ferretti, R. E. Leite, W. Jacob Filho, R. Lent, and S. Herculano-Houzel, "Equal numbers of neuronal and nonneuronal cells make the human brain an isometrically scaled-up primate brain," *J. Comp. Neurol.* **513**, 532-541 (2009).
8. S. Herculano-Houzel, B. Mota, and R. Lent, "Cellular scaling rules for rodent brains," *Proc. Natl. Acad. Sci. U.S.A.* **103**, 12138-12143 (2006).

- 
9. A. P. Alivisatos, M. Chun, George M. Church, Ralph J. Greenspan, Michael L. Roukes, and R. Yuste, "The Brain Activity Map Project and the Challenge of Functional Connectomics," *Neuron* **74**, 970-974 (2012).
10. A. S. Chiang, C. Y. Lin, C. C. Chuang, H. M. Chang, C. H. Hsieh, C. W. Yeh, C. T. Shih, J. J. Wu, G. T. Wang, Y. C. Chen, C. C. Wu, G. Y. Chen, Y. T. Ching, P. C. Lee, C. Y. Lin, H. H. Lin, C. C. Wu, H. W. Hsu, Y. A. Huang, J. Y. Chen, H. J. Chiang, C. F. Lu, R. F. Ni, C. Y. Yeh, and J. K. Hwang, "Three-dimensional reconstruction of brain-wide wiring networks in *Drosophila* at single-cell resolution," *Curr. Biol.* **21**, 1-11 (2011).
11. U. B. Pandey and C. D. Nichols, "Human disease models in *Drosophila melanogaster* and the role of the fly in therapeutic drug discovery," *Pharmacol. Rev.* **63**, 411-436 (2011).
12. J. C. Tuthill, "Lessons from a compartmental model of a *Drosophila* neuron," *J. Neurosci.* **29**, 12033-12034 (2009).
13. N. W. Gouwens and R. I. Wilson, "Signal Propagation in *Drosophila* Central Neurons," *J. Neurosci.* **29**, 6239-6249 (2009).
14. H. T. Beier and B. L. Ibey, "Experimental comparison of the high-speed imaging performance of an EM-CCD and sCMOS camera in a dynamic live-cell imaging test case," *PLoS One* **9**, e84614 (2014).
15. M. Uecker, S. Zhang, D. Voit, A. Karaus, K. D. Merboldt, and J. Frahm, "Real-time MRI at a resolution of 20 ms," *NMR Biomed* **23**, 986-994 (2010).
16. G. H. Glover, "Overview of functional magnetic resonance imaging," *Neurosurg. Clin. N. Am.* **22**, 133-139 (2011).
17. K. Ugurbil, J. Xu, E. J. Auerbach, S. Moeller, A. T. Vu, J. M. Duarte-Carvajalino, C. Lenglet, X. Wu, S. Schmitter, P. F. Van de Moortele, J. Strupp, G. Sapiro, F. De

- 
- Martino, D. Wang, N. Harel, M. Garwood, L. Chen, D. A. Feinberg, S. M. Smith, K. L. Miller, S. N. Sotiropoulos, S. Jbabdi, J. L. Andersson, T. E. Behrens, M. F. Glasser, D. C. Van Essen, E. Yacoub, and W. U.-M. H. Consortium, "Pushing spatial and temporal resolution for functional and diffusion MRI in the Human Connectome Project," *Neuroimage* **80**, 80-104 (2013).
18. S. F. Cogan, "Neural Stimulation and Recording Electrodes," *Annu Rev Biomed Eng* **10**, 275-309 (2008).
19. H. Bin, Y. Lin, C. Wilke, and Y. Han, "Electrophysiological Imaging of Brain Activity and Connectivity—Challenges and Opportunities," *IEEE. Trans. Biomed. Eng.* **58**, 1918-1931 (2011).
20. Z. Fekete, "Recent advances in silicon-based neural microelectrodes and microsystems: a review," *Sens. Actuators B Chem.* **215**, 300-315 (2015).
21. B. A. Wilt, L. D. Burns, E. T. Wei Ho, K. K. Ghosh, E. A. Mukamel, and M. J. Schnitzer, "Advances in light microscopy for neuroscience," *Annu. Rev. Neurosci.* **32**, 435-506 (2009).
22. D. R. Hochbaum, Y. Zhao, S. L. Farhi, N. Klapoetke, C. A. Werley, V. Kapoor, P. Zou, J. M. Kralj, D. Maclaurin, N. Smedemark-Margulies, J. L. Saulnier, G. L. Boulting, C. Straub, Y. K. Cho, M. Melkonian, G. K. Wong, D. J. Harrison, V. N. Murthy, B. L. Sabatini, E. S. Boyden, R. E. Campbell, and A. E. Cohen, "All-optical electrophysiology in mammalian neurons using engineered microbial rhodopsins," *Nat. Methods* **11**, 825-833 (2014).
23. V. Voleti, K. B. Patel, W. Li, C. Perez Campos, S. Bharadwaj, H. Yu, C. Ford, M. J. Casper, R. W. Yan, W. Liang, C. Wen, K. D. Kimura, K. L. Targoff, and E. M. C. Hillman, "Real-time volumetric microscopy of in vivo dynamics and large-scale samples with SCAPE 2.0," *Nat. Methods* **16**, 1054-1062 (2019).

- 
24. M. Duocastella, G. Sancataldo, P. Saggau, P. Ramoino, P. Bianchini, and A. Diaspro, "Fast Inertia-Free Volumetric Light-Sheet Microscope," *ACS Photonics* **4**, 1797-1804 (2017).
25. W. R. Zipfel, R. M. Williams, and W. W. Webb, "Nonlinear magic: multiphoton microscopy in the biosciences," *Nat. Biotechnol.* **21**, 1369-1377 (2003).
26. B. V. R. Tata and B. Raj, "Confocal laser scanning microscopy: Applications in material science and technology," *Bull. Mater. Sci.* **21**, 263-278 (1998).
27. F. Helmchen and W. Denk, "Deep tissue two-photon microscopy," *Nat. Methods* **2**, 932-940 (2005).
28. H. Li, Q. Cui, Z. Zhang, L. Fu, and Q. Luo, "Nonlinear optical microscopy for immunoimaging: a custom optimized system of high-speed, large-area, multicolor imaging," *Quant. Imaging. Med. Surg.* **5**, 30-39 (2014).
29. A. M. D. Lee, H. Wang, Y. Yu, S. Tang, J. Zhao, H. Lui, D. I. McLean, and H. Zeng, "In vivo video rate multiphoton microscopy imaging of human skin," *Opt. Lett.* **36**, 2865-2867 (2011).
30. K. F. Tehrani, C. V. Latchoumane, W. M. Southern, E. G. Pendleton, A. Maslesa, L. Karumbaiah, J. A. Call, and L. J. Mortensen, "Five-dimensional two-photon volumetric microscopy of in-vivo dynamic activities using liquid lens remote focusing," *Biomed. Opt. Express* **10**, 3591 (2019).
31. W. Göbel, B. M. Kampa, and F. Helmchen, "Imaging cellular network dynamics in three dimensions using fast 3D laser scanning," *Nat. Methods* **4**, 73-79 (2006).
32. C. Huang, C. Y. Tai, K. P. Yang, W. K. Chang, K. J. Hsu, C. C. Hsiao, S. C. Wu, Y. Y. Lin, A. S. Chiang, and S. W. Chu, "All-Optical Volumetric Physiology for Connectomics in Dense Neuronal Structures," *iScience* **22**, 133-146 (2019).
33. R. Lu, M. Tanimoto, M. Koyama, and N. Ji, "50 Hz volumetric functional imaging

- with continuously adjustable depth of focus," *Biomed. Opt. Express* **9**, 1964-1976 (2018).
34. K. M. N. S. Nadella, H. Roš, C. Baragli, V. A. Griffiths, G. Konstantinou, T. Koimtzis, G. J. Evans, P. A. Kirkby, and R. A. Silver, "Random-access scanning microscopy for 3D imaging in awake behaving animals," *Nat. Methods* **13**, 1001-1004 (2016).
35. E. J. Botcherby, C. W. Smith, M. M. Kohl, D. Debarre, M. J. Booth, R. Juskaitytis, O. Paulsen, and T. Wilson, "Aberration-free three-dimensional multiphoton imaging of neuronal activity at kHz rates," *Proc. Natl. Acad. Sci. U.S.A.* **109**, 2919-2924 (2012).
36. J. Bewersdorf, R. Pick, and S. W. Hell, "Multifocal multiphoton microscopy," *Opt. Lett.* **23**, 655-657 (1998).
37. R. Yuste, "Two-photon imaging with diffractive optical elements," *Front. Neural Circuits* **3**(2009).
38. K. Otomo, T. Hibi, T. Murata, H. Watanabe, R. Kawakami, H. Nakayama, M. Hasebe, and T. Nemoto, "Multi-point Scanning Two-photon Excitation Microscopy by Utilizing a High-peak-power 1042-nm Laser," *Anal Sci* **31**, 307-313 (2015).
39. K. Bahlmann, P. T. C. So, M. Kirber, R. Reich, B. Kosicki, W. McGonagle, and K. Bellve, "Multifocal multiphoton microscopy (MMM) at a frame rate beyond 600 Hz," *Opt. Express* **15**, 10991-10998 (2007).
40. T. V. Truong, W. Supatto, D. S. Koos, J. M. Choi, and S. E. Fraser, "Deep and fast live imaging with two-photon scanned light-sheet microscopy," *Nat. Methods* **8**, 757-760 (2011).
41. S. Quirin, J. Jackson, D. S. Peterka, and R. Yuste, "Simultaneous imaging of neural activity in three dimensions," *Front. Neural Circuits* **8**(2014).
42. T. Schrodell, R. Prevedel, K. Aumayr, M. Zimmer, and A. Vaziri, "Brain-wide 3D

- 
- imaging of neuronal activity in *Caenorhabditis elegans* with sculpted light," *Nat. Methods* **10**, 1013-1020 (2013).
43. J. Wu, Y. Liang, S. Chen, C.-L. Hsu, M. Chavarha, S. W. Evans, D. Shi, M. Z. Lin, K. K. Tsia, and N. Ji, "Kilohertz two-photon fluorescence microscopy imaging of neural activity in vivo," *Nat. Methods* **17**, 287-290 (2020).
44. K. H. Kim, C. Buehler, K. Bahlmann, T. Ragan, W.-C. A. Lee, E. Nedivi, E. L. Heffer, S. Fantini, and P. T. C. So, "Multifocal multiphoton microscopy based on multianode photomultiplier tubes," *Opt. Express* **15**, 11658-11678 (2007).
45. B. F. Grewe, F. F. Voigt, M. van 't Hoff, and F. Helmchen, "Fast two-layer two-photon imaging of neuronal cell populations using an electrically tunable lens," *Biomed. Opt. Express* **2**, 2035-2046 (2011).
46. L. Sacconi, E. Froner, R. Antolini, M. R. Taghizadeh, A. Choudhury, and F. S. Pavone, "Multiphoton multifocal microscopy exploiting a diffractive optical element," *Opt. Lett.* **28**, 1918-1920 (2003).
47. T. Nielsen, M. Fricke, D. Hellweg, and P. Andresen, "High efficiency beam splitter for multifocal multiphoton microscopy," *J. Microsc.* **201**, 368-376 (2001).
48. B. O. Watson, V. Nikolenko, R. Araya, D. S. Peterka, A. Woodruff, and R. Yuste, "Two-photon microscopy with diffractive optical elements and spatial light modulators," *Front. Neurosci.* **4**(2010).
49. Refer to the description of DOE from the HOLOEYE company:
<https://holoeye.com/diffractive-optics/>
50. N. Olivier, A. Mermillod-Blondin, C. B. Arnold, and E. Beaufepaire, "Two-photon microscopy with simultaneous standard and extended depth of field using a tunable acoustic gradient-index lens," *Opt. Lett.* **34**, 1684-1686 (2009).
51. K.-J. Hsu, K.-Y. Li, Y.-Y. Lin, A.-S. Chiang, and S.-W. Chu, "Optimizing depth-of-

- field extension in optical sectioning microscopy techniques using a fast focus-tunable lens," *Opt. Express* **25**, 16783-16794 (2017).
52. M. Duocastella, B. Sun, and C. Arnold, "Simultaneous imaging of multiple focal planes for three-dimensional microscopy using ultra-high-speed adaptive optics," *J Biomed Opt* **17**, 050505 (2012).
53. Y. Xu, P. Zou, and A. E. Cohen, "Voltage imaging with genetically encoded indicators," *Curr Opin Chem Biol* **39**, 1-10 (2017).
54. T. Knopfel and C. Song, "Optical voltage imaging in neurons: moving from technology development to practical tool," *Nat. Rev. Neurosci.* **20**, 719-727 (2019).
55. See the specification of the TAG lens online: <https://www.tag-optics.com/index.php>
56. Kuo-Jen Hsu, "High-speed and Deep-tissue Optical Microscope Techniques for Drosophila Brain Functional Studies," Doctoral Dissertation, National Taiwan University, 2018.
57. See the specification of the TAG lens online: <https://www.tag-optics.com/index.php>
58. Ron D. Frostig. In Vivo Optical Imaging of Brain Function (CRC Press/ Taylor & Francis, 2009).
59. M. Drobizhev, N. S. Makarov, S. E. Tillo, T. E. Hughes, and A. Rebane, "Two-photon absorption properties of fluorescent proteins," *Nat. Methods* **8**, 393-399 (2011).
60. T. Hazelrigg, N. Liu, Y. Hong, and S. Wang, "GFP Expression in Drosophila Tissues: Time Requirements for Formation of a Fluorescent Product," *Dev. Biol.* **199**, 245-249 (1998).
61. L.-C. Cheng, N. G. Horton, K. Wang, S.-J. Chen, and C. Xu, "Measurements of multiphoton action cross sections for multiphoton microscopy," *Biomed. Opt. Express* **5**, 3427 (2014).
62. See from the specification of Hamamatsu multi-anode PMT catalog.

63. See the specification of the TAG lens online: <https://www.tag-optics.com/index.php>
64. K. J. Hsu, Y. Y. Lin, Y. Y. Lin, K. Su, K. L. Feng, S. C. Wu, Y. C. Lin, A. S. Chiang, and S. W. Chu, "Millisecond two-photon optical ribbon imaging for small-animal functional connectome study," *Opt. Lett.* **44**, 3190-3193 (2019).
65. C.-S. Liao, P. Wang, P. Wang, J. Li, H. J. Lee, G. Eakins, and J.-X. Cheng, "Spectrometer-free vibrational imaging by retrieving stimulated Raman signal from highly scattered photons," *Sci. Adv.* **1**, e1500738 (2015).
66. S. S. Howard, A. Straub, N. G. Horton, D. Kobat, and C. Xu, "Frequency-multiplexed in vivo multiphoton phosphorescence lifetime microscopy," *Nat. Photonics* **7**, 33-37 (2012).
67. T. Shimozawa, K. Yamagata, T. Kondo, S. Hayashi, A. Shitamukai, D. Konno, F. Matsuzaki, J. Takayama, S. Onami, H. Nakayama, Y. Kosugi, T. M. Watanabe, K. Fujita, and Y. Mimori-Kiyosue, "Improving spinning disk confocal microscopy by preventing pinhole cross-talk for intravital imaging," *Proc. Natl. Acad. Sci. U.S.A.* **110**, 3399-3404 (2013).
68. J. W. Cha, V. R. Singh, K. H. Kim, J. Subramanian, Q. Peng, H. Yu, E. Nedivi, and P. T. C. So, "Reassignment of Scattered Emission Photons in Multifocal Multiphoton Microscopy," *Sci. Rep.* **4**(2014).